Surface and Molecular Level Characterization of Nanomaterials for Water Treatment and
Drug Delivery

by
Sheyda Shakiba

A dissertation submitted to the Department of Civil and Environmental Engineering,
Cullen College of Engineering
in partial fulfillment of the requirements for the degree of

DOCTOR OF PHILOSOPHY

in Environmental Engineering

Chair of Committee: Stacey M. Louie

Committee Member: William G. Rixey

Committee Member: Debora F. Rodrigues

Committee Member: Jacinta C. Conrad

Committee Member: Xinli Liu

Committee Member: Elham Fini

University of Houston
May 2021

ACKNOWLEDGMENTS

I had an excellent opportunity to pursue a Ph.D. degree at the University of Houston. This journey at the University of Houston would have been impossible without the constant support from my advisor, colleges, family, and friends. I express my gratitude to my advisor, Dr. Stacey M. Louie, for accepting me as a graduate research assistant and devoting a tremendous amount of time to training me on lab instruments, experimental designs, data interpretation, and data analysis. I will also appreciate her for helping me to improve my critical research thinking and presentation skills. I would also like to thank my committee members, Dr. William G. Rixey, Dr. Debora F. Rodrigues, Dr. Jacinta C. Conrad, Dr. Xinli Liu, and Dr. Elham Fini, for providing their feedback and comments on my work.

I would also like to thank Dr. Charisma Lattao for her constant moral support during the last four years, and for training me on lab instruments, and for providing laboratory assistance. I would also like to thank other colleagues and professors for providing resources and laboratory assistance, including Prof. Michael Harold for access to the FTIR instrument, Dr. Vincent A. Hackley for the NIST SRM 1898 TiO_2 NPs, and Prof. Gregory V. Lowry for the SEC column. I would also appreciate our collaborators, Dr. Carlos E. Astete and Dr. Cristina M. Sabliov from Louisiana State University, for synthesis and providing TEM images of polymeric nanoparticles. I would also thank Dr. Rafael Cueto for conducting DSC measurements and data analysis. I also thank Luis R. Barco for helping in UV-Vis spectral analysis. I am also thankful to

ABSTRACT

Nanomaterials have versatile applications in a variety of fields, including water treatment applications in environmental engineering and delivery of active ingredients for biomedical or agricultural applications. To explain, predict, and improve the functionality of nanoparticles for these applications, it is essential to provide a detailed and robust characterization of their surface and molecular level interactions. However, the characterization of these nanoscale systems is often challenging. This dissertation contributes toward developing new approaches to characterize and predict the surface chemistry and release behavior of nanomaterials. Specifically, the first section of the dissertation focuses on measuring and predicting competitive adsorption of proteins and natural organic matter onto titanium dioxide nanomaterials for water treatment. This research identified that intermolecular interactions and the kinetics of adsorption are critical to predict the adsorbed layer composition in complex environmental matrices. The following sections focus on developing advanced multi-detector asymmetric flow field – flow fractionation (AF4) methods to characterize the release of active ingredients from polymeric nanoparticles. This research demonstrated that, along with providing more robust and rapid analysis of drug release compared to conventional methods, the unique capability of the AF4 analysis to acquire size-resolved release profiles enables an improved understanding of release mechanisms that is not achievable in bulk time-resolved assays. Overall, the new methods and modeling approaches developed here can be broadly applied to evaluate the surface and molecular interactions of nanomaterials and thereby better predict their functionality and design improved nanomaterials for environmental and health applications.

TABLE OF CONTENTS

CHAPTER 3. NOVEL METHODS FOR CHARACTERIZATION OF DRUG RELEASE FROM POLYMERIC NANOPARTICLES

CHAPTER 4. SIZE-DEPENDENT ANALYSIS TO DISTINGUISH MECHANISMS OF RELEASE FROM POLYMERIC NANOPARTICLES

APPENDIX C. SUPPORTING INFORMATION FOR

LIST OF TABLES

LIST OF FIGURES

xvii

CHAPTER 1. INTRODUCTION

1.1 Overview of Nanotechnology Applications and Characterization Needs

Engineered nanoparticles (NPs), including metal oxide and polymeric NPs, have versatile applications in various fields, such as environmental fields for water treatment or pharmaceuticals for drug delivery purposes.[1] To fully characterize and predict the NPs behavior for water treatment applications, it is critical to investigate their properties under conditions that mimic the actual environments. Natural and engineered systems contain various types of macromolecules, such as proteins, polysaccharides, and humic substances. Once NPs are exposed to the environmental matrix, the interaction of macromolecules with different physicochemical properties and their possible adsorption on the NP surface can significantly change the NP properties (e.g., charge, surface chemistry, etc.) and hence affect the fate, transport, and functionality of the NPs.[2-4] Therefore, the investigation of the adsorption process and molecular-level characterization of the NPs is essential to predict the change in the dissolution, reactivity, or aggregation state of the NPs and understand their likely functionality during realistic application scenarios such as water treatment.

In addition to metal and metal oxide nanomaterials, polymeric nanoparticles are of growing interest as biodegradable or biocompatible materials for both biomedical and environmental (e.g., agricultural) applications. In these applications, the nanoparticle is often intended to serve as a carrier for an active ingredient. Hence, in addition to characterization of the NP itself, it is essential to understand the release

profile of active ingredients from the NPs and identify the mechanisms to predict the release behavior under any relevant application conditions (e.g., temperature, pH, etc.).

In this chapter, we provide a short literature review and discuss current research gaps in evaluating and predicting the surface transformations on metal oxide NPs in complex matrices and active ingredient release from polymeric nanocarriers.

1.2 Current Research Gaps

1.2.1 Surface Transformations of Metal Oxide Nanoparticles in Complex Matrices

Metal and metal oxide nanoparticles (NPs) have many applications in water treatment, for example, as adsorbents for removal of contaminants in drinking water or wastewater [5-8] or for removal of natural organic matter (NOM) from drinking water to reduce disinfection by-product formation,[9] or as reactive materials to degrade contaminants. Hereafter, we discuss challenges in predicting the surface transformations of NPs in environmental matrices, with a specific focus on titanium dioxide (TiO_2) NPs as photocatalytic nanomaterials of wide interest for the degradation of emerging contaminants.[10-13]

Evaluating adsorption from more complex mixtures can be hindered by the challenging nature of separation and selective detection. Furthermore, during the adsorption process, the compounds adsorb from a bulk mixture of macromolecules; therefore, the interactions of free molecules in both the solution phase and at the interface (with the adsorbate species) should not be neglected. Additionally, in multi-component systems, compounds with similar or different adsorption affinity might exist. Therefore, in addition to the adsorption process for each individual compound,

2

other simultaneous processes such as co-adsorption, displacement of the adsorbed species by solution-phase species, or multi-layer adsorption need to be considered.

The majority of the prior literature on corona formation has considered simplified systems with only one single class of compound under fixed or varying environmental conditions. For instance, adsorption of different amino acids[14] (each individually) or an organic acid (i.e., citric acid[15]) onto TiO_2 at different pH were investigated. Some studies also considered the effect of different classes of macromolecules adsorption (in single-component solution) to TiO_2 NPs and their subsequent effect on NPs functionalities. During a recent study, Wu et al. investigated the effect of bovine serum albumin (BSA) or fulvic acid (FA) coatings on photoreactivity properties of TiO_2 NPs[16] but had not considered the system containing both BSA and FA. Even adsorption from a single class of components, such as humic substances or natural organic matter (NOM), can be complicated to measure and predict given the broad range of individual components included in the classification.[17, 18] For example, NOM adsorption might vary based on the NOM origin,[19, 20] properties of the NOM (e.g., functional groups, molecular weight),[21, 22] the NPs (e.g., size, charge),[11] or environmental conditions (e.g., pH, ionic strength, types of ions).[11, 21 23] The competitive adsorption between different fractions of the NOM, and higher affinity for species with higher aromaticity and molecular weight has been reported in a number of studies.[11, 24, 25]

In environmental applications, the NPs can be expected to encounter not only NOM but even more complex mixtures of biomolecules and NOM. However, few prior studies have considered systems containing NOM with other types of compounds like

proteins or other biomolecules. Prediction of competitive adsorption could be relatively simple if equilibrium can be assumed. However, recent studies have demonstrated the importance of the kinetics or order of interactions in multicomponent adsorption.[26-28] [29] For TiO$_2$ specifically, a recent study by Wu et al. investigated the ability of humic acid to displace pre-coated species on TiO$_2$ particles in sequential adsorption experiments. Their findings suggest the displacement of weekly bound smaller organic acids (i.e., ascorbic acid and citric acid) by humic acid, and co-adsorption of a protein (bovine serum albumin (BSA)) and humic acid.[30] Another related study evaluated the competitive adsorption and sequential adsorption of BSA and oxalate (representing dissolved organic carbon) onto TiO$_2$ NPs.[31] To better evaluate the surface coating of the NPs in more realistic conditions, considering the simultaneous exposure of the NPs to different types of the macromolecules as well as the sequential adsorption can be more informative.

Often, the full suite of potential intermolecular interactions (in solution or at the surface) is not explicitly investigated, and hence predicting the adsorption process and resulting corona composition might be more challenging if such interactions are important. This research gap contributes to uncertainty in the prediction of the NP surface chemistry behavior in natural environments and water treatment systems.

1.2.2 Characterization of Active Ingredient Release from Nanocarriers

The use of nanocarriers for applications in drug delivery and agrochemical delivery has gained wide attention due to the utility of the nanoparticle to shield against drug degradation and control the amount and release of the administrated drug, which

4

facilitates targeted drug delivery.[32, 33] In this application, it is required to have a robust and reliable method to detect and quantify the drug loading inside the matrix and subsequently obtain an accurate *in vitro* drug release profile. The majority of the conventional approaches require a separation step for the isolation of unentrapped active ingredients from the nanocarriers, and a subsequent method for quantification of the unentrapped/entrapped compounds. Additionally, these approaches are bulk release assays that do not provide additional information on the particle transformation or release mechanisms. The challenges of conventional approaches and the use of AF4 as a potential solution are further elaborated below.

1.2.2.1. Isolation of the Nanocarriers for Drug Quantification

Conventional methods to obtain release profiles based on the separation of particles from free drugs prior to quantification can result in increased time consumption and low sample recovery and may be applicable to drug release investigation solely in simple media (e.g., buffer). Additionally, the information obtained regarding the release behaviors (extent and rate of release) might be inaccurate; for example, during dialysis, an unavoidable lag time for dissolved drugs to diffuse through the dialysis membrane might be introduced; if this lag time is the limiting rate (i.e., slower than the NP release rate), then the release rate from the NPs can be underestimated. Additionally, centrifugation approaches that apply extensive forces during the NPs separation might also result in underestimating the actual drug loading. Moreover, in these approaches, the indirect quantification of drugs in dialysates or supernatants might not be possible due to sample loss (e.g., adsorption onto centrifuge tubes or the dialysis device).

To address these limitations in dissolution/release investigations, a few studies have proposed new approaches in which the need for particle separation is eliminated. For instance, the applications of drug selective electrodes were demonstrated for investigating the release profile of procaine hydrochloride from microgel,[34] electrochemical probes for detection of doxorubicin release from nanocarriers,[35] or potentiometric sensors for monitoring the dissolution of hydrophobic compounds.[36] Additionally, some studies also applied different spectroscopy or imaging techniques such as attenuated total reflection Fourier transform infrared (ATR-FTIR) spectroscopy,[37] near infrared spectroscopy,[38] Raman spectroscopy,[39] FTIR imaging,[40-42] or UV imaging[43] to monitor the real-time drug release/dissolution from tablets/solids and to investigate further near-surface phenomena in the release process.

Overall, these approaches were able to eliminate the need for separation of the free drug from the particles for further quantification; however, these methods are only applicable to a limited range of studies due to the unavailability of a drug selective electrode/probe/sensor or interference of the NP matrix or biological matrix with the drug quantification.

1.2.2.2. Limited Characterization Information

Common bulk release assays are typically used for studying time-dependent drug release profiles but are not easily able to provide information regarding the size-dependent drug release, the NPs transformations during the release process (e.g., swelling, degradation), or other phenomenological insights regarding the drug release mechanism. One approach that can be applied to investigate the size-dependent release process is to synthesize various batches of the particles with different size distributions.

By comparing the drug release data obtained for each batch, detailed information regarding the size-dependent release behavior and the drug release mechanisms can be obtained. For instance, Berkland et al. studied the release of three model drugs with various hydrophobicity from poly(sebacic anhydride) (PSA) microparticles and concluded that depending on the drug properties by decreasing the size of the microsphere, different size-dependent release rates, ranging from almost no size-dependent release to a slower release, are observed.[44] However, for poly(lactide-*co*-glycolide) (PLGA) microspheres, an increase in the release rate with decreasing size of the microparticles was reported and attributed to an increase in surface area to volume ratio.[45] Other studies involving the synthesis of different size ranges of β-carotene in zein protein,[46] or Rhodamine B loaded nanocapsules,[47] reported a faster release for smaller nanocarriers. In another study, the change in the lysozyme release mechanism (for copolymer microspheres) from zero-order kinetics to Fickian diffusion was reported with a change in particle size.[48]

Overall, to observe size-dependent release behavior, an extensive amount of measurements and sample preparations would usually be required. Therefore, development of an approach that can perform these analyses on a single batch of polydisperse NPs would be novel and valuable. One possible solution to overcome the mentioned limitations (i.e., separation of free drug and no size information) is the coupling or hyphenation of fractionation methods such as asymmetric flow field-flow fractionation (AF4) or capillary electrophoresis (CE) with characterization of the size fractions by various online/offline detectors. For instance, a number of studies have demonstrated the use of separation techniques such as capillary electrophoresis (CE),

coupled to online detectors for investigation of drug encapsulation in liposomes.[49-53] In the next section, we will provide the current state-of-the-art for the use of the AF4 approach for drug release investigations.

1.2.2.3. AF4 and Current State-of-the-art for AF4

Asymmetric flow field-flow fractionation has shown promising results for successful size separation of nanoformulations.[54-56] After separation of the nanocarriers, the drug distributions can be measured *ex situ* by collecting NPs fractions, followed by offline HPLC or liquid chromatography-mass spectroscopy (LC-MS) analysis.[55-57] For example, in a recent study by Hu et al., in addition to evaluation of NP size and morphology, drug distribution across different NP size fractions was achieved by fraction collection from the AF4 followed by offline HPLC analysis.[58] Ansar et al. also applied the AF4 separation technique to doxorubicin liposomal formulations and analyzed the collected fractions at different time intervals for their size distribution, lipid composition, and the ratio of drug to lipid.[57]

In another approach, by coupling AF4 to various online detectors (e.g., UV-Vis, fluorescence detection (FLD)), the separation and characterization of the nanoformulation can be performed simultaneously. For example, Hinna et al. and Fraunhofer et al. investigated the coupling of AF4 with online UV-Vis analysis to probe loading or transfer from liposomal and gelatin NPs, respectively.[59-62] Wankar et al., also by the use of AF4 with an online UV-vis spectrophotometer, confirm the antibiotic loading inside the nanocarriers.[63] The main challenges in the use of UV-vis detection techniques might be the interference of the particle scattering with the UV-Vis measurements for drug detection.[59, 64] Fluorescence detection (FLD) can be used for

8

detection of the fluorophore compounds and as a substitute for UV detection, providing higher sensitivity and selectivity. However, to our knowledge, the applications of AF4-FLD analysis for nanomedicines have been limited to qualitative studies, e.g., by Iavicoli et al. for the binding of fluorophore-tagged peptides to liposomes,[65] de Oliveira et al. to evaluate drug transfer to proteins,[66] or Pound-Lana et al. to investigate the aggregation of the nanoparticles and to monitor the release of lipophilic dye from polymeric nanospheres[67] without detailed quantitative analysis of release profiles.

The other advantage of using size-separation techniques such as AF4 is that by coupling the instrument to online light scattering detectors, the obtained high resolution size-resolved information can enable investigation of phenomena such as degradation or swelling of the particles. This method was previously used for monitoring nanogel degradation during the time under different conditions,[68, 69] investigating the erosion/swelling of thermoresponsive microgels,[70] or self-degradation of drug-loaded polymeric nanoparticles.[71]

Overall, coupling separation techniques with multi-detector analyses for direct quantification of the drug inside the particle can enable rapid generation of "high information" data to overcome limitations of the conventional methods. The sensitive/selective detection of active ingredients directly inside the particles and simultaneous size analysis can enable the size-dependent release analysis and further investigation of the release mechanism and drug distribution by conducting measurements on one polydisperse sample rather than the need for the synthesis of several batches with different sizes.

1.3 Dissertation Overview

This dissertation reports the development of advanced characterization techniques to characterize the surface transformations and molecular release from nanomaterials and the application of these methods to predict competitive adsorption and identify release mechanisms. Three specific research projects are presented with the following objectives: (1) predicting the composition of mixed coronas (protein and NOM) on the surface of TiO_2 NPs for water treatment applications; (2) developing and validating a multi-detector AF4 method for direct monitoring of drug release from polymeric NPs for drug delivery applications; and (3) extending the AF4 method to evaluate formulation purity and NP transformations and to identify release mechanisms via size-dependent release analysis.

The first project is presented in Chapter 2 and investigates the adsorption of two different classes of macromolecules, a protein and natural organic matter (NOM), with titanium dioxide (TiO_2) NPs under competitive and sequential exposure conditions. By fundamentally considering the physicochemical properties of the macromolecules (i.e., size, diffusion coefficient, adsorption affinity) and NPs (i.e., size), the competitive adsorption behavior and, therefore, the composition of the mixed corona can be predicted. Moreover, in this study, the effect of all possible interactions between the macromolecules and the NPs on the adsorption process will be considered. This study will contribute to predict the surface chemistry of the NPs exposed to different macromolecules in more complex environments like water treatment facilities. This chapter of the dissertation is published in *Environmental Science & Technology.*[72]

The second project is presented in Chapter 3 and aims to demonstrate the development of asymmetric flow field-flow fractionation (AF4) coupled with fluorescence detection and multiple other detectors as a novel approach for direct and near-real-time monitoring of fluorescent drug release from polymeric NPs. This new approach can help us to obtain useful information regarding the temperature- and size-dependent release behavior of NPs that can be challenging to measure with conventional methods (e.g., NPs with a high amount of unincorporated drug and with low loading). Overall, this study contributes to providing a new and more robust method to obtain the release profile of small fluorescent molecules from polymeric NPs for drug delivery purposes. This chapter of the dissertation has been submitted for publication.

The third project is presented in Chapter 4 and extends the multi-detector AF4 approach with online total organic carbon (TOC) detection, as well as demonstrates the full capabilities of the approach to distinguish drug release mechanisms. We demonstrate the advantages of TOC over alternative detection techniques such as UV detection for quantification of the NPs as well as free polymers in the matrix. The bulk release profile obtained by the AF4 approach will be validated by solvent extraction techniques. Moreover, by investigating the size-dependent release behavior of a lipophilic dye from polymeric NPs, as well as the drug-loaded NPs (Chapter 3), we will identify the location of the active ingredient carried by the particles (near/at the surface or entrapped inside the particles) to better identify the release mechanism. This chapter is under preparation for submission as a manuscript.

CHAPTER 2. ADSORPTION OF MACROMOLECULE MIXTURES ONTO METAL OXIDE NANOPARTICLES

2.1 Introduction

Engineered nanoparticles (NPs) have gained attention for applications in myriad fields such as water treatment and drug delivery, while concerns for potential environmental risks have also arisen.[73-75] The adsorption of macromolecules to form a coating or corona on the NP surface significantly changes the environmental fate and biological interactions of the NPs,[2, 3, 76-87] and hence surface chemistry is a critical property of the NP. In complex matrices, the corona composition is difficult to characterize or predict. For example, natural organic matter (NOM) or humic substances can show adsorptive fractionation, such that the composition of the adsorbed layer differs from that of the bulk solution,[88-94] and extensive studies on protein corona formation in physiological media have highlighted the dynamic nature of the adsorption process.[82-87] To our knowledge, few studies are available for NPs in environmental media comprising multiple classes of macromolecules, including not only NOM but also proteins, polysaccharides, and other biomolecules.[17, 18] This research gap contributes uncertainty in interpreting NP behavior in complex environmental matrices, when the ultimate NP surface composition is unknown.

Here, we investigate the competitive adsorption of NOM and a protein, bovine serum albumin (BSA), onto titanium dioxide (TiO$_2$) NPs as a model system to identify the mechanisms controlling corona formation on NPs in complex environmental mixtures. TiO$_2$ NPs are photoreactive and hence of interest for water treatment

applications,[13, 95-98] but surface fouling (or corona formation) can modify the effectiveness of the NPs.[99-101] Our long-term goal is to predict the photoreactivity of TiO_2 in complex media. To do so first requires a thorough understanding of the corona formation. To our knowledge, only single-component adsorption of NOM[22, 102-104] or BSA[104-107] onto TiO_2 NPs has previously been evaluated. Adsorption of NOM and protein together has primarily been studied in the soil sciences, where zonal organic matter structures proposed by Kleber et al.[108] were attributed in part to multilayers that form upon sequential adsorption of pure proteins over NOM coatings on mineral surfaces.[109-111] However, in these studies, the influence of solution-phase interactions that can occur between NOM and protein (prior to adsorption) has not yet been fully explored. A recent study by Schmidt et al. identified that solution-phase complexation of BSA onto DNA reduces repulsive interactions to enhance DNA adsorption to goethite surfaces.[112] As proteins also complex with NOM,[113-119] we hypothesize that complexation can influence adsorption from mixtures of NOM and protein onto NPs. A comprehensive understanding of the adsorption process must therefore consider all possible interactions between NOM, protein, and TiO_2 NPs, including those between the uncoated NPs and macromolecules, between NOM and protein in solution (e.g., complexation[114-118]), and between adsorbed and dissolved macromolecules (e.g., displacement[120-122] or multi-layer adsorption[109-111]).

The objective of this study is to achieve a mechanistic understanding of the fundamental processes controlling the adsorption of mixtures of NOM and BSA onto TiO_2 NPs, by investigating solution and surface interactions, as well as the kinetics and history of these interactions. Batch adsorption experiments were evaluated against

theoretical equilibrium and kinetic adsorption models. We then focus on the influence of NOM-protein complexation on the adsorption process, using size exclusion chromatography (SEC) to identify complexation and *in situ* attenuated total reflectance – Fourier transform infrared (ATR-FTIR) spectroscopy to probe competitive adsorption, co-adsorption, or multilayer adsorption phenomena under different NP exposure conditions. We expect this fundamental knowledge will be useful to identify the range of processes that can affect corona formation on NPs in complex environmental media.

2.2 Materials and Methods

2.2.1 Materials

Titanium dioxide (TiO_2) NPs (Standard Reference Material (SRM) 1898) were obtained from the National Institute of Standards and Technology (NIST, Gaithersburg, MD), Suwannee River NOM (Cat. No. 1R101N) from the International Humic Substances Society (IHSS, St. Paul, MN), and bovine serum albumin (BSA, reagent grade pure powder) from Sera Care Life Sciences (Milford, MA). Other reagents are specified in the Appendix A. BSA (1 g/L) and NOM (1 g/L) stock solutions were prepared in Milli-Q water, adjusted to pH 7 using (0.1 or 1) M HCl or NaOH, and allowed to equilibrate overnight to dissolve. Stock solutions were filtered through 0.22 µm polyethersulfone membranes (EMD Millipore, Burlington, MA). Filter loss (to correct subsequent concentrations) was determined against unfiltered stocks for BSA by absorbance at 280 nm on a UV-2600 spectrophotometer (Shimadzu, Columbia, MD) (< 5% filter loss), and for NOM by total organic carbon (TOC) analysis (Xenco

14

Laboratories, Houston, TX) or SEC with refractive index (RI) detection, described in the Appendix A (8% to 10% filter loss). Subsequent samples containing NOM or BSA were prepared in an aqueous buffer of 1.2 mM $NaHCO_3$ and 0.85 mM $CaCl_2$ (pH 7 to 7.5), representing a simplified Environmental Protection Agency (EPA) moderately hard water[123] (matching the total monovalent and divalent cation concentrations using only $NaHCO_3$ and $CaCl_2$), and provides similar pH, bicarbonate, and calcium concentrations to those reported in freshwater systems.[124]

2.2.2 Preparation and Characterization of TiO₂ Suspensions

Stock suspensions of TiO₂ NPs (2 g/L in Milli-Q water) were dispersed using an ultrasonication probe (TM250B Tekmar Sonic Disruptor, Cincinnati, OH) at a measured power[125] of (20 ± 3) W for three 5-min intervals, immediately prior to use. The NPs have reported crystallite particle diameters of (19 ± 2) nm for anatase (comprising 76% of the sample) and (37 ± 6) nm for rutile (comprising 24%).[126] Dynamic light scattering (DLS) measurements (Zetasizer Nano, Malvern Instruments, Westborough, MA) were taken to determine the hydrodynamic size as the *z*-average diameter of (155 ± 11) nm, intensity-average diameter of (182 ± 14) nm, or volume-average diameter of (118 ± 8) nm for stock suspensions diluted to 0.2 g/L TiO₂ NPs in 1 mM NaCl (pH 5.6 ± 0.5), confirming good dispersion of the NPs compared to the reported volume-mean diameter in the NIST SRM 1898 Certificate of Analysis (CoA).[126] After each adsorption experiment, DLS size was also measured directly on samples containing 0.5 g/L NPs in the buffer stated above. A specific surface area of 54 m^2/g reported in the NIST CoA (from Brunauer–Emmett–Teller (BET) analysis) was used to calculate adsorbed masses.

2.2.3 Characterization of BSA and NOM Solutions by SEC

Solutions of BSA and NOM and their mixtures were prepared in the CaCl$_2$/NaHCO$_3$ medium noted above, fixing one species' concentration at 100 mg/L and varying the other from (10 to 200) mg/L. SEC analysis was performed using a Superdex 75 10/300 GL analytical SEC column (GE Healthcare, Chicago, Illinois) on an Agilent 1290 Infinity system comprising a binary pump, degasser, and autosampler (Agilent, Santa Clara, CA). 100 µL of sample was injected. The eluent was 4 mM phosphate (pH 7) with 25 mM NaCl at a flow rate of 0.7 mL/min.[127][128] Similar results were observed in eluent matching the sample buffer (Figure A.2), but column fouling by NOM occurred in Ca^{2+}-containing media. A UV-vis diode array detector (Agilent 1260 UV-DAD), fluorescence detector (Agilent 1260 FLD), and refractive index (RI) detector (Wyatt, Optilab T-rEX) were situated in-line after the SEC column. The DAD monitored absorbance across (200 to 500) nm in 2 nm increments. The FLD monitored the fluorescence of BSA at excitation/emission wavelengths of (295/345) nm.[129] Complexation of NOM onto BSA was evaluated within 1 h of mixing, based on the change in UV and FLD peak areas across the BSA elution time and depletion in RI peak area across the NOM elution time, on duplicate samples. The complexation kinetics of BSA (100 mg/L) and NOM (100 mg/L) were also evaluated.

2.2.4 Batch Adsorption Isotherms

Adsorption isotherms onto TiO$_2$ NPs (0.5 g/L) were obtained in triplicate. Single-component isotherms were collected for initial concentrations of BSA from (60 to 250) mg/L or NOM from (10 to 200) mg/L in the CaCl$_2$/NaHCO$_3$ buffer. The buffer

and adsorbates were mixed, followed by NP addition within 1 h. Samples were covered with aluminum foil and rotated end-over-end at 25 rpm at room temperature for approximately 24 h. Then, 1.5 mL of sample was centrifuged in an Eppendorf Protein LoBind centrifuge tube at 13000 rpm ($12641 \times g$) for 23 min (MiniSpin Plus, Eppendorf, Hamburg, Germany). Supernatant was collected to quantify unadsorbed species. Batch adsorption samples for mixtures of BSA and NOM onto TiO_2 (0.5 g/L) were prepared following the same procedures, fixing the concentration of one species at 100 mg/L while the other was varied from (10 to 200) mg/L.

The adsorbed mass of BSA or NOM was determined by solution depletion, i.e., subtracting the remaining from the initial concentration, and dividing the depleted mass by the estimated TiO_2 surface area from the NIST CoA. BSA was quantified by the Bradford assay (Appendix A);[130] for binary-component solutions, corrections for interferences in the presence of NOM[131] were applied (Figure A.1). NOM was analyzed by SEC with refractive index (RI) detection (method description in Appendix A) to quantify solution depletion and identify adsorptive fractionation of NOM onto TiO_2. Spectral analysis of the NOM by batch- and SEC-UV-vis analysis[132-135] was also performed to evaluate adsorptive fractionation (Appendix A).

2.2.5 Kinetic Adsorption Experiments

In situ ATR-FTIR spectroscopy was used to semi-quantitatively evaluate the kinetics of adsorption, displacement of adsorbed species, and multilayer adsorption processes. A Nicolet iS50 FTIR spectrometer (ThermoFisher Scientific, Waltham, MA) was equipped with a diamond/ZnSe single reflection ATR crystal (PIKE Technologies,

Fitchburg, WI). Spectra were collected from (800 to 4000) cm^{-1} with a resolution of 2 cm^{-1} and averaged over 200 scans. 5 µL of TiO$_2$ (10 g/L in Milli-Q water) was dried onto the ATR crystal, and a flow cell (PIKE Technologies) was attached. Because the background solution chemistry and pH are important,[23, 107, 136] buffer solution with the same composition used in the adsorption experiments was flowed over the NPs to equilibrate the surface chemistry and also remove loosely attached NPs.

Adsorption experiments were conducted separately with pure NOM, pure BSA, or mixtures. For pure NOM or BSA, 100 mg/L solutions in the buffer were flowed over the NPs, and spectra were collected every 10 min and reprocessed using a background spectrum of macromolecule-free buffer over the TiO$_2$ film. We performed the same experiment for NOM-BSA mixtures (100 mg/L of each species), injected after almost 1 hour mixing. To compare relative adsorbed amounts of NOM and BSA from the mixtures, spectra across (1300 to 1800) cm^{-1} were modeled as a linear combination of the single-component adsorbed NOM and BSA spectra to obtain fitted coefficients, A'_{NOM} and A'_{BSA} (details in Appendix A). For this analysis, 1800 cm^{-1} was largely free of NOM or BSA absorbance and selected as a base point to vertically align the spectra before fitting. The ATR-FTIR analysis is only semi-quantitative because of the variable TiO$_2$ film deposited between experiments; hence, fitted coefficients are not compared directly. Only ratios of coefficients, e.g., $\frac{A'_{BSA}(t)}{A'_{NOM}(t)}$, were compared between samples, normalizing the TiO$_2$ surface area and sample volume probed, roughly analogous to the use of internal standards for quantitative FTIR analysis.[137]

Sequential adsorption experiments were performed to evaluate interactions between adsorbed and dissolved macromolecules. Fresh TiO$_2$ NP films were prepared

and equilibrated in buffer, followed by equilibration in NOM (100 mg/L), which was identified in batch experiments to preferentially adsorb. In one experiment, pure BSA (100 mg/L) was then injected over the NOM-coated TiO_2 to identify displacement or overcoating. In other experiments, a mixture of BSA and NOM was injected over the NOM-coated TiO_2, followed by a solution of pure BSA, to distinguish the role of solution-phase mixture interactions on BSA adsorption to NOM-coated TiO_2. Three mixtures were evaluated, BSA (50 mg/L) with NOM (100 mg/L), BSA (100 mg/L) with NOM (200 mg/L), and BSA (200 mg/L) with NOM (100 mg/L).

2.3 Results and Discussion

2.3.1 Batch Single-component Adsorption of BSA and NOM onto TiO_2 NPs

Batch adsorption experiments were performed at pH 7 to 7.5, where the TiO_2 NPs have a $|\zeta| < 20$ mV,[126, 138] and both BSA and NOM are negatively charged (isoelectric point of BSA ≈ 5.1;[139] zeta potential for NOM at pH 7 $\approx$ -40 mV).[102] The adsorption behavior will be determined by attractive forces, including Van der Waals forces, hydrophobic interactions, hydrogen bonding, and Ca^{2+} bridging in our media, as well as repulsive electrostatic and hydrophilic forces. While uncoated TiO_2 NPs aggregate rapidly in this medium, increasing concentrations of BSA and NOM provided steric/electrosteric colloidal stability,[140, 141] as observed by DLS (Figure A.3). Aggregation at lower adsorbate to NP ratios could reduce the available surface area for adsorption, but we obtained similar BSA adsorption isotherms at different TiO_2 concentrations, (0.5 and 1) g/L, suggesting the effect may be minimal. To obtain the entire isotherm with measurable solution concentrations, the initial concentrations of

adsorbate used were higher than typical environmental concentrations, particularly for proteins which represent a small percent of dissolved organic carbon (DOC) in surface waters.[18, 142] However, the lower extent of our remaining (equilibrium) solution concentrations ($\approx$ 4 mg/L) is within the range of higher concentrations observed (e.g., up to 40 mg/L of DOC in wetlands,[18] or (1 to 50) mg/L protein in urban watersheds and wastewater effluents[143-145]).
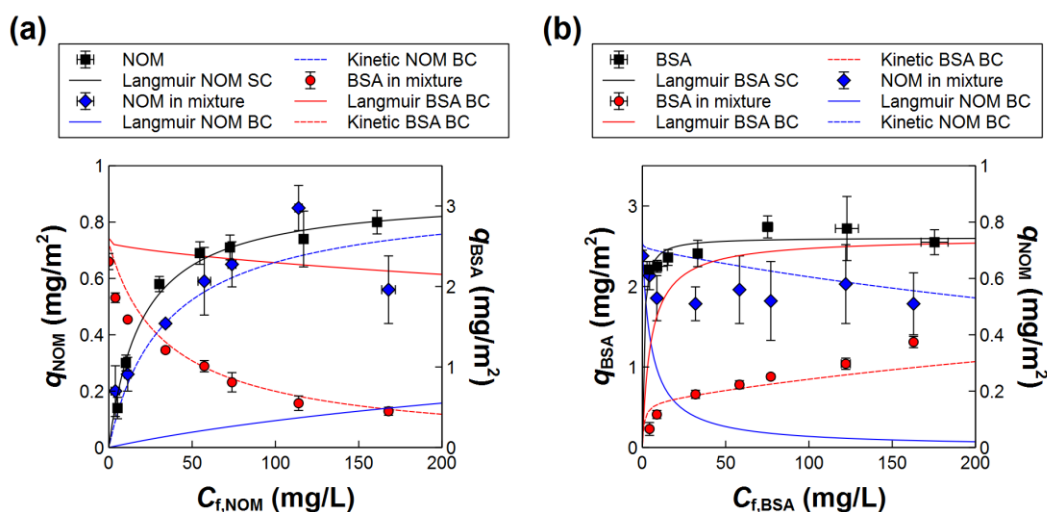
Figure 2.1. Batch adsorption isotherms onto TiO$_2$ NPs for the single-component (SC) solution and binary-component (BC) mixtures of NOM and BSA. Error bars represent the standard deviation of $n = 3$ samples.

A Langmuir adsorption isotherm (Equation A.2) was able to fit the single-component adsorption of BSA and NOM (Figure 2.1), with saturation adsorbed masses, q_{max}, of (2.6 and 0.90) mg/m^2, respectively, fitted by nonlinear regression. These values are higher than other reports, e.g., 1.7 mg/m^2 for BSA at pH 7.3,[146] and $\approx$ 0.2 mg/m^2 for NOM at pH 7,[94] and likely attributable to the presence of Ca^{2+} which enhances both albumin and NOM adsorption to TiO$_2$ by bridging.[147-150] Therefore, we caution extrapolation of results to media lacking Ca^{2+}. The Langmuir isotherm constant, K, for

BSA (1.1 L/mg) was higher than that for NOM (0.051 L/mg). We interpret K only as an empirical fitting parameter indicative of the steeper slope of the BSA isotherm and also note wide 95% confidence intervals on the fitted K for BSA (Table A.1).

We investigated the NOM adsorption in further detail, considering the heterogeneity of the NOM itself. Batch UV-vis absorbance data showed a decrease in the spectral slope of the NOM after adsorption (Figure A.4), indicative of preferential adsorption of higher molar mass species with "activated" aromatic groups (i.e., those with polar ring substitutions, e.g., carbonyl, carboxyl, and ester groups).[134] The SEC analysis (Figure A.5), along with providing adsorbed mass of NOM, confirmed preferential adsorption of higher molar mass NOM, consistent with prior studies.[88-90] The direct relationship between spectral slope and molar mass was also verified by SEC-UV-DAD analysis[133, 135] (Figure A.6). Finally, ATR-FTIR analysis showed that the non-adsorbing, lower molar mass fraction contained higher amounts of functional groups at 1120 cm^{-1} (Figure A.7), which are observed in hydrophilic NOM fractions and attributed to the C-O stretch of alcohol or carbohydrate species.[151, 152] The preferential adsorption was used to inform the properties of adsorbing NOM when parameterizing the competitive adsorption models hereafter.

2.3.2 Batch Competitive Adsorption from Mixtures of NOM and BSA is Kinetically-determined and Monolayer-limited

Adsorption from mixtures of NOM and BSA onto TiO$_2$ was measured in two sets of batch experiments, varying the concentration of BSA in the presence of 100 mg/L NOM, and vice versa (Figure 2.1). NOM largely outcompetes BSA for adsorption,

contrary to expectations from the single-component isotherms. To further explore this phenomenon, experimental observations were compared to two theoretical models, an equilibrium Langmuir adsorption model, and a kinetic adsorption model. Our goal is to identify a simple analytical model capable of describing the competitive adsorption when parameterized using only the single-component Langmuir parameters and known or measured properties of the macromolecules and NPs.

The binary-component Langmuir adsorption model is presented in Equation 2.1[153],

$$q_i = \frac{q_{\text{max},i} K_i C_{\text{f},i}}{1 + \sum_{j=1}^{n} (K_j C_{\text{f},j})} , \tag{2.1}$$

where q_i (mg/m^2) is the adsorbed mass of species i, and $C_{\text{f},i}$ (mg/L) is the final solution concentration of i at the end of the adsorption experiment. $q_{\text{max},i}$ (mg/m^2) and K_i (L/mg) are the maximum monolayer adsorbed capacity and the Langmuir isotherm constant, respectively, from each single-component isotherm. This equilibrium model was not capable of predicting adsorption from the mixtures (Figure 2.1), significantly overestimating the adsorbed mass of BSA relative to NOM. A key assumption of the Langmuir model is that adsorption is reversible, and compounds with higher affinity will displace others to achieve equilibrium. Contrarily, the observed data suggest that our system does not meet Langmuir assumptions.

The alternative limiting case is a kinetic adsorption model in which NOM and BSA adsorb *irreversibly*. Irreversible attachment has been modeled by random sequential adsorption (RSA) models[154, 155] or analogously by colloid deposition

models.[156] For adsorption onto NPs in suspension, the depletion rate of adsorbate from solution, $\frac{dN_\infty}{dt}$, can be described by the Smoluchowski equation[157] with a dynamic site blocking function, $B(\theta)$,[156]

$$\frac{dN_{i,\infty}}{dt} = -\alpha\left[4\pi D(R_1 + R_2)N_{\mathrm{TiO_2}}\right]N_{i,\infty}B(\theta) = -\alpha k_f N_\infty B(\theta), \qquad (2.2)$$

where $N_{i,\infty}$ is the number concentration of macromolecules in bulk solution at time t, D is the summed diffusion coefficients for the macromolecule and NP, R_1 and R_2 are the hydrodynamic radii of the macromolecule and NP, $N_{\mathrm{TiO_2}}$ is the number concentration of TiO$_2$ NPs, α is the attachment efficiency, and θ represents the fractional surface coverage. The diffusion-limited rate coefficient for favorable attachment (no energy barrier) is represented by k_f. Notably, this model will always predict the same final surface coverage at infinite time, regardless of solution concentration. Hence, this model is incapable of predicting the observed concentration-dependent single-component adsorption isotherms without incorporating additional conditions, such as spreading of macromolecules upon adsorption.[158, 159] The paradoxical nature of observing both irreversible and concentration-dependent adsorption has been discussed in the protein adsorption literature.[155, 160]

We do not propose to provide the most complete model to address this scenario but rather to obtain a simple kinetic model capable of explaining our experimental data on final adsorbed layer composition. We proceed by simplifying Equation 2.2 to eliminate the site-blocking function and assume favorable attachment (or equivalent attachment efficiencies for NOM and BSA). Incorporating site blocking requires a numerical solution and will not change the *final* adsorbed layer composition predicted,

23

since the adsorption rates of all adsorbates are affected equally. Obtaining attachment efficiencies would require kinetic data or otherwise treatment of the attachment efficiencies as fitting parameters in the model.

For favorable attachment without site blocking, integrating Equation 2.2 yields Equation 2.3,

$$\ln\left(\frac{N_{i,\infty}}{N_{i,0}}\right) = -4\pi D(R_1 + R_2)N_{\text{TiO}_2}t = -k_f t, \tag{2.3}$$

where $N_{i,0}$ is the initial concentration of species i. The depleted concentration and adsorbed mass of each species at each time t is then obtained by a mass balance. Having eliminated the site blocking function, a stopping criterion is needed to end the adsorption of each species. In defining this criterion, we incorporate concentration-dependent adsorption (i.e., the possibility for undersaturation) by specifying that the adsorption of each species ends when it has reached equilibrium with the surface sites that are unoccupied by the competing species, as defined in Equation 2.4,

$$q_i(t) = \frac{q_{\text{max},i}K_iC_i(t)}{1 + K_iC_i(t)}\left(1 - \sum_{j=1}^{n}\frac{q_{j\neq i}}{q_{\text{max},j\neq i}}\right). \tag{2.4}$$

Equations 2.3 and 2.4 are solved together to obtain different stopping times, $t_{\text{stop},i}$, for each adsorbate. Importantly, the adsorption is made irreversible by holding the adsorbed mass of faster-adsorbing species fixed at $q_i(t_{\text{stop},i})$ for all $t \geq t_{\text{stop},i.}$ Thereafter, the slower-colliding species can continue adsorbing to any remaining available sites until reaching its own stopping time. The final state is at disequilibrium compared to Equation 2.1. Note that if the irreversibility criterion is eliminated and q and C are taken

at equilibrium, Equation 2.4 becomes equivalent to the binary-component Langmuir equation (Equation 2.1).

Overall, this kinetic model predicts the experimental data for the final adsorbed layer composition significantly better than the equilibrium Langmuir model across all mixtures (Figure 2.1). The smaller size (higher diffusion coefficient) and higher number concentration of NOM relative to BSA results in a higher adsorbed mass for NOM than predicted by the Langmuir equilibrium model. Because of the high K parameter for BSA, the model predicts > 80% overall surface saturation for any initial BSA concentration > 1 mg/L (in the presence of 100 mg/L of NOM). The key assumptions of irreversible and monolayer-limited adsorption in this model were then directly tested in ATR-FTIR experiments.

2.3.3 Multilayers Form Upon Sequential Exposure of TiO$_2$ NPs to Pure NOM and Pure BSA

In situ ATR-FTIR spectroscopy has previously been applied to evaluate the adsorption of BSA,[105, 107, 136, 161] NOM,[23] polymers,[162] and other compounds[163-165] onto TiO$_2$ and other surfaces.[165-168] This method allows semi-quantitative analysis of the kinetics and extent of adsorption onto NPs. First, individual spectra of adsorbed NOM or BSA were collected during adsorption to the TiO$_2$ NP film from 100 mg/L solutions (Figure A.8). The strong peaks at (1410 and 1570) cm^{-1} for adsorbed NOM are likely attributable to deprotonated carboxyl groups (–COO$^-$)[169] [170] and also include contributions from aliphatic hydrocarbons[152, 171] and aromatic alkenes,[152, 171] respectively, that absorb in these regions. Consistent with our batch fractionation results

(Figure A.7), the peak at 1125 cm^{-1} (C-O stretch of carbohydrates) in the < 10 kDa NOM fraction was not observed in the adsorbing NOM. For BSA, the two main peaks correspond to amide I at (1600 to 1700) cm^{-1} for C=O stretching, and amide II at (1500 to 1600) cm^{-1} for N-H bending and C-N stretching.[171,172]

Then, a sequential adsorption experiment was performed in which the surface of the deposited NPs was equilibrated with NOM (100 mg/L) as the kinetically-favored adsorbate, followed by pure BSA (100 mg/L). To quantify adsorption of multiple species, previous studies used peak heights when peaks did not overlap significantly for adsorbed protein[173] and other compounds.[112] Here, the broad bands for NOM and BSA overlap extensively, but peak locations did not shift significantly in mixed layers compared to the single-component adsorption. Hence, the mixed layer spectra were successfully modeled as a linear combination of the single-component adsorbed BSA and NOM spectra in the range of (1300 to 1800) cm^{-1} (Equation A.6, Figure A.9). The fitted coefficients, A'_{BSA} and A'_{NOM}, are only semi-quantitative but can be evaluated for trends in the adsorbed mass of each species within each experiment or when ratioed to normalize for TiO$_2$ surface or sample volume probed.

While in other cases, surface ligands with low affinity have been found to be displaced by higher affinity species,[171] results here agree with adsorption irreversibility, the adsorbed amount of NOM remained nearly constant during the subsequent adsorption of BSA (Figure A.9). More notably, the extensive BSA adsorption suggests that pure BSA significantly overcoats adsorbed NOM, similar to other sequential adsorption experiments reporting multilayer formation of pure proteins onto humic-coated minerals.[109-111]

Comparing the batch (mixture) and *in situ* ATR-FTIR (sequential) adsorption, the formation of NOM-protein coronas on TiO_2 NPs then appears to be fundamentally different when the NPs are exposed to a mixture (monolayer restriction) *versus* sequential exposure to pure solutions (multilayer adsorption). To explain these contradictory behaviors, we hypothesize that intermolecular complexation between humic substances and proteins in solution, well-known to occur,[114-118] changes adsorption from mixtures compared to pure substances. Hence, we investigated the role of intermolecular interactions through additional SEC and *in situ* ATR-FTIR experiments.

2.3.4 Solution-Phase Complexation Occurs Between BSA and NOM

SEC experiments were performed to evaluate complexation interactions between NOM and BSA in the solution phase. BSA elutes from the SEC column from $\approx$ (11 to 18) min as two peaks, corresponding to BSA dimer and monomer, which were considered together in the analyses. NOM elutes primarily as a broad peak from $\approx$ (15 to 26) min. Upon increasing the ratio of NOM to BSA in solution, UV absorbance and RI in the BSA region increase significantly (Figure 2.2), indicating attachment of aromatic NOM species onto BSA. Complexation also quenches the BSA fluorescence, consistent with previous reports[174] and possibly indicative of binding of the NOM with fluorescent tryptophan residues in BSA or a change in BSA conformation. As with adsorption to the TiO_2 NPs, NOM with higher molar masses have slightly higher affinity to complex with BSA. The amount of NOM attached to the BSA estimated by SEC-RI

analysis showed increasing complexation with the ratio of NOM:BSA, and complexation was observed to proceed over ≈ 5 h before equilibrating (Figure A.10).
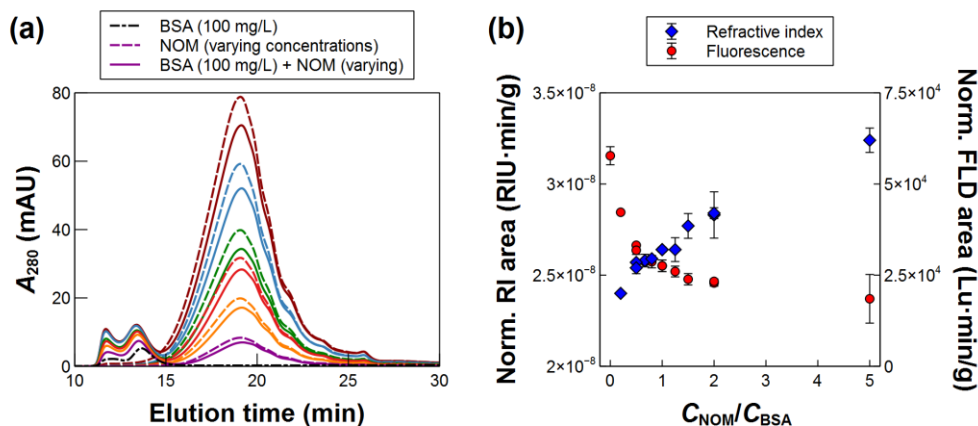
Figure 2.2. SEC-UV$_{280}$ chromatograms (a) and normalized RI and FLD peak area to injected BSA mass for BSA-NOM mixtures (b). The chromatograms were collected for BSA, NOM (20, 50, 80, 100, 150, 200 mg/L), and their mixtures.

2.3.5 Co-adsorption is Followed by Suppressed Multilayer Formation in Simultaneous Adsorption from NOM-BSA Mixtures onto TiO$_2$ NPs

In situ ATR-FTIR was used to investigate the simultaneous adsorption of NOM and BSA onto TiO$_2$ NPs and evaluate the effects of complexation in solution on the adsorption from NOM-BSA mixtures onto TiO$_2$ NPs. First, simultaneous adsorption of BSA (100 mg/L) and NOM (100 mg/L) onto the *uncoated* TiO$_2$ was evaluated. While both species increasingly adsorb over time, the ratio of adsorbed BSA to NOM decreases over the first hour (Figure 2.3). This trend can be explained either by a lower affinity of BSA to adsorb upon complexation, or increasing co-adsorption of NOM with BSA as it complexes to BSA over ≈ 5 h at the concentrations used here. Batch adsorption experiments using isolated NOM-protein complexes suggested that complexation does

not largely suppress BSA adsorption onto *uncoated* TiO$_2$ (Figure A.11); hence, co-adsorption of NOM complexed with BSA may contribute more to the results observed in the initial stage of adsorption to the uncoated TiO$_2$ NPs.
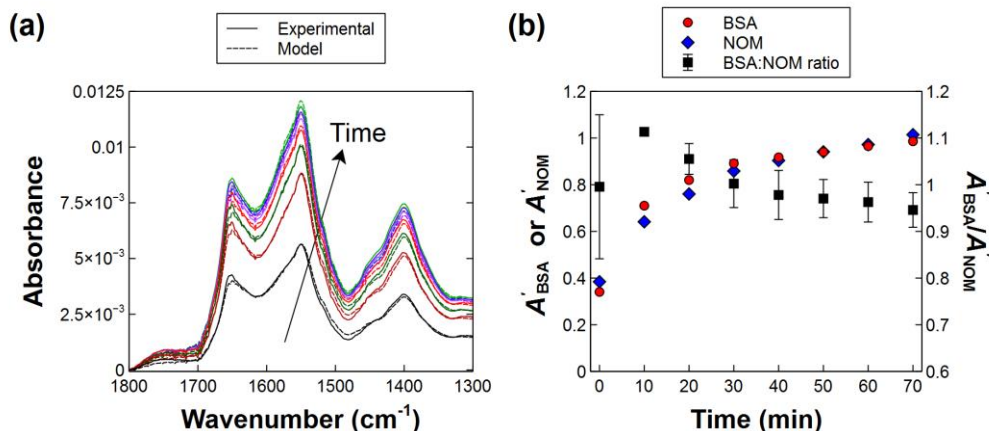
Figure 2.3. *In situ* ATR-FTIR experiment for simultaneous adsorption from mixtures of BSA (100 mg/L) and NOM (100 mg/L) onto TiO$_2$ NPs in the same buffer as the batch adsorption experiments.

The larger picture from the mixture experiment is that the overall BSA adsorption does indeed appear to be suppressed in the mixture relative to pure BSA, specifically, BSA adsorption begins to plateau within 1 h in the mixture (Figure 2.4), but remains nearly linear over 1 h when adsorbing from pure solution even after NOM has pre-adsorbed (Figure A.9). We hypothesize that over longer time scales, complexation of NOM onto dissolved BSA hinders the ability of BSA to overcoat adsorbed layers *after* the TiO$_2$ surface has been saturated. To test this hypothesis, adsorption from NOM-BSA mixtures onto NOM-coated TiO$_2$ NPs was evaluated (Figure 2.4 and A.12) and compared to subsequent adsorption of the pure BSA for various concentrations of BSA and NOM. In all cases, after providing adequate opportunity for adsorption from the NOM-BSA mixtures, subsequent injection of pure

BSA led to further protein adsorption beyond that in the mixtures. Hence, adsorption sites must be available to pure BSA that are not available to the complexed BSA. We propose that the complexed BSA fills remaining bare TiO_2 sites (since NOM is not completely saturated from 100 mg/L starting conditions), but has little affinity to overcoat the adsorbed NOM after complexing with NOM in solution. On the contrary, the pure BSA is capable to attach onto the adsorbed NOM to form an overcoating. While modeling this behavior without more quantitative kinetic data is outside the scope of this study, possible extensions to the kinetic model are discussed in the Appendix A that could describe this multilayer formation.
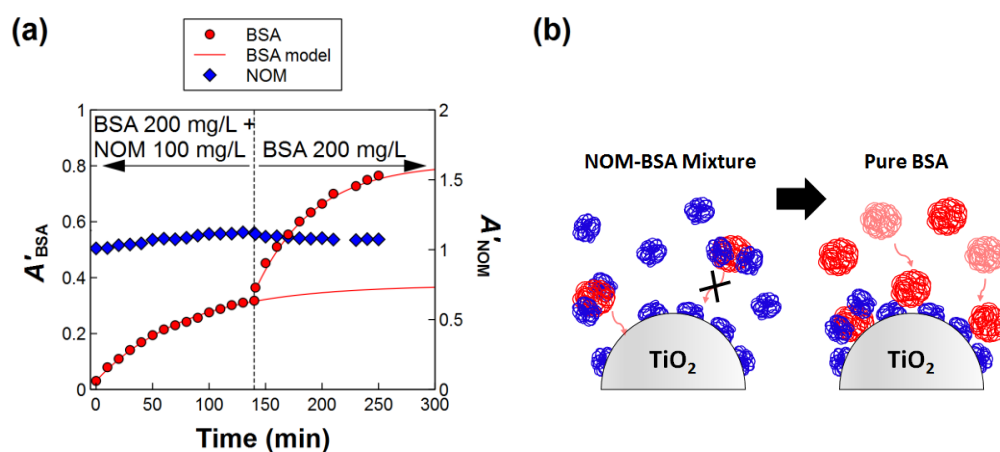
Figure 2.4. *In situ* ATR-FTIR experiment for the sequential adsorption of a mixture of BSA and NOM, followed by pure BSA, onto NOM-coated TiO_2 NPs (a) and the proposed conceptual model (b).

In summary, the complexation interaction between NOM and BSA is a critical process leading to the occurrence of fundamentally different adsorption phenomena under different NP exposure conditions and time scales, as depicted in Figure 2.5. Multilayer formation occurs upon sequential exposure to *pure* solutions of NOM and BSA. In mixtures, BSA-NOM complexes can co-adsorb to the *uncoated* TiO_2 at short

time scales. However, after the TiO_2 surface is saturated, the complexation of NOM to BSA in solution ultimately hinders any further development of NOM/protein multilayers on the TiO_2 NPs, such that monolayer restrictions are reasonable when modeling batch adsorption from mixtures (Figure 2.1). Notably, in this system, all possible mixture interactions (macromolecule–NP, macromolecule–macromolecule, and macromolecule–adsorbed layer) and their kinetics are important.
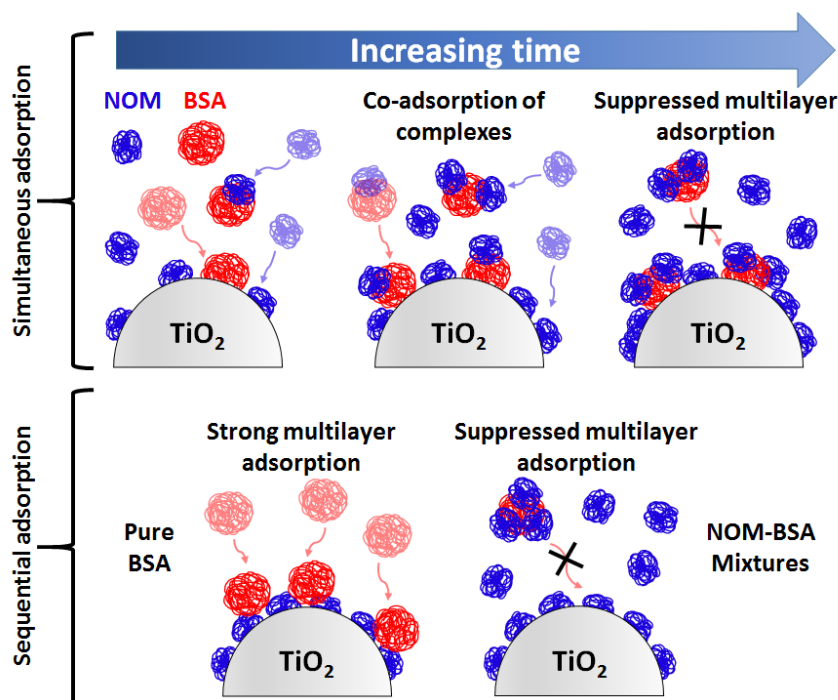
Figure 2.5. Conceptual model for competitive adsorption of NOM and BSA onto TiO_2 NPs, accounting for the critical role of dynamic intermolecular interactions.

2.4 Conclusions and Implications

This study has presented a thorough investigation of the fundamental mechanisms involved in the competitive adsorption of NOM and proteins (with BSA as a model protein) onto TiO_2 NPs, using both modeling and experimental methods to fully evaluate the adsorption process under a range of possible NP exposure conditions. The

behaviors observed here further expand our understanding of the role of mixture interactions and kinetics on corona formation in environmental media. Just as protein corona formation in biological systems is well known to be a dynamic process, so will prediction of heterogeneous corona formation in environmental systems require knowledge of not only the matrix and NP composition, but also the intermolecular interactions in solution and at the NP surface, and the kinetics and history of these interactions.

To our knowledge, this study is the first to directly identify the roles of both dynamic complexation in solution and the history of the NP surface on the competitive adsorption process in environmental matrices containing mixtures of NOM and protein. The influence of sequential exposure observed here will be most relevant during transport of NPs between environments, e.g., from surface water to a biofilm layer concentrated in proteins, or bio-uptake, where an NOM-coated NP can obtain a protein corona. Diurnal or seasonal patterns also produce fluctuations in the composition of organic matter in natural and engineered water treatment systems.

Additional research is needed to evaluate generalizability from the single solution chemistry and high adsorbate and NP concentrations in this study. The presence of Ca^{2+} in our samples likely enhanced the adsorption of both proteins and NOM onto TiO_2, and hence the adsorbed masses and adsorption irreversibility may change in media lacking Ca^{2+}. pH and ionic strength also change the NP surface charge or screens charges, affecting adsorption. Using our simple kinetic model to extrapolate to lower mixture concentrations (e.g., < 10 mg/L of both adsorbates), NOM is still predicted to outcompete such that the BSA adsorbed mass is relatively sensitive to the NOM

32

concentration, whereas NOM adsorption is relatively insensitive to the presence of BSA. However, experiments are needed to confirm. Such studies should address whether long-term conditioning of NPs in lower, environmentally relevant macromolecule concentrations (but relatively high concentrations compared to relevant NP concentrations, i.e., minimal solution depletion) would result in similar adsorbed layers to those measured at high concentrations. True adsorption irreversibility would suggest that the final corona should not depend on absolute concentrations given sufficient time for adsorption.

We anticipate systematic investigations for mixtures of macromolecules covering a range of physicochemical properties (e.g., humic substances, proteins, polysaccharides, lipids, DNA, etc.) will enable elucidation of overarching rules to predict competitive adsorption onto NPs and other surfaces in complex environmental media. Future studies are needed to evaluate how the corona compositions and structures formed under different conditions will affect subsequent NP behavior in the environment. Most notably, we identified that exposure of the NP to a homogeneous mixture of NOM and proteins that have already undergone complexation will produce only a thin monolayer coating, whereas sequential or alternating exposures of the NP to different ratios of NOM and protein can result in multilayer coatings. The corona thickness and adsorbed mass are known to dominate the steric or electrosteric repulsion between NPs,[81, 175] and hence our study suggests that the details of the history of NP exposure to various macromolecules can be important to the overall fate and transport of the NPs. Corona composition, structure, and thickness are also likely to change the reactivity of NPs, including photoreactive TiO_2 NPs,[99-101] where the adsorbed

macromolecules will interact with both organic pollutants and reactive oxygen species. Finally, the degradation of the corona and transformation of the NP itself can also vary with corona composition, leading to longer-term differences in NP fate and transport.[176-178] The thoroughly characterized system presented here will be useful to investigate the effect of the composition and structure of NOM/protein coronas on the photoreactivity of TiO_2 NPs and reactive transformations of the corona.

CHAPTER 3. NOVEL METHODS FOR CHARACTERIZATION OF DRUG RELEASE FROM POLYMERIC NANOPARTICLES

3.1 Introduction

Drug entrapment in polymeric nanoparticles (NPs) is a well-known approach to enhance drug efficiency by controlling the drug transport, uptake, and release.[4, 179-181] Potential benefits conferred by drug entrapment include reduction in drug administration frequencies, decreased toxicity to cells, and targeted delivery.[182-186] Accurate characterization of the drug distribution (entrapped versus dissolved) and release profile is crucial to understand or predict the performance of drug-loaded NPs, with release profile being one of the key quality attributes specified in U.S. Food & Drug Administration (FDA) guidelines for evaluation of nanomaterial-based drugs. [187] The shape of the release profile also provides critical insight into the mechanism of release, for example by diffusion or swelling.[188] Finally, the dependence of the release behavior on the environmental conditions such as pH, temperature, or media composition provides insight into the material properties and interactions.[189, 190] For example, heating a polymeric nanoparticle beyond its glass transition temperature (T_g) is expected to result in higher diffusion and release rates of drugs from the polymeric matrix.[189, 191, 192] Methods to obtain release profiles should hence be robust to accurately evaluate drug release across a variety of release conditions.

Direct measurements of the drug entrapped within the NPs (Figure 3.1a) can be advantageous to monitor drug loading and release over conventional dialysis experiments (Figure 3.1b), in which the dissolved drugs are quantified in the dialysate,

e.g., by high performance liquid chromatography (HPLC), or the total drug in the retentate (dissolved and entrapped) is measured by extracting or dissolving the NPs in an organic solvent for drug quantification. Dialysis introduces an unavoidable lag time for dissolved drugs to diffuse through the dialysis membrane; if this lag time is the limiting rate (i.e., slower than the NP release rate), then the release rate from the NPs can be underestimated. For example, using a drug-selective electrode to eliminate the dialysis lag time found a faster release from microgels than dialysis.[34] Furthermore, a "burst" release of unincorporated or loosely-bound drugs is commonly noted, particularly for poly(lactic-*co*-glycolic acid) (PLGA) nanomedicines.[193] The diffusion profile of the "burst" drugs from the dialysis bag will be superimposed over that of the entrapped drugs, obscuring both the extent and rate of release from within the NPs. Methods to directly probe *only* the entrapped drug in the NPs in "real time" (i.e., without any separation lag) would be advantageous to eliminate these artifacts.
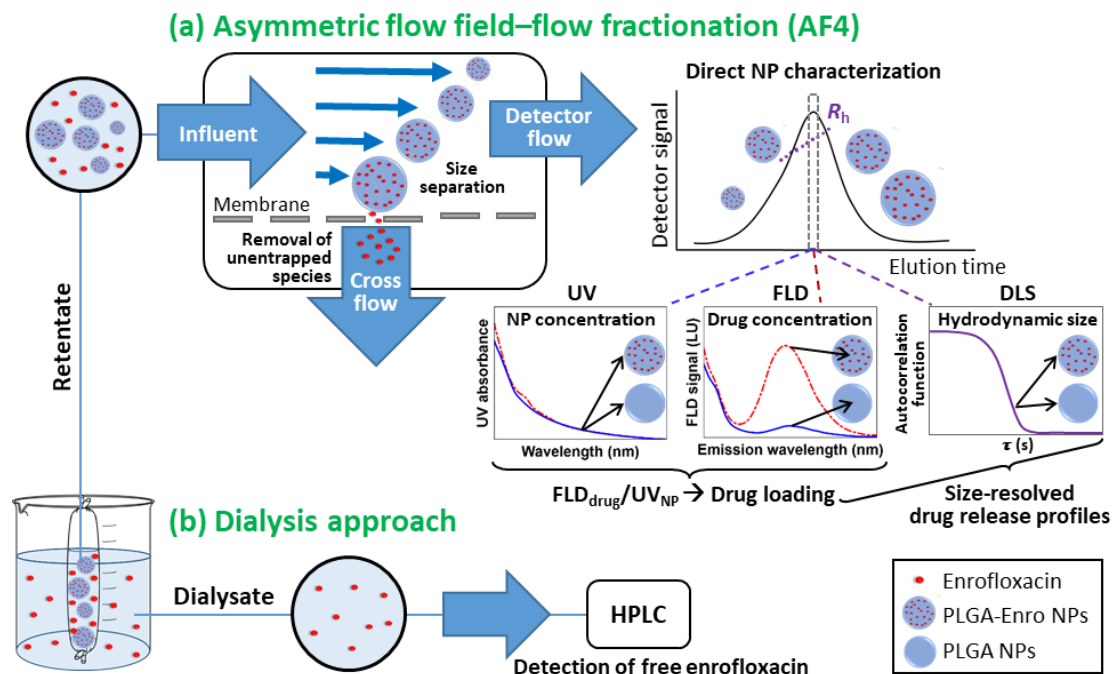
Figure 3.1. Schematic comparing asymmetric flow field–flow fractionation (AF4) (a), and dialysis (b). AF4 provides *in situ* purification of unentrapped drugs, followed by size separation and direct characterization of NPs.

Asymmetric flow field–flow fractionation (AF4) is proposed here to provide real-time separation of entrapped and dissolved drugs and direct analysis of only the entrapped drugs (Figure 3.1a). The principle of AF4 is discussed in previous texts; [194-200] briefly, injected particles are first "focused" toward an ultrafiltration membrane. Then, an applied crossflow establishes a force field, in which smaller particles (with higher diffusion coefficient) equilibrate toward the middle of the AF4 channel (with maximum velocity) and elute sooner than larger particles. AF4 hence provides immediate washing of dissolved species through the membrane during focusing, in addition to NP size separation. NP sizes, compositions, and concentrations can then be characterized by coupling AF4 to various detectors.[54, 201] In the vast majority of applications, AF4 has been coupled with light scattering to obtain size distributions of

polymeric NPs[202-208] or with inductively coupled plasma mass spectrometry (ICP-MS) for inorganic NP speciation.[209-214] Few studies have applied AF4 to assess the loading of organic drug molecules in polymer NPs. Drug distributions can be measured *ex situ* by collecting AF4 fractions, followed by offline HPLC or liquid chromatography-mass spectroscopy (LC-MS) analysis.[55-57] For direct drug detection, Hinna et al. and Fraunhofer et al. investigated the coupling of AF4 with online UV-Vis analysis to probe loading or transfer from liposomal and gelatin NPs, respectively.[59-62] In these UV-Vis measurements, particle scattering prevents a severe and unavoidable interference to drug detection.[59, 64] Hence, drug can only be observed if it is present in high concentrations or has a unique absorbance feature (e.g., in the visible light region). For quantitative analysis, corrections must be made to subtract the particle scattering interference; these corrections are unreliable when the drug signal is low relative to the particle scattering background (Figure 3.1), making drug quantification infeasible by UV-Vis detection for NPs that are large (i.e., high scattering intensity) and have low drug loading [59]. Furthermore, the light scattering contribution depends on the particle size and concentration (which can vary across the chromatographic peak and between samples), adding further uncertainty to the interference correction.

Fluorescence detection (FLD) is a more sensitive and selective alternative to UV detection for fluorescent or fluorescently-labeled compounds.[215-217] Notably, of the 12 currently FDA-approved liposomal and protein-based nanoparticles for drug delivery, 11 of the drug compounds are inherently fluorescent and could be amenable to AF4-FLD analysis.[218] However, while AF4 has been coupled with FLD to characterize macromolecules[219] such as humic substances,[220-223] proteins,[215, 216, 224] and

biopolymers,[225] it has not yet been used to quantify drug release from nanomedicines. Applications of AF4-FLD analysis for nanomedicines have been limited to qualitative studies, e.g., by Iavicoli et al. for the binding of fluorophore-tagged peptides to liposomes[65] or by de Oliveira et al. to evaluate drug transfer to proteins[66], without quantitative analysis of release profiles. In addition to applying AF4-FLD for quantification, we further propose that combining AF4 for NP size separation with FLD for drug quantification can enable unique measurements of size-resolved drug release profiles that would be impossible to achieve with AF4-UV detection, where different size particles would contribute different scattering interferences in the drug quantification.

The objective of this study is to demonstrate the novel development of an AF4-FLD method for the acquisition of direct, real-time, size-resolved release profiles of fluorescent drugs from polymeric NPs. Here, enrofloxacin-loaded poly lactic-*co*-glycolic acid (PLGA) NPs are evaluated as a model system,[186] where PLGA is one of the most common polymers for drug delivery systems,[182, 183, 226] and enrofloxacin is a fluoroquinolone antibiotic with inherent fluorescence. First, method development is demonstrated on coupling AF4 with FLD and UV detection to selectively quantify the entrapped drug by FLD and the overall PLGA NP concentration by UV (and hence quantify the drug loading), along with online multi-angle light scattering (MALS) and dynamic light scattering (DLS) detectors to acquire NP size distributions and shape factors. Then, the AF4 method is applied to evaluate the size- and temperature-dependent drug release from the NPs, and the AF4 results are compared and validated against conventional dialysis experiments. A diffusion model is applied that explicitly

considers both diffusion barriers (through the polymeric matrix, and across the dialysis membrane) to integrate the AF4 and dialysis data and quantify release rates. This study ultimately demonstrates the first proof of concept of AF4-FLD to monitor drug release from polymeric NPs and the significant and unique advantages achieved over alternative methods.

3.2 Materials and Methods

3.2.1 Materials

Poly lactic-*co*-glycolic acid (PLGA, 50:50 lactide:glycolide, 38 to 54 kDa), poly (vinyl alcohol) (PVA, 31 to 50 kDa), Tween 80, and enrofloxacin from Sigma Aldrich (Millipore Sigma, St Louis, MO, USA), as well as ethyl acetate (ACS grade, $\geq$99.5%, Fisher Scientific Co, Hampton, NH, USA) and trehalose dihydrate ($\geq$98%, Fisher Scientific Co, Hampton, NH, USA), were used in the NP synthesis. Enrofloxacin (Alfa Aesar, Ward Hill, MA, USA) was used as the model fluorescent drug. Enrofloxacin is only moderately hydrophobic, with a solubility limit of 145.8 mg/L and 181.9 mg/L in water and 0.1 M phosphate buffer (pH 7.4),[227] respectively, and reported octanol-water partitioning coefficients (log P) of 0.24 to 1.1.[228]

Potassium phosphate monobasic anhydrous, sodium phosphate dibasic heptahydrate (both ACS grade, Amresco, Solon, OH, USA), sodium chloride ($>$ 99.0%, ACS grade) from Sigma Aldrich (Millipore Sigma, St Louis, MO, USA), and potassium chloride (99.999%, trace metal basis, Acros Organics, Morris Plains, NJ, USA) were used to prepare phosphate buffered saline (PBS, 137 mM NaCl, 2.7 mM KCl, 10.1 mM Na_2HPO_4, 1.8 mM KH_2PO_4, pH 7.4). Phosphoric acid (85%, ACS grade, Ricca

Chemical Company, Arlington, TX, USA) and acetonitrile (Chromasolv Plus, for HPLC, >99.9%, Honeywell Riedel-de Haen, Seelze, Hanover, Germany) were used for HPLC mobile phase preparation.

3.2.2 NPs Synthesis

The NPs were synthesized by emulsion evaporation similarly to our prior work except substituting the PVA surfactant with Tween/PVA.[186, 229] Briefly, for the enrofloxacin-loaded PLGA NPs (denoted hereafter as "PLGA-Enro NPs"), the organic phase was prepared by dissolving 420 mg of PLGA and 39 mg of enrofloxacin in 10 mL of ethyl acetate under stirring (400 to 500 rpm) for 30 minutes. The aqueous phase was prepared by dissolving Tween 80 in 110 mL of low resistivity water to obtain a final concentration of 5 mg/mL. Next, the organic phase was poured into the aqueous phase under stirring (400 to 500 rpm), and the emulsion was passed four times in a microfluidizer (M 110P, Microfluidics, Westwood, MA, USA). Next, the organic solvent was evaporated in a rotavapor (Buchi R-300, Buchi Corp., New Castle, DE, USA) under vacuum at 32 °C for 70 minutes. Then, the polymeric NP suspension was mixed with 9 mL of 2.0% (w/v) of PVA solution prepared in advance with water of low resistivity. Finally, the suspension was mixed with trehalose in a mass ratio of 1 to 1 and freeze dried (FreeZone 2.5, Labconco Corp., Kansas City, MO, USA) at -80 °C for two days. The samples were stored at -20 °C for testing and characterization purposes. "Empty" PLGA NPs were synthesized following the same method with the exclusion of enrofloxacin. The mixtures did not undergo purification steps prior to lyophilization, and hence the total concentration of enrofloxacin in the lyophilized PLGA-Enro powder

was 1.64% (w/w). The NPs were synthesized as three separate batches. The NPs synthesis were performed by Dr. Carlos E. Astete and Dr. Cristina M. Sabliov.

3.2.3 NPs Characterizations

Transmission electron microscope (TEM) images of PLGA-Enro and empty PLGA NPs were obtained using a JEOL JEM-1400 series 120kV (JEOL USA Inc., Peabody, MA, USA). The NP sample was mixed with a contrast agent (uranyl acetate) before placing one droplet over a carbon copper 300 grid. The sample was dry before placing in the microscope chamber. TEM images are presented in the Appendix B Figure B.1. TEM measurements were conducted by Dr. Carlos E. Astete.

Attenuated total reflectance – Fourier transform infrared (ATR-FTIR) spectra of the NPs and their individual component materials were collected on a Nicolet iS10 FTIR spectrometer (ThermoFisher Scientific, Waltham, MA, USA). Each material was applied onto the surface of a Ge ATR crystal. Spectra were collected as the average of 96 scans from 800 cm^{-1} to 4000 cm^{-1} with a resolution of 4 cm^{-1}, with the clean ATR crystal spectrum background subtracted from each sample spectrum (Figure B.2).

The glass transition temperature (T_g) of the NPs was measured by modulated differential scanning calorimetry (MDSC). The measurements were obtained on a TA Instruments DSC (model Q200, TA Instruments, New Castle, DE, USA). The DSC experiments were performed with 5 to 10 mg of sample using standard aluminum pans. The sample compartment was purged with nitrogen (gas flow 50 mL/min) during the experiment. The procedure was as follows: (1) cool down sample to -40 °C; hold isothermal at this temperature for 5 min; (2) modulate +/- 0.80 °C every 60 seconds; (3)

hold isothermal for 5 min; and (4) ramp 5.00 °C/min to 80.00 °C. The T_g and onset and offset points were calculated using the inflection point method using the Reverse Heat Flow Signal (Figure B.3).

Finally, batch DLS and electrophoretic light scattering measurements of size and zeta potential, respectively, were collected on a Malvern Zetasizer Nano ZS instrument (Malvern Panalytical Inc., Malvern, UK). In addition to measurements of the initial NP suspensions, the PLGA-Enro NPs were evaluated for any changes over the release experiments by collecting NPs dialyzed in PBS at 37 °C (see Section 3.2.5). Zeta potential measurements were conducted in folded zeta capillary cells (DTS 1070, Malvern Panalytical Inc., Malvern, UK) and computed from the electrophoretic mobility using the Smoluchowski model. The average and standard deviations across five measurements are reported. To reduce electrode corrosion in the presence of PBS during the zeta potential measurements, the applied voltage was set to 100 V and the PBS suspensions of the NPs were diluted to 0.5 g/L NPs in deionized water for the batch measurements (no significant difference in zeta potential was observed if NPs were diluted into PBS).

3.2.4 Enrofloxacin Entrapment Efficiency

Centrifugation and centrifugal ultrafiltration methods were compared to separate entrapped and dissolved drug to calculate the entrapment efficiency of drug in the PLGA-Enro NPs. In the first approach, samples were centrifuged for 15 min at 13000 rpm (maximum relative centrifugal force (RCF_{max}) = 11337g, MiniSpin Plus, Eppendorf, Barkhausenweg, Hamburg, Germany), and the supernatants were collected

and filtered through 0.22 μm polytetrafluoroethylene (PTFE) membranes (MicroSolv Technology, Leland, NC, USA). In the second approach, the samples were filtered in pre-washed 100 kDa Amicon Ultra-4 centrifugal filters (EMD Millipore, Burlington, MA, USA) at 4500 rpm (RCF$_{max}$ = 4415g) for 8 min (Sorvall Legend XTR Centrifuge, ThermoFisher Scientific, Waltham, MA, USA), and the filtrate was collected for analysis. The entrapped drug concentration was obtained by subtracting the supernatant or filtrate concentration (measured by HPLC analysis, Section 3.2.7) from the total concentration of enrofloxacin. In both methods, control experiments (enrofloxacin only in PBS) were performed to assess losses during the sample preparation. For the NP samples, standard additions were performed in which 1 mL of dissolved enrofloxacin (at different concentrations) was added to 3 mL of the lyophilized powder dispersed in PBS at a concentration of 0.5 g/L of PLGA-Enro NPs (1 g/L of total powder including trehalose) to further assess and correct for matrix effects due to the NPs and other excipients in the nanoformulations.

3.2.5 Release Experiments

Release experiments were conducted using a stock suspension of PLGA-Enro NPs, prepared at 7.5 g/L of NPs (15 g/L of powder including trehalose) in PBS (pH 7.4) with bath sonication for 10 seconds (Branson 1800, Emerson, St. Louis, MO, USA). 1 mL of the NP suspension was added to a 1 mL dialysis device (Spectra/Por Float-A-Lyzer G2, molecular weight cut-off (MWCO) 100 kDa, cellulose ester), which was prewashed following the manual. The MWCO was chosen to be much higher than enrofloxacin to improve drug diffusion from the dialysis device into the reservoir.[34, 230]

No significant loss of the enrofloxacin to the dialysis device was observed. Release experiments were conducted at three different temperatures, (20 ± 1) °C (i.e., room temperature), (30 ± 1) °C, and (37 ± 1) °C. The room temperature was measured by a thermometer held inside the water bath, and the higher temperatures were achieved in a heated bath sonicator (Branson 1800, Emerson, St. Louis, MO, USA) without sonication. The dialysis device was floated in a closed (screw-cap) reservoir containing 120 mL fresh PBS preheated and equilibrated for 24 h in advance. At each time point, for AF4 measurements, 20 μL of NPs from inside the dialysis device was diluted with 280 μL PBS to obtain a final concentration of 0.5 g/L of NPs (1 g/L of powder including trehalose), then immediately injected to the AF4 instrument (Section 3.2.6). Simultaneously, for HPLC measurements, 0.4 mL of liquid from the reservoir was collected and substituted with 0.4 mL fresh PBS and held refrigerated for further quantification by HPLC (Section 3.2.7). Because samples were removed from inside and outside the dialysis device for analysis, the mass of NPs and drug in the system is depleted between each measurement. As such, the released concentration obtained by HPLC was corrected to account for sample removal (details in the Appendix B). All results reported are the average and standard deviation of experiments on three independently synthesized NP suspensions.

Because a burst release is expected to significantly impact measurements of free drug appearing in the dialysate but not the entrapped drug measurement by AF4-FLD, release measurements were also performed on purified PLGA-Enro NPs at 30 °C to validate this hypothesis and interpretation of the results, with purified NPs prepared by dialyzing the NPs at room temperature as described in the Supporting Information.

45

Finally, control release experiments were performed for enrofloxacin alone (249 mg/L) in PBS, as well as a mixture of empty PLGA NPs (7.5 g/L as NPs) and enrofloxacin (249 mg/L) in PBS, at the three temperatures above to obtain the diffusion rates of the dissolved drug from the dialysis device.

3.2.6 AF4 Method for Direct Analysis of NPs

The AF4 module (Eclipse AF4, Wyatt Technology, Santa Barbara, CA, USA) was integrated with an Agilent 1290 Infinity HPLC system (Agilent Technologies, Santa Clara, CA, USA) comprising a binary pump, degasser, and autosampler. The Eclipse AF4 short channel was prepared with a spacer height of 250 μm and 10 kDa regenerated cellulose (RC) membrane. The full AF4 method is presented in the Appendix B Table B.1. Briefly, the mobile phase was the same PBS as the dialysis media, detector flow rate was 0.5 mL/min, and total run duration was 100 min. The injection volume was 50 μL (injection flow rate of 0.2 mL/min). The focus flow rate and duration were optimized to 1.5 mL/min and 4 min, respectively, to achieve both good separation and high entrapped drug recovery as discussed in the Results.

Online detectors included an Agilent 1260 Infinity UV-Vis diode array detector (DAD) and fluorescence detector (FLD), as well as a Wyatt DAWN HELEOS II multi-angle light scattering (MALS) detector and Wyatt dynamic light scattering (DLS) (or quasi-elastic light scattering) detector. The DLS detector was located at the 140° scattering angle, and measurement duration was 5 s. The optimization of the detector setup and data analysis approach to quantify enrofloxacin release from the NPs are discussed in detail in the Results and the SI. Briefly, careful selection of the FLD and

UV wavelengths allows independent, selective quantification of the entrapped enrofloxacin and the overall polymer matrix of the NP, respectively. The UV DAD was set to monitor the 400 nm wavelength as the PLGA NP signal (UV_{NP}) without enrofloxacin interference, with full spectra collected from wavelengths 190 nm to 600 nm (step size 2 nm). The FLD was used to quantify the entrapped enrofloxacin at its optimal excitation and emission wavelengths of 280 nm and 420 nm, respectively (FLD_{drug}). Emission spectra were also collected at each time point at a fixed excitation wavelength (280 nm) with emission wavelength varying from 300 nm to 540 nm (5 nm step size), and the photomultiplier tube (PMT) gain was set to 13. The FLD_{drug}/UV_{NP} ratio represents the drug loading (i.e., ratio of enrofloxacin/polymer) in the NPs and can be used to quantify drug release over time.

3.2.7 HPLC Method for Analysis of Dissolved Enrofloxacin

Dissolved enrofloxacin was quantified on the Agilent 1290 Infinity HPLC system noted above, using a ZORBAX Eclipse Plus C18 HPLC column (4.6×150 mm dimensions, 5 µm particle size). Isocratic elution was performed with phosphate buffer (0.02 M, pH 3) (82%) and acetonitrile (18%) as the mobile phase,[231] flow rate of 1 mL/min, and run duration of 10 minutes. The injection volume was 10 µL. The UV DAD was set to monitor the 280 nm wavelength (UV_{drug}) and collect full spectra from 190 nm to 600 nm (step size 2 nm). Note while HPLC-FLD_{drug} data were also acquired, HPLC-UV_{drug} was used here for quantification of dissolved enrofloxacin because of the wider linear calibration range to measure high unentrapped drug concentrations in the drug loading measurements (Section 3.3.1).

3.3 Results and Discussion

3.3.1 Loading and Entrapment Efficiency of the PLGA-Enro NPs

Before initiating the AF4 analysis, the initial concentration of entrapped enrofloxacin in the unpurified PLGA-Enro NPs was estimated by subtracting the dissolved drug from the total drug concentration after removing the NPs by centrifugal ultrafiltration or centrifugation. While adsorptive loss of drug was observed to the ultrafiltration device in control samples of enrofloxacin without NPs (Figure B.4a), standard additions of known enrofloxacin concentrations to the NP samples (spiked prior to separation and sample processing) showed no significant loss of the spiked drug (Figure B.4b), suggesting excipients in the formulation can coat adsorptive sites on the ultrafiltration membrane to minimize drug losses.

These analyses found that a high proportion of the total drug from the synthesis ($\approx$ 94%) was unincorporated or rapidly desorbed. The low drug entrapment efficiency is consistent with the relatively low hydrophobicity of the enrofloxacin (log P of 0.24 to 1.1).[228] The drug loading, i.e., entrapped drug, was determined to be (2.0 ± 0.4) μg enrofloxacin/mg NPs or (1.2 ± 0.5) μg enrofloxacin/mg NPs ($n = 3$ replicates) by ultrafiltration or centrifugation, respectively, using the standard addition approach. We also applied a two-stage dialysis method (discussed in Section 3.3.5) to measure both the burst and entrapped drug concentrations, which yielded a drug loading of (1.9 ± 0.3) μg enrofloxacin/mg NPs, close to that obtained by ultrafiltration. The lower drug loading measured by centrifugation compared to the gentler ultrafiltration and dialysis methods may be attributable to strong centrifugal forces inducing additional release of

drug from the NPs.

3.3.2 Proof of Principle for Analysis of Drug Loading in PLGA-Enro NPs by Multi-detector AF4

AF4 method development includes optimization of the AF4 flow parameters and the detector settings on the UV, FLD, MALS, and DLS detectors used for characterization. For clarity, we first present the results of the optimized AF4 method, then discuss the detector and flow optimization in Section 3.3.3. Figure 3.2 shows the optimized AF4 chromatograms with UV, FLD, and LS detection for both PLGA-Enro and empty PLGA NPs, as well as the hydrodynamic radius (R_h) obtained by online DLS. Satisfactory size separation of the NPs was achieved, with elution of smaller NPs followed by larger NPs. The PLGA-Enro NPs showed complete elution with minimal loss to the membrane, discussed in Section 3.3.3. Although the empty PLGA NPs have a similar size distribution (with R_h directly measured by the online DLS detector), peak broadening and delayed elution were observed, suggesting NP interactions with the AF4 membrane and highlighting the need for online DLS analysis to obtain accurate size distributions.
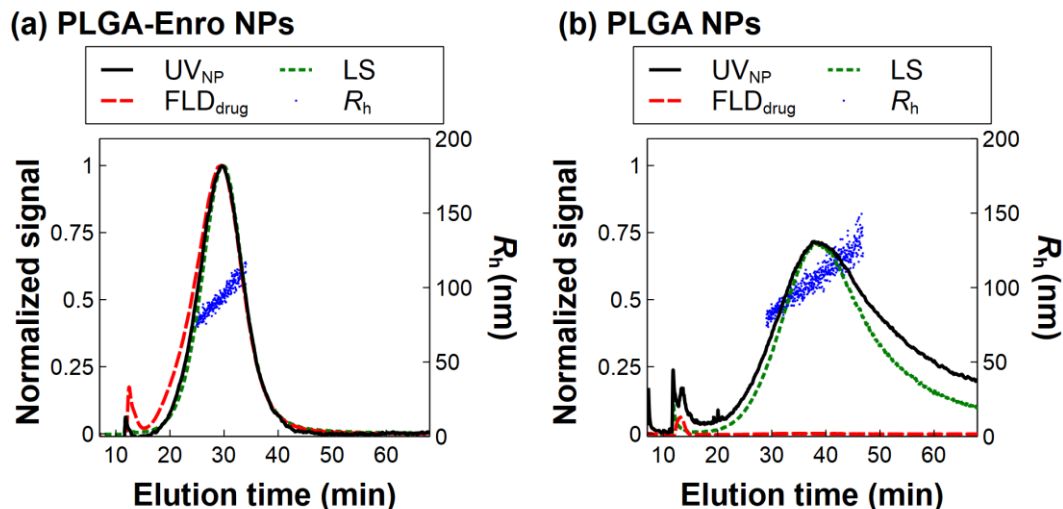
Figure 3.2. AF4 chromatograms with UV_{NP}, FLD_{drug}, and LS detection and simultaneous R_h analysis by online DLS for PLGA-Enro NPs (a) and "empty" PLGA NPs (b).

The key proposed advantages of AF4-FLD for drug loading analysis over alternative separation and detection schemes are (1) the rapid *in situ* removal of dissolved drug during the AF4 focus step, followed by (2) the selective and sensitive quantification of entrapped drug by FLD, with minimal interference from the polymer matrix. The successful separation of the NPs from unincorporated drug was confirmed by injecting a sample containing a physical mixture of empty PLGA NPs with enrofloxacin to the system (Figure B.5), no apparent difference in the FLD signal was observed in the mixture compared to the empty PLGA NPs. Furthermore, the FLD and UV-Vis spectra of the empty PLGA NPs, unpurified PLGA-Enro NPs (with $\approx 94\%$ free drug), and PLGA-Enro NPs purified *in situ* in the AF4 analysis were compared (Figure B.6). These spectra show that the high burst release of dissolved enrofloxacin is indeed eliminated in AF4, while only the NPs and entrapped drug are retained in the channel for analysis.

50

Regarding the selectivity and sensitivity issues, prior AF4 methods utilized UV-Vis detection for entrapped drug quantification.[59-62, 65] However, here the spectral analysis (Figure B.6a) shows that UV-Vis is not suitable to quantify enrofloxacin in the purified PLGA-Enro NPs because the peak absorbance attributable to the drug (at ≈ 280 nm) is very low relative to the NP scattering, which was further confirmed in the release experiments (Section 3.3.4). Therefore, subtraction corrections to eliminate NP scattering contributions from the drug absorbance are not feasible. However, we noted that because all NPs (PLGA-Enro and empty PLGA) show a UV signal attributable to the light scattering and absorbance by the PLGA, a judicious selection to monitor the UV signal at 400 nm (UV_{NP}) attributable only to the NPs (no enrofloxacin interference) can provide the PLGA NP concentration. On the other hand, setting the FLD excitation/emission wavelengths to those specific to the enrofloxacin (FLD_{drug}, excitation/emission at 280 nm/420 nm) enables a highly sensitive and selective detection of the entrapped drug with minimal contributions from the PLGA matrix (Figure 3.2 and Figures B.5 and B.6).

The selectivity of the FLD_{drug} signal for the entrapped enrofloxacin and UV_{NP} signal for the PLGA NPs is then exploited to achieve independent, distinct quantification of the entrapped drug versus the overall NPs, respectively. The ratio of the FLD_{drug} signal to the UV_{NP} signal for the NPs is then representative of the drug loading (mass of drug/mass of NPs). To obtain release profiles over time, we assume FLD_{drug}/UV_{NP} to be linearly proportional to the drug loading and evaluate the percent decrease relative to the FLD_{drug}/UV_{NP} measured at time zero (immediately upon dispersing the NPs in solvent). Normalizing FLD_{drug} to UV_{NP} also corrects for any

inconsistencies in NP concentrations across measurements, either because of changes to the sample (e.g., solvent evaporation or losses of NPs) or variability in recovery of NPs from the AF4 channel during the measurement. Hence, while the use of FLD to evaluate peptide binding to liposomes was previously reported to show poorer reproducibility and linearity than UV detection,[65] here we achieve a relative standard deviation of 6% on the raw FLD_{drug} peak areas and 3% on the ratio of FLD_{drug}/UV_{NP} peak areas ($n = 16$ replicates), whereas the UV detector (at any wavelength) is unsuitable to monitor changes in the entrapped enrofloxacin because of the low drug absorbance relative to NP scattering interference in the UV detection.

We also explored use of the raw FLD_{drug} signal to quantify the enrofloxacin inside the NPs against external calibration standards of dissolved enrofloxacin (injected into the AF4 without crossflow), but the entrapped drug showed a shift in the peak fluorescence emission wavelength relative to the dissolved drug, suggesting a strong interaction between the enrofloxacin and PLGA matrix (Figure B.6b). Evaluating the raw FLD_{drug} intensity against external (dissolved) standards also suggested a higher loading of (4.0 ± 0.1) µg/mg ($n = 16$ replicates) than that obtained in Section 3.3.1, suggesting fluorescence enhancement in the PLGA matrix. Because calibration against external standards was not possible, a separate measurement of entrapment efficiency is first required to determine the initial drug loading, and FLD_{drug}/UV_{NP} can subsequently be used to evaluate the relative proportion of drug loading remaining in the NPs.

3.3.3 Optimization of AF4 Flow Parameters for Optimal Separation and Drug Recovery

Optimization of the duration and flow rates of each step in the AF4 method typically revolves around achieving good size separation (by adjusting the focus flow rate or duration to focus the NPs into a narrow band against the accumulation wall and adjusting the crossflow rate in the elution step to achieve good resolution of different NP sizes) and good overall recovery with minimal perturbation of the NPs (for example, deformation of fragile NPs).[194] However, for entrapped drug quantification, the potential for drug washout from the NPs during the focus step must also be considered.[196, 232, 233] Here, three focus flow rates (0.5 mL/min, 1.5 mL/min, and 2.0 mL/min) and two focus durations (4 min and 8 min) were compared (Figure B.7 and Table B.2). The lowest focus flow rate (0.5 mL/min) showed a large initial "void" peak eluting immediately after the focus step, which likely represents incomplete NP relaxation in the AF4 channel and is unsuitable for the NP analysis. Comparing the 1.5 mL/min and 2.0 mL/min focus flow rates, higher focus flow rates resulted in both lower NP recovery (evaluated from the UV_{NP} peak area). Furthermore, higher flow rates and longer focus durations may induce drug washout (evaluated from the FLD_{drug}/UV_{NP} ratio, representing drug loading). Hence, a moderate focus flowrate (1.5 mL/min) and shorter focus duration (4 min) were selected as the optimal conditions.

In the optimized conditions, we achieved a NP recovery of 90% ± 6% ($n = 16$ replicates), as determined by comparing the UV_{NP} peak area in the main peak (eluting from ≈ 13 min to 60 min) to that for a NP injection without any applied focus or cross flow. Although the FLD spectra show that the small void peak contains some

enrofloxacin, it is excluded from further analysis since the identity of this peak (excess polymer or NPs) is not clear; however, including this peak did not significantly change the conclusions of the analyses (data not shown). A rinse peak associated with the final rinse through the injection port at the end of each measurement (Figure B.7), representing NPs adsorbed in the system (e.g., the injection tubing), is also excluded from analysis. We note that some entrapped drugs may still be washed out from the NPs in the optimized AF4 method, but we assume the fraction of washout is consistent across all measurements (with consistent AF4 settings) and hence that the semi-quantitative analysis of drug loading relative to the time zero measurement is valid.

3.3.4 AF4 Measurements Show Temperature-dependent Release Profiles

The optimized AF4 method was applied to acquire direct release profiles on the PLGA-Enro NPs and compared to a conventional, indirect approach (dialysis with quantification of drug release to the dialysate). Temperature is well known to influence drug release rates from polymeric NPs; notably, an increase in temperature above T_g results in the transition from a glassy to rubbery state, and faster release is expected with the increased relaxation of the polymer chains [192]. The measured T_g of the PLGA-Enro NPs was 32.9 ± 0.8 °C ($n = 3$ replicates on independently synthesized NPs), with an onset point of (28.5 ± 0.3) °C and offset point of (37.67 ± 0.09) °C (Figure B.3). Hence, temperatures below (20 °C), near (30 °C), and above (37 °C) the T_g were applied to evaluate the capability of the AF4 and dialysis approaches to capture the expected temperature-dependent release behavior.

Figure 3.3 presents the AF4-UV$_{NP}$ and AF4-FLD$_{drug}$ chromatograms, as well as

the FLD_{drug}/UV_{NP} ratio normalized to the initial FLD_{drug}/UV_{NP} at each individual elution time point, representing the fraction of entrapped enrofloxacin remaining *in each size fraction of NPs*. The unique applications of this size-specific loading data, together with the DLS and MALS data, are discussed in Section 3.3.6. Spectral analysis of the NPs over the duration of the release again demonstrated that the FLD detector is critical to quantify the drug loading, as the UV absorbance of the drug is very small relative to the NP scattering signal (Figure B.8).
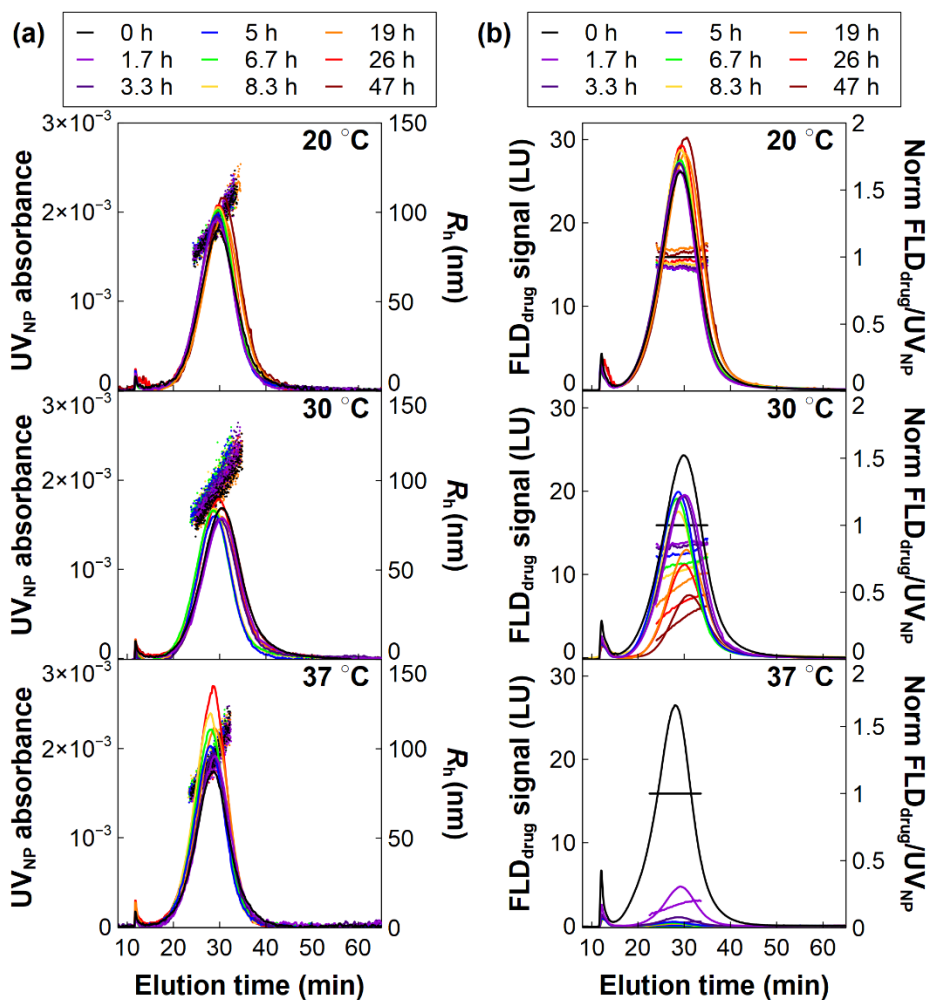
Figure 3.3. AF4-UV_{NP} (a, solid traces, left axis) and AF4-FLD_{drug} (b, solid traces, left axis) chromatograms, R_h (a, scatter points, right axis), and normalized FLD_{drug}/UV_{NP} ratios (b, scatter points, right axis) of PLGA-Enro NPs.

Here, the overall drug release is assessed by integrating FLD_{drug} and UV_{NP} peak areas across the entire NP sample (elution time 13 min to 60 min), taking the ratio of FLD_{drug}/UV_{NP} peak areas as the drug loading, and dividing by the peak area ratio for the initial sample (0 h release), to obtain the fraction of *entrapped* drug remaining over time (Figure B.9a). Given the initial amounts of entrapped and free drug (Section 3.3.1), the percent release relative to the *total* drug in the system was then computed (Figure 3.4a). The AF4 measurements clearly show a strong temperature dependence of enrofloxacin release from the PLGA NPs, with minimal enrofloxacin release at 20 °C, slow release at 30 °C (near T_g), and rapid release at 37 °C (above T_g). Fitting the release profiles to first-order kinetics gives apparent rate constants, $k_{apparent,AF4}$, of (0.0010 ± 0.0005) h^{-1}, (0.06 ± 0.01) h^{-1}, and (1.0 ± 0.1) h^{-1} ($n = 3$) at 20 °C, 30 °C, and 37 °C, respectively (model fits shown in Figure 3.4a and Figure B.9a).

It is noted that the UV_{NP} peak area increased over time at 37 °C (Figure 3.3a), likely due to solvent evaporation from the 1 mL dialysis device leading to concentration of the NPs over time. Hence, the FLD_{drug}/UV_{NP} normalization is important to correct for NP concentration and appropriately compare enrofloxacin loading in the NPs across multiple samples. We also note the same trends are clearly observed for the raw FLD_{drug} peak over time (Figure 3.3b) as in the FLD_{drug}/UV_{NP} peak area (Figure B.9a), supporting the reliability of the analysis (i.e., the decreasing FLD_{drug}/UV_{NP} ratio is not an artifact of changing UV_{NP} peak areas).
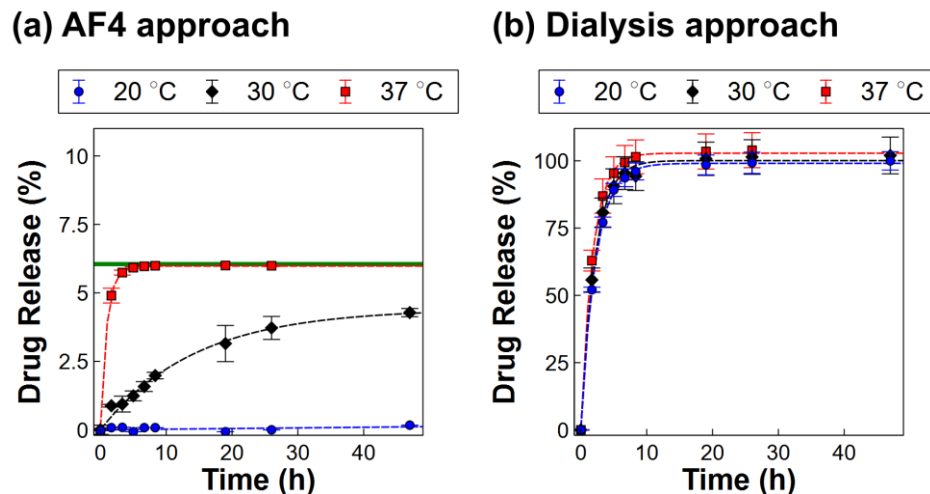
Figure 3.4. Release profiles of PLGA-Enro NPs by multi-detector AF4 (a) and dialysis (b).

3.3.5 Conventional Dialysis Measurements are Poorly Sensitive to the Release of Entrapped Drugs in the Presence of a High Burst Release or Rapid Release

The AF4-FLD approach was compared to dialysis as a conventional method to acquire release profiles, in which the concentration of drugs in the dialysate at each time point was measured by HPLC (Figure B.9b). The overall release profiles obtained by dialysis appear to contradict the AF4 measurements. For example, AF4 showed a rapid release of enrofloxacin at 37 °C within < 4 h (Figures 3.3 and Figure 3.4a), whereas dialysis suggests a slower release over 10 h, similar to that at the lower temperatures (Figure 3.4b). At 20 °C, AF4 showed no significant release of the entrapped drugs, whereas dialysis results appear to indicate a similar extent of release to the higher temperatures. Fitting the dialysis release profiles to first-order kinetics gives apparent rate constants, $k_{apparent,dialysis}$, of (0.45 ± 0.01) h^{-1}, (0.48 ± 0.06) h^{-1}, and (0.55 ± 0.02) h^{-1} ($n = 3$) at 20 °C, 30 °C, and 37 °C, respectively (model fits shown in Figure 3.4b). Overall, the dialysis results would suggest minimal differences in either the rates or

extent of release, regardless of temperature. In contrast, AF4 clearly distinguishes the expected temperature dependence in both the rate and extent of drug release from the NPs.

These seemingly inconsistent results can be attributed to the difference in the principle of each method and the presence of a high proportion of burst release of unincorporated or loosely bound drugs ($\approx 94\%$ of the total enrofloxacin) in the PLGA-Enro NPs, which can obscure quantification of the entrapped drug. The dialysate includes the total dissolved enrofloxacin (from both the burst release and subsequent release of entrapped drugs). Hence, distinguishing the release of specifically the entrapped drugs by dialysis is challenging whenever a burst release occurs. Furthermore, the dialysis membrane introduces a lag time to equilibrate the dissolved drug inside and outside the dialysis device. Hence, obtaining an accurate release rate of the entrapped drugs via dialysate measurements would require both a low background of burst release drug and a slow release rate from the NPs relative to the dialysis kinetics.

Three different approaches were taken to test these hypotheses: (1) a "two-stage" dialysis experiment to confirm the burst amount and the amount of entrapped drug release; (2) theoretical modeling to affirm the proposed roles of diffusion of entrapped drug from the NPs versus diffusion of the burst drug through the dialysis bag; and (3) a release experiment using purified PLGA-Enro NPs to validate the AF4 measurements against dialysis in a low burst, slow release scenario.

Approach 1 (Two-Stage Dialysis) If the AF4 results for the entrapped drug release extent are valid, there should be a difference in the enrofloxacin concentrations appearing in the dialysate after equilibration at 37 °C and 20 °C, representing the release

of total drug (entrapped + burst) and unincorporated drug (burst), respectively. Direct subtraction of the dialysate measurements in Figure 3.4b yields an entrapped drug concentration of (1.2 ± 2.3) µg enrofloxacin/mg NPs ($n = 3$ replicates). The high relative standard deviation is attributable to the low entrapment, together with the propagation of uncertainty in the two concentrations being subtracted. To validate the AF4 results while minimizing these errors, an additional dialysis experiment was designed in two stages; first, the NPs were dialyzed at 20 °C for 26 h to measure the burst release (assuming negligible release from the NPs); then, the dialysis device was transferred to a reservoir with clean PBS media at 37 °C for another 26 h to measure the subsequent release of the entrapped drug without interference of the burst release. Following this method, the burst release was determined to be (29 ± 1) µg enrofloxacin/mg NPs and drug entrapment was (1.9 ± 0.3) µg enrofloxacin /mg NPs (i.e., entrapment efficiency of $6.0\% \pm 1.0\%$) ($n = 6$, duplicate experiments on three NP batches), consistent with that determined by ultrafiltration in Section 3.3.1.

Approach 2 (Diffusion Model) If the AF4 measures the entrapped drug release while dialysis measures both the burst and entrapped drug release, we expected these results could be reconciled through a diffusion model that explicitly accounts for the two distinct diffusion rates from the polymeric NPs (k_p) and across the dialysis membrane (k_d), while tracking the entrapped drug in the NPs, the dissolved drug in the dialysate, and the dissolved drug inside the dialysis bag. The model diagram, equations, implementation details, and results are presented in the Appendix B (Figure B.10 and Equations B.2 to B.6). In brief, the diffusion model is derived from Fick's first law assuming homogeneous drug concentrations within each compartment (as previously

presented for drug diffusion from liposomal carriers and across a dialysis membrane;[234-236]) here, the model is adjusted from prior references to account for accumulation of drug in the dialysis reservoir (i.e., perfect sink conditions are not assumed). The k_d value at each temperature was measured in independent dialysis experiments to minimize the number of fitting parameters and hence uncertainty in the model fits, with k_p as the only fitted parameter. Comparison of measured k_d values for dissolved enrofloxacin alone or spiked into suspensions of empty PLGA NPs (Figures 3.5 and B.11) showed the nanoformulation excipients slowed the dialysis rate; hence, the spiked release rates were used in the models for the PLGA-Enro NPs.
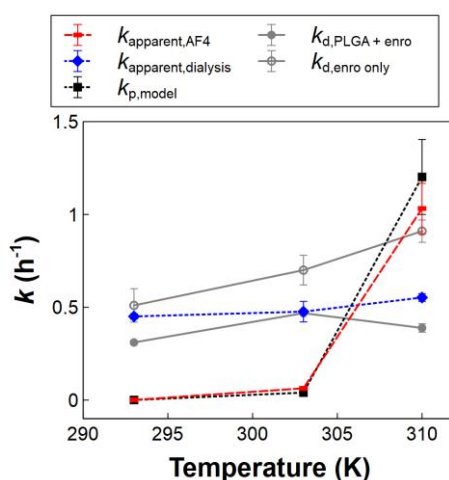
Figure 3.5. Rate constants for drug diffusion from PLGA NPs fitted from the diffusion model ($k_{p,model}$), and "apparent" rate constants from AF4 alone or dialysis alone, considering only one single release process (Figure 3.4).

The model was successfully able to fit the experimental data (Figure B.12), supporting the proposed explanation for the differences in the AF4 and traditional dialysis measurements. The results for the fitted k_p are summarized in Figure 3.5 and Table B.3 and compared to the "apparent" rate constants ($k_{apparent}$) fitted to the AF4 and dialysis data, assuming only one single release process (Figure 3.4). At all temperatures,

$k_{apparent,dialysis}$ is primarily influenced by the large burst release and reflects the release rate of the dissolved drug through the dialysis bag (k_d), whereas $k_{apparent,AF4}$ reflects the release rate of the entrapped drug from the NPs (k_p). The diffusion lag imparted by dialysis can also be important at 37 °C, where the dialysis rate of enrofloxacin in the presence of the NPs ($k_d = (0.39 \pm 0.02)$ h^{-1}) is slower than the NP release rate ($k_p = (1.2 \pm 0.2)$ h^{-1}); hence, dialysis becomes the limiting rate for drug appearance in the dialysate.

The trend in rate constants with temperature also supports the proposed physical explanations for k_d versus k_p, according to the Stokes-Einstein law, the drug diffusion coefficient should be linearly related to temperature, assuming no change in other factors such as viscosity. Indeed, $k_{apaprent,dialysis}$ and k_d across the dialysis membrane show a relatively linear relationship with temperature. On the other hand, $k_{apaprent,AF4}$ and k_p for release from the NPs show a sharp increase above T_g, indicating that the rapid release is not attributable purely to increasing thermal energy but rather to the glassy to rubbery transition of the polymeric matrix above T_g.

Approach 3 (Purified PLGA-Enro NP Release) To more definitively validate the AF4 results and the hypothesized influence of the burst release, we also conducted release experiments with purified PLGA-Enro NPs, where much of the dissolved drug is removed, and at 30 °C, where the release of entrapped drug is expected to be slower than that through the dialysis bag (Figure 3.5). To purify the NPs, 1 mL of PLGA-Enro NPs (7.5 g/L NPs) were dialyzed against 120 mL of PBS at room temperature for 26 h without buffer change to remove unentrapped drug. The remaining concentration of dissolved drug is calculated to be 11% of the total remaining drug (entrapped + dissolved) in the dialysis bag, based on the entrapment efficiency and dilution factor in

the dialysis reservoir. Then, the dialysis device was transferred to a preheated PBS reservoir at 30 °C, and samples were collected and analyzed following the same procedure as release experiments for unpurified NPs.

The equilibrium extent of release determined by dialysis and AF4 was 94% and 80%, respectively, of the calculated total drug (entrapped + dissolved) in the purified NPs (Figure 3.6), consistent with the expected 11% dissolved drug remaining after purification. Furthermore, fitted release rate constants were more similar on the purified NPs ($k_{apparent,AF4} = 0.09 \pm 0.01$ h^{-1} and $k_{apparent,dialysis} = 0.19 \pm 0.02$ h^{-1}) than the unpurified NPs (0.06 ± 0.01 h^{-1} by AF4 and 0.48 ± 0.06 h^{-1} by dialysis), with the rate measured in the dialysate still somewhat higher due to the contribution of the remaining 11% free drug in the purified NPs. Overall, these results are consistent with our justification that the higher extent and rate of release measured in the dialysate at 30 °C is attributable to the burst release obscuring the quantification of the entrapped drug.
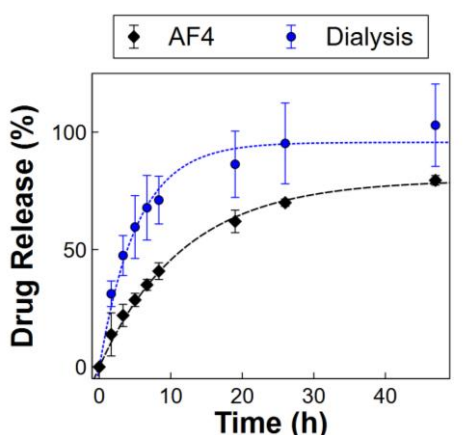
Figure 3.6. Drug release profile obtained by AF4-FLD and dialysis for the purified PLGA-Enro NPs, obtained following the same procedure as Figure 3.4. The raw AF4 chromatograms are presented in Figure B.13.

In summary, measurements of drug in the dialysate are strongly influenced by

the presence of any burst release, which are often unavoidable in nanoformulations.[193] AF4-FLD resolves this issue by (1) providing rapid separation of the NPs from the dissolved background and (2) enabling direct, real-time characterization of the enrofloxacin entrapped in the NPs, thereby eliminating the interference of dissolved drugs in the measurement as well as the dialysis lag time. Hence, both the extent and rate of release of entrapped drugs are selectively probed, without requiring additional control experiments on dissolved drug release or modeling analyses that would be needed to correctly interpret the conventional dialysis results.

3.3.6 AF4-FLD-LS Measurements Yield Size and Shape Data and Size-dependent Release Profiles for Mechanistic Interpretation of Release Results

Coupling AF4 with online DLS and MALS detectors produces additional useful information regarding the size and shape of the NPs. The online DLS results showed no significant change in the R_h of the NPs, consistent with batch DLS measurements (Figure B.14a). Additionally, using the MALS detector to obtain the radius of gyration (R_g), the shape factor R_g/R_h was determined to be 0.76 ± 0.03 at time zero ($n = 9$ replicates), suggesting a homogenous sphere shape for the NPs,[237] and also did not vary significantly over time (Figure B.14b). We also did not observe any significant changes in the zeta potential (Figure B.15). Overall, the direct size analysis by online DLS and MALS shows that the PLGA-Enro NPs were physically stable during the drug release, and hence changes in swelling or degradation of the polymeric NPs are not involved in the higher release with temperature.

The combined simultaneous collection of FLD_{drug}, UV_{NP}, and DLS data across

63

the entire continuous size distribution of NPs eluting from the AF4 channel enabled size-resolved drug release profiles to be evaluated with remarkable resolution by evaluating the FLD_{drug}/UV_{NP} ratio at each individual chromatographic time point (Figure 3.3b). For example, an elution time of 21 min corresponded to $R_h = 65$ nm, and the relative fraction of entrapped enrofloxacin remaining in this specific size fraction of NPs over the release experiment can then be monitored as the FLD_{drug}/UV_{NP} signal eluting at 21 min, distinctly from the release from other size fractions of the NPs (Figure 3.7a). Release rate constants were thereby fitted at every chromatographic time point (representing different size NPs) to obtain individual release rates at high size resolution (Figure B.16). A more rapid decrease in the FLD_{drug}/UV_{NP} ratio is clearly observed for smaller NPs (eluting earlier) than for larger NPs. Furthermore, the relationship between the release rate constant and NP size, $k \propto 1/R_h^2$ (Figure 3.7b) is consistent with that predicted across the given NP size range by radial diffusion models that explicitly account for spatial variation in the drug concentration during the release.[238, 239] Obtaining these size dependent release profiles would typically require tedious labor to synthesize different NPs with different average R_h or separate a polydisperse NP sample into size fractions, then perform separate release experiments on each sample. Hence, a limited set of data are typically available to test models for the size dependence of the release rate. These results demonstrate that AF4-FLD can be an extremely powerful tool to distinguish drug release from polydisperse NPs or several different NP populations within one single release experiment, providing detailed information to achieve a better understanding of the release mechanism.
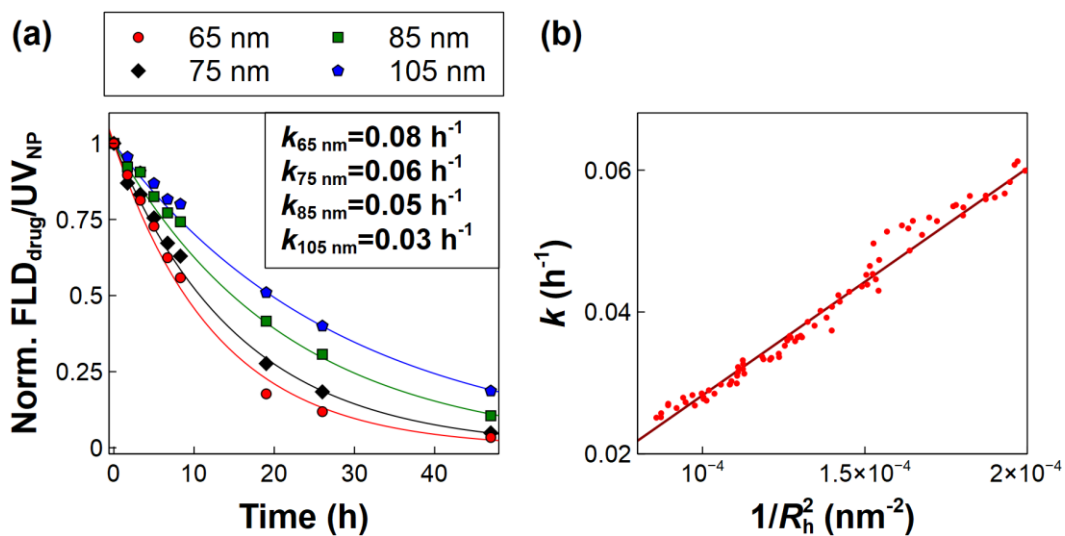
Figure 3.7. Size-dependent release rates were analyzed across the AF4 chromatograms for the PLGA-Enro NPs at 30 °C (Figure 3.3). Fitted release rate constants were evaluated for all chromatographic time points from 21 to 30 min.

3.4 Conclusion

This research demonstrates AF4-FLD as a novel approach that successfully overcomes limitations of traditional dialysis methods (notably, lag time and susceptibility to interferences from the burst release background) to obtain overall release profiles of enrofloxacin from PLGA NPs with minimal sample preparation, while also enabling fully size-resolved release profiles to be simultaneously acquired. A complete AF4-FLD method development was provided that explicitly addresses the optimization of the focus step to balance drug recovery and separation efficiency. The AF4-FLD approach showed highly promising results over traditional dialysis methods to reliably distinguish the extent and rate of the entrapped drug release, particularly under circumstances with any background of burst release drug. The direct entrapped drug measurement was crucial here to identify the influence of NP transformations (i.e., crossing T_g) on the drug release rate. Furthermore, considering that NPs in real

applications will not be applied in a dialysis device and that the entrapped drug concentration can be more important in targeted delivery than the burst release (which may occur far from the ultimate delivery site), the direct measurement of the entrapped drug release by AF4 is purported to be more useful than dissolved drug analysis by dialysis. Additional advantages of AF4 demonstrated here include the capability to add online DLS and MALS detection to simultaneously monitor the stability of the NPs during the drug release, and the ability to distinguish release rates from different NP size populations, providing critical data to deduce the release mechanisms.

The AF4-FLD method is expected to be broadly applicable to characterize the release of fluorescent or fluorescently-tagged drugs from polymeric NPs and other "soft" NPs, with fluorescent drugs representing the vast majority of drugs that are currently FDA-approved for nanomedicines (e.g., liposomal and albumin-based drugs). The method is expected to be facile and robust to characterize drug release and NP stability while eliminating errors in release measurements due to drug interactions with devices used in typical release experiments (e.g., the dialysis membrane). In future studies, we will validate this method for different fluorescent dyes and will also explore the unique capabilities of AF4 to separate NPs from other constituents (e.g., biomolecules) in order to acquire release profiles and drug distributions in complex matrices. These measurements can lead to better design of drug-loaded NPs and yield high value in reducing time and costs to characterize nanodelivery systems before initiating *in vivo* experiments.

CHAPTER 4. SIZE-DEPENDENT ANALYSIS TO DISTINGUISH MECHANISMS OF RELEASE FROM POLYMERIC NANOPARTICLES

4.1 Introduction

Polymeric nanoparticles (NPs) and other nanomaterials such as liposomes or micelles have versatile applications in biomedicine and broader fields as carriers for drugs or other active ingredients. Along with size distribution and surface chemistry, the release profile is a critical parameter to control, as a slow or triggered release is often essential to ensure the nanoparticle carries and releases the active ingredient at the desired rate or under desired conditions. The release mechanism is fundamentally determined by the localization of the drug (e.g., entrapped, encapsulated, or surface-bound) and the properties and transformations of the particle (e.g., particle structure, glassy or rubbery state, shrinking or swelling, degradation or erosion). Hence, to predict drug release or transfer from the NPs, it is critical to understand the drug localization and identify the primary release mechanisms. Direct measurement of the nanoscale drug localization in polymeric NPs is often highly challenging, with state-of-the-art methods only recently being developed and demonstrated, such as coupled atomic force microscopy – infrared spectroscopy (AFM-IR or "nanoIR").[240] Hence, release assays are typically conducted to attempt to deduce the release mechanism.

In a standard drug release study, release is evaluated either as the total drug concentration appearing in solution (i.e., the released drug) over time, or the total drug depleted from the NPs over time; that is, the drug is quantified in bulk. A number of

release models, including dissolution models, radial diffusion models, and the Korsmeyer-Peppas model, are commonly applied to fit time-resolved release profiles to deduce the release mechanism. However, such release profiles may not contain sufficient information to confidently deduce the initial drug distribution or the release mechanism, given that several models can produce similar time-resolved release profiles despite being derived using completely different assumptions and conceptual model formulations. In principle, introducing size as a second dimension to the release profile would enable a more definitive distinction of release mechanisms by imposing additional constraints. For example, radial diffusion models predict a strong influence of particle size on the release rate, which could be tested given size-resolved experimental release data. However, measuring size-resolved release rates is challenging in practice when standard release assays only separate dissolved drugs from bulk NPs. Hence, acquiring release profiles on different sizes of NPs would require tedious labor to synthesize batches of NPs with different sizes or separate a polydisperse sample of NPs into discrete size fractions, then conduct a separate release study on each batch of NPs.[238] The size resolution achievable is then severely limited by the number of size fractions that can be prepared.

Our recent research presented the development of multi-detector asymmetric flow field-flow fractionation (AF4) to rapidly acquire size-resolved release profiles at high size resolution. Prior applications of AF4 to evaluate drug release or transfer have been limited to bulk analysis across the entire NP peak,[59, 61, 62, 66, 241, 242] or performed size-resolved evaluations via fraction collection and offline analysis of each fraction.[57, 243] Our study demonstrated the ability to achieve release profiles at high size resolution

by taking full advantage of the continuous size separation provided by AF4, together with online fluorescence detection (FLD), UV detection, and dynamic light scattering (DLS) to evaluate drug loading, NP concentrations, and NP sizes at every chromatographic time point across the size distribution. When applied to poly (lactic-*co*-glycolic) acid (PLGA) NPs loaded with enrofloxacin, a relatively hydrophilic antibiotic (octanol-water partitioning coefficient, log P, of 0.24 to 1.1[228]), the method revealed size-dependent release rates consistent with that predicted by a radial diffusion model. Further advantages included *in situ* removal of an immediate burst release of the hydrophilic enrofloxacin, which produced a strong interference in release evaluation by dialysis.

This study further develops the multi-detector AF4 method to evaluate the product purity, transformations, and release mechanisms of PLGA NP formulations with the introduction of online total organic carbon (TOC) detection for polymer quantification (Figure 4.1a). A robust method to quantify the PLGA NPs is particularly critical to evaluate drug loading (i.e., the mass/mass concentration of drug to polymer). UV-vis detection can be poorly suited to obtain mass concentrations as the measured transmittance is influenced severely by light scattering,[244] which is not proportional to mass concentration across a NP size distribution or if the NP size changes over time (e.g., because of shrinking, swelling, or degradation). Refractive index (RI) is sensitive to changes in pressure (and hence flow rates) during the AF4 measurement, as well as the compression or density of the polymer,[245] resulting in uncertainty or variability in the RI increment (dn/dc) to relate RI to concentration. Here, TOC analysis is proposed to provide more universal detection and unambiguous, mass-based quantification of

polymer concentrations, both in the NP population as well as dissolved polymer (i.e., excess surfactant).

The extended AF4 method is applied to PLGA NPs loaded with coumarin 6 (C6), a lipophilic fluorescent dye (log P) of 5.6.[246] As with other lipophilic dyes,[247-251] C6 has been used as a model representation of lipophilic drugs to better understand their release behavior, or alternatively as a fluorescent tag to track NP distributions in biological samples (where the dye ideally remains within the particles).[252] Prior literature on the synthesis and release behavior of C6-loaded PLGA NPs show a wide range of extents and rates of C6 release, as summarized in the Appendix C, Table C.1. Notably, these studies report the possibility for both a slow "burst" release of the lipophilic C6 from the NP surface, slower release of entrapped C6 via degradation of the PLGA NPs, and enhanced rates and extents of transfer when the NPs are exposed to liposomes. An understanding of C6 distribution in the NP hence may be important to predict the release or transfer behavior. Here, the size-resolved AF4 analysis is proposed to provide evidence of the release mechanisms of C6 from PLGA NPs.

In summary, the main objectives of this study are to develop the novel coupling of AF4 with online TOC detection to quantify polymeric NP concentrations and evaluate product purity, and to apply the AF4 method to evaluate the size-resolved release of C6 from PLGA NPs. Bulk release profiles are validated against liquid chromatography LC) analysis to quantify C6 extracted from the NPs (Figure 4.1b), and AF4 analyses of the overall PLGA NP size and concentration are complemented with LC – quadrupole time-of-flight (QTOF) analysis of small polymer residues identified in the NP extracts (Figure 4.1b). Finally, the size-resolved release profiles acquired by

70

AF4 for the C6-loaded PLGA NPs are contrasted to that previously acquired on enrofloxacin-loaded PLGA NPs to distinguish release mechanisms and deduce differences in drug distribution in the NPs.
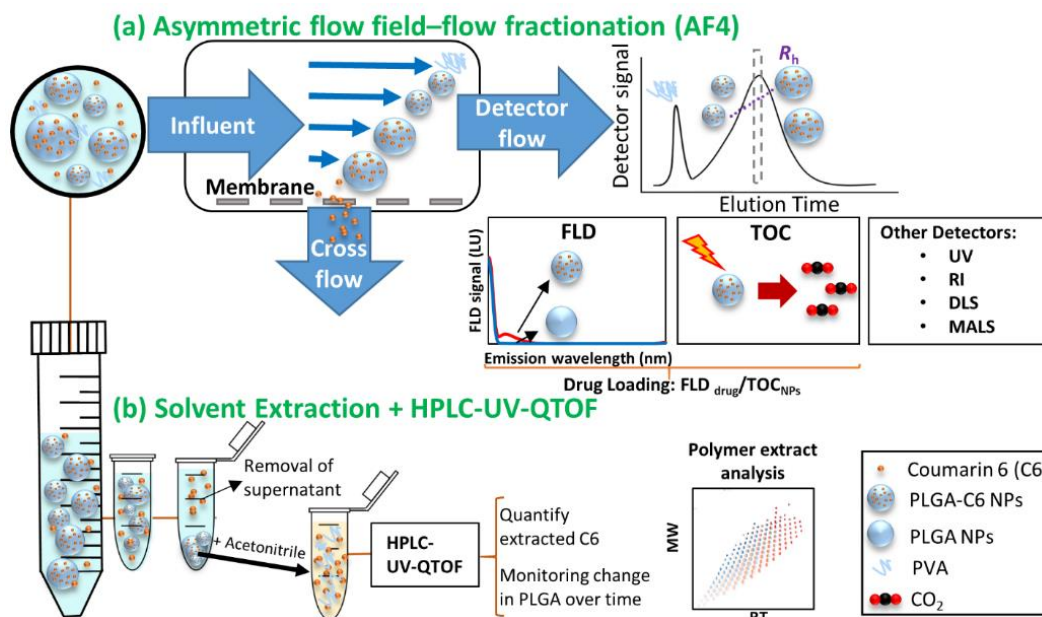
Figure 4.1. Schematic of the experimental approaches to investigate the drug release behavior by using AF4 (a) or organic solvent extraction and LC-QTOF.

4.2 Materials

For the NP synthesis, 3-(2-Benzothiazolyl)-7-(diethylamino)coumarin (coumarin 6, laser grade, 98%) and poly (vinyl alcohol) surfactant (PVA, 88% hydrolyzed, molecular weight (MW) of 85–120 kDa) were purchased from Acros Organics (Morris Plains, NJ, USA). Poly(lactic-*co*-glycolic acid) (PLGA, 50:50 lactide: glycolide, MW of 38–54 kDa), and dichloromethane (DCM) (anhydrous, ≥99.8%, contains 40-150 ppm amylene as a stabilizer) were purchased from Sigma Aldrich (Millipore Sigma, St Louis, MO, USA). For the release experiments, potassium phosphate monobasic anhydrous (KH_2PO_4, ACS grade, Amresco, Solon, OH, USA),

sodium phosphate dibasic heptahydrate ($Na_2HPO_4 \cdot 7H_2O$, ACS grade, Amresco), sodium chloride (> 99.0%, ACS grade, Sigma Aldrich), and potassium chloride (99.999%, trace metal basis, Acros Organics) were used for the preparation of phosphate buffered saline (PBS, 137 mM NaCl, 2.7 mM KCl, 10.1 mM Na_2HPO_4, 1.8 mM KH_2PO_4, pH 7.4). For AF4 mobile phase preparation, KH_2PO_4, $Na_2HPO_4 \cdot 7H_2O$, and sodium sulfate decahydrate ($Na_2SO_4 \cdot 10H_2O$, Acros Organics) were used for the mobile phase preparation. LC-MS grade acetonitrile ($\geq$ 99.9%, OmniSolv LC-MS, EMD Millipore, Burlington, MA, USA and $\geq$ 99.9%, Baker Analyzed for LC-MS, J.T. Baker, Phillipsburg, NJ) and LC-MS grade water (Baker Analyzed for LC-MS, J.T. Baker, Phillipsburg, NJ), as well as formic acid (ACS reagent, Honeywell, Charlotte, NC, USA) were used for LC-QTOF mobile phase preparation.

4.3 Methods

4.3.1 Synthesis of Polymeric Nanoparticles

Coumarin 6 loaded PLGA NPs (PLGA-C6) were synthesized with some modifications to a previously reported emulsion evaporation technique.[253] To prepare the aqueous phase, PVA was initially dissolved at 1.5 % (w/w) in deionized water (DIW) under constant magnetic stirring (600 rpm) with heating at 90 °C for $\approx$ 3 hours. The solution was filtered through a 0.22 μm polyethersulfone (PES) membrane (EMD Millipore) to remove undissolved or aggregated PVA, then diluted to a final concentration of 0.3 % (w/w) in DIW. A stock solution of C6 was prepared by dissolving 4 mg of C6 powder in 4 mL of DCM, then diluted 20 times in DCM to a final concentration of 0.05 g/L. The organic phase for the NP synthesis was then prepared by

dissolving 12.5 mg of PLGA powder in 1 mL of DCM, followed by adding 0.25 mL of C6 solution (0.05 g/L in DCM). The organic phase was slowly added to 12.5 mL of PVA solution (0.3 % (w/w)) under constant stirring (660 rpm), followed by 10 minutes of probe sonication at an amplitude of 100 % and pulse of 2 s on / 2 s off (Fisherbrand Model 120 Sonic Dismembrator, Fisher Scientific, Waltham, MA, USA), then stirred for another 4 hours to evaporate the remaining DCM under a fume hood. The total concentrations of material in the remaining aqueous phase are 1 mg/L of C6, 1 g/L of PLGA, and 3 g/L of PVA.

To purify the NPs, 8 mL of the synthesized NPs suspensions were distributed among eight Eppendorf Protein LoBind centrifuge tubes and centrifuged at 13000 rpm (12641g) for 23 min (MiniSpinPlus, Eppendorf, Hamburg, Germany), followed by two washes with DIW. The supernatants from each centrifugation step were collected and held refrigerated and in the dark for further quantification of the C6 and PVA by LC-QTOF and batch TOC analysis, respectively. Separate batches were prepared for each release experiment; hence, error bars in all analyses include batch-to-batch variability along with variability in the experiments and measurements.

4.3.2 Characterization of Synthesized Particles

4.3.2.1. Batch DLS and zeta potential measurements

Batch hydrodynamic size and zeta potential were measured by DLS and electrophoretic light scattering, respectively, on a Malvern Zetasizer Nano ZS instrument (Malvern Panalytical Inc., Malvern, UK). Measurements were taken on the unpurified NPs (before washing) and purified NPs at the beginning and end of the

release experiments (i.e., 0 h and 96 h). DLS measurements were taken on the sample as collected (0.25 g/L of NPs in PBS). For zeta potential measurements, the NPs were centrifuged and resuspended in DIW to avoid rapid corrosion of the electrodes on the folded zeta capillary cell (DTS 1070, Malvern) used for the measurement. The applied voltage was set to 100 V, and the Smoluchowski model was applied to convert electrophoretic mobility to the apparent zeta potential. Reported values are the average and standard deviation from four independently synthesized batches of NPs with five measurements per sample.

4.3.2.2. Transmission electron microscopy (TEM) imaging

Transmission electron microscope (TEM) images of PLGA-C6 were obtained by a JEOL JEM-1400 series 120kV (JEOL USA Inc., Peabody, MA, USA). The NPs were mixed with a contrast agent (uranyl acetate) before placing one droplet over a carbon copper grid. The sample was dry before placing in the microscope chamber (Appendix C, Figure C.1).

4.3.2.3. Differential scanning calorimetry (DSC)

A portion of the NPs was lyophilized for DSC analysis by adding trehalose dihydrate (Sigma Aldrich) as a cryoprotectant to the purified PLGA-C6 NP suspension in a ratio of 1 g trehalose dehydrate to 1 g PLGA NPs, then lyophilizing on a Freezone 4.5 L benchtop freeze drier at -84 °C (Labconco, Kansas City, MO, USA).

The glass transition temperature (T_g) of the NPs was measured by modulated differential scanning calorimetry (MDSC) The measurements were obtained on a TA Instruments DSC (model Q200, TA Instruments, New Castle, DE, USA). The DSC experiments were performed with 5 to 10 mg of sample using standard aluminum pans.

The sample compartment was purged with nitrogen (gas flow 50 mL/min) during the experiment. The procedure was as follows: (1) cool down sample to -40 °C; hold isothermal at this temperature for 5 min; (2) modulate +/- 0.80 °C every 60 seconds; (3) isothermal for 5.00 min (4) Ramp 5.00 °C/min to 80.00 °C. The T_g and onset and offset points were calculated using the inflection 188 point method using the Reverse Heat Flow Signal. (Appendix C, Figure C.2).

4.3.2.4. Quantification of dye loading and entrapment efficiency

To evaluate the dye loading and entrapment efficiency, the dissolved (unentrapped) C6 from the synthesis was measured in the aqueous supernatants collected during the NP purification procedure. The entrapped C6 was also measured on the first NP sample collected in the release experiments (0.25 g/L NPs, time 0) after centrifugation to pellet the NPs and remove supernatant, followed by extraction of the pellet into acetonitrile, as described in Section 4.3.4. All samples were diluted by a factor of two to achieve a background solution of 50 vol % acetonitrile / 50 vol % DIW for measurement by LC-UV-QTOF with C6 quantification against external standards in the same background solution, as described in Section 4.3.6. The mass of C6 measured in the extracted NPs was divided by the mass of PLGA NPs to compute the C6 loading (µg C6/mg NPs). The entrapment efficiency is also reported as the ratio of the entrapped C6 to the total measured amount of C6 (sum of the entrapped C6 and supernatants from the NP purification steps).

4.3.3 Batch TOC Analysis for Quantification of PLGA NPs and PVA Surfactant

Batch TOC measurements of the polymeric materials were conducted using a portable TOC detector (Sievers M9-SEC Portable TOC Analyzer, Suez, Trevose, PA, USA) configured in batch analysis mode. Acid (6 M phosphoric acid) and oxidizer (15% ammonium persulfate) cartridges were obtained from Suez (Trevose, PA, USA), and flow rates were set to 2 µL/min and 4 µL/min, respectively. The instrument was operated with inorganic carbon removal enabled. The organic carbon is then oxidized by a UV/persulfate-catalyzed reaction to CO_2, which is transferred across a permeable selective membrane into water to form bicarbonate ions, which is quantified by a conductivity detector. Calibration was verified against potassium hydrogen phthalate (KHP) standards. More details about the selection of TOC instrument are provided in the Appendix C.

The purpose of the batch TOC measurements was to determine the PVA and PLGA oxidation efficiency on known samples, which were then applied as correction factors to all reported TOC values (including those taken in online measurements using the same TOC instrument settings). All samples were diluted to a target concentration of ≈ 10 mg C/L. For PVA, the oxidation efficiency was calculated by comparing the measured TOC (g C/L) to the theoretical carbon concentration on PVA standards of known mass concentration dissolved in DIW, where C represents 54.5 % (w/w) of the total PVA mass. Preparing PLGA standards in aqueous media was not feasible because of its poor aqueous solubility. Therefore, the PLGA oxidation efficiency was computed indirectly by measuring the TOC on unpurified NPs (where the concentrations of both PVA and PLGA are known from the synthesis), then subtracting the contribution of the

76

PVA to the TOC signal (considering the known PVA concentration as C and its oxidation efficiency) to obtain the measured C concentration for PLGA to compare against the expected theoretical value. For PLGA, C represents 46.2 % (w/w) of the total mass.

4.3.4 Release Experiments

To evaluate the dye release profile from the PLGA-C6 NPs, the purified NP stocks (1 g/L) were diluted in PBS (preheated to 37 °C) to obtain a final concentration of 0.25 g/L (as PLGA). The NP suspension was held in a 50 mL polypropylene centrifuge tube (Corning, Tewksbury, MA, USA) and maintained at 37 °C in a heated bath sonicator (Branson 1800, Emerson, St. Louis, MO, USA) without sonication. Dialysis was not used because our prior study showed evaporative losses from within the dialysis unit at 37 °C, which would complicate validation of C6 measured in the NPs over time. Notably, sorption to the polypropylene container was also observed and found to be important to maintain sink conditions, as discussed in the SI.

To acquire samples to analyze using the multi-detector AF4 approach, 0.4 mL of the NPs were collected at different time intervals (0 h to 96 h) into HPLC vials with inserts and were injected immediately onto the AF4 instrument (Section 4.3.5) without further treatment. Samples of 1.5 mL of the NPs were also collected for LC-UV-QTOF analysis and immediately centrifuged in Eppendorf Protein LoBind centrifuge tubes at 13000 rpm (12641g) for 23 min (MiniSpinPlus, Eppendorf, Hamburg, Germany). The aqueous supernatant was collected for analysis, and the remaining NP pellets were kept refrigerated in the dark for further until further processing. To extract the remaining

entrapped C6 and soluble portions of polymer from the NP pellets at each time point, 1.48 mL of acetonitrile was added to each centrifuge tube to reach the initial sample volume. Then, the samples were vortexed for 10 s and rotated end-over-end at 25 rpm at room temperature for 1 h, followed by centrifuging at 13000 rpm for 23 minutes to pellet any undissolved material. 200 μL of the acetonitrile extracts were mixed with 200 μL of DIW for LC-UV-QTOF analysis. (Note preliminary tests showed substantial filter loss of C6, so no further purification was performed beyond centrifugation.) The release experiments were performed on four independently synthesized batches of NPs.

4.3.5 Multi-detector AF4-UV-LS-FLD-RI-TOC Analysis

The multi-detector AF4 system for direct quantification of the C6-loaded PLGA NPs includes an AF4 module (Eclipse AF4, Wyatt Technology, Santa Barbara, CA, USA) with a short channel containing a spacer (height of 250 μm) attached to an Agilent 1290 Infinity LC system (Agilent, Santa Clara, CA, USA). The LC system includes a binary pump, degasser, and autosampler. The AF4 mobile phase was phosphate buffer (4 mM, pH 7) with Na_2SO_4 (25 mM). The Na_2SO_4 was selected for compatibility with the online TOC detector, as Cl^- oxidation must be avoided. The AF4 sample injection and detector flow rates were set to 0.2 and 0.5 mL/min, respectively. The injection volume was 100 μL with a total run duration of 100 minutes for each sample. The same setting and flow setup was used as optimized in our previous work for similarly sized PLGA NPs (Appendix C, Table C.2). Two ultrafiltration membrane types were evaluated for the accumulation wall, 10 kDa regenerated cellulose (RC) (Ultracel PLCGC, MilliporeSigma) were die-cut in-house from sheet membranes, and 30 kDa

polyethersulfone (PES) (Microdyn-Nadir, supplied by Wyatt Technology). The RC membrane resulted in higher recovery of the PLGA NPs. However, overall the results for loading and release were similar after normalizing the fluorescence signal for the C6 to the NP concentration (either by UV, RI, or TOC detection), demonstrating the robustness of the data analysis approach. Therefore, results were averaged across four replicates using both membranes.

Online detectors included an Agilent 1260 Infinity UV-Vis diode array detector (DAD) and fluorescence detector (FLD), Wyatt DAWN HELEOS II multi-angle light scattering (MALS) and dynamic light scattering (DLS) (or quasi-elastic light scattering) detectors, a refractive index (RI) detector (Wyatt, Optilab T-rEX), and total organic carbon (TOC) detector (Sievers M9-SEC portable TOC analyzer) configured in flow mode with turbo measurement to collect a TOC measurement every 4 s. Detectors were ordered as UV DAD $\rightarrow$ MALS/DLS $\rightarrow$ FLD $\rightarrow$ RI $\rightarrow$ TOC, with optical detectors ordered from highest to lowest flow cell pressure limit and TOC as the final detector given the destructive detection mode. The UV DAD was set to 350 nm wavelength as the primary wavelength for PLGA NP detection, with full spectra collected from wavelength 190 nm to 600 nm (step 2 nm). For FLD, the optimal excitation and emission wavelengths for C6 detection were set as 450 nm and 510 nm, respectively, with a photomultiplier tube (PMT) gain of 13. These wavelength settings minimized scattering interferences, with a fluorescence peak observed at 510 nm emission. Emission spectra were also collected from 460 nm to 890 nm (5 nm step size). The DLS detector was located at the 140° scattering angle, and the measurement duration was 5 s. The MALS data were analyzed using the Berry formalism as the optimal selection for

the size range of NPs measured here.[195, 254] For online TOC measurements, effluent from the RI detector was routed directly to the TOC analyzer, and the same acid and oxidizer flow rates were used as in the batch TOC setup. The hardware and software for data integration are described in the Supporting Information.

4.3.6 LC-UV-QTOF Quantification

LC-UV-QTOF analysis was performed on the supernatants from the purification steps after the NP synthesis, as well as supernatants and acetonitrile extracts of all NP pellets collected from the release experiments. The analysis was performed on an LC system (1260 Infinity II, Agilent Technologies) with binary pump and degasser, thermostatted autosampler (held at 4 °C, sample injection volume of 20 µL, needle flush of 5 s in LC-MS grade methanol) with integrated column compartment (held at 40 °C), Zorbax Eclipse Plus C18 Rapid Resolution High Definition (RRHD) column (2.1 x 50 mm, 1.8 µm), and UV-Vis DAD set to monitor the 449 nm wavelength for C6 quantification. The mobile phase solvents were A, 0.1 % formic acid in water, and B, acetonitrile and total flow rate was 0.3 mL/min. A gradient elution was run, hold at 5 % B for 2 min, ramp to 40 % B from 2 to 5 min; ramp to 95 % B from 5 to 20 min; hold at 95 % B from 20 to 24 min; ramp to 5 % B from 24 to 25 min; and hold at 5% B from 25 to 30 min to re-equilibrate. QTOF analysis was performed on an Agilent 6545 QTOF mass spectrometer with a dual Agilent jet stream (AJS) electrospray ionization (ESI) source in positive ion mode. The first two minutes of each sample run was diverted to waste, then the remainder of the run to ESI-QTOF analysis. Mass spectra were collected from 60 to 1700 *m/z* in full scan mode (no precursor selection or collision energy

applied). The ESI source settings and additional details are listed in the Supporting Information. Data were collected into MassHunter Acquisition B.09.00 and processed in MassHunter Qualitative Analysis 10.0 and MassHunter Mass Profiler 10.0.1. All LC-UV-QTOF measurements were conducted by Dr. Stacey M. Louie.

4.4 Results and Discussion

4.4.1 Batch Characterization of PLGA-C6 NPs

Batch measurements of the purified PLGA-C6 NPs yielded a z-average hydrodynamic radius (R_h) of 100 ± 2 nm and zeta potential of -4 ± 2 mV, respectively. TEM images showed a range of NP sizes, e.g., from 50 nm to 100 nm radius (Figure C.1), where the smaller sizes by TEM compared to batch DLS may be attributable to shrinking of the NPs under the vacuum, as well as the z-averaged weighting of the DLS size distribution toward larger NP sizes. DSC results yielded a T_g of 44.8 °C, similar to that reported by the manufacturer for the pure PLGA of 46 to 50 °C.[255] The NPs are hence expected to be in the glassy state at the temperature of 37 °C used in the release experiments.

Quantification of C6 by LC-UV analysis for both supernatants and the NP pellets from the synthesis resulted in an entrapment efficiency and dye loading of 60 ± 4 % and 0.8 ± 0.1 µg C6/mg PLGA ($n = 4$ replicates), respectively. These results are close to previously reported values of 70 to 80 % encapsulation efficiency and 0.1 % (w/w) C6 loading in PLGA when using similar ratios of materials in the synthesis.[256]

4.4.2 AF4 with Online TOC Detection for Nanoformulation Purity Analysis

Product purity is an important quality assurance measure for nanoformulations, along with the particle size distribution and aggregation state. Here, we report the first coupling of AF4 with online TOC detection for nanoformulation analysis, to our knowledge. Prior to coupling AF4 with TOC, batch TOC measurements were first conducted on known samples to determine oxidation efficiency of the two major components by mass (PVA and PLGA) used in the NP synthesis. An oxidation efficiency of 93 ± 4 % (n = 3 replicates) was determined on PVA standards. Furthermore, using the indirect approach presented in the Methods, an oxidation efficiency of 77 ± 7 % (n = 3 replicates) was determined for the PLGA NPs.

To evaluate formulation purity, the unpurified PLGA-C6 NPs (containing 0.25 g/L of PLGA along with all unincorporated C6 and a total of 0.75 g/L of PVA surfactant) and purified NPs (0.25 g/L of PLGA and any bound C6 and PVA) were evaluated by multi-detector AF4 analysis. For both samples, the online DLS measurements confirmed size separation of the polydisperse NPs, with the NPs eluting from around 20 to 60 min with R_h ranging from 70 nm to 120 nm across the full width half maximum (FWHM) of the light scattering peak (Figure 4.2). A void peak also elutes around 10 to 20 min that comprises materials such as excess PVA that are larger than the membrane pore size (10 to 30 kDa) but smaller than the NPs. Qualitatively, a clear difference is observed when comparing the chromatograms acquired by different online detectors, with the TOC and RI detectors much more sensitive than the UV detector to the excess polymer in the unpurified sample (Figure 4.2).
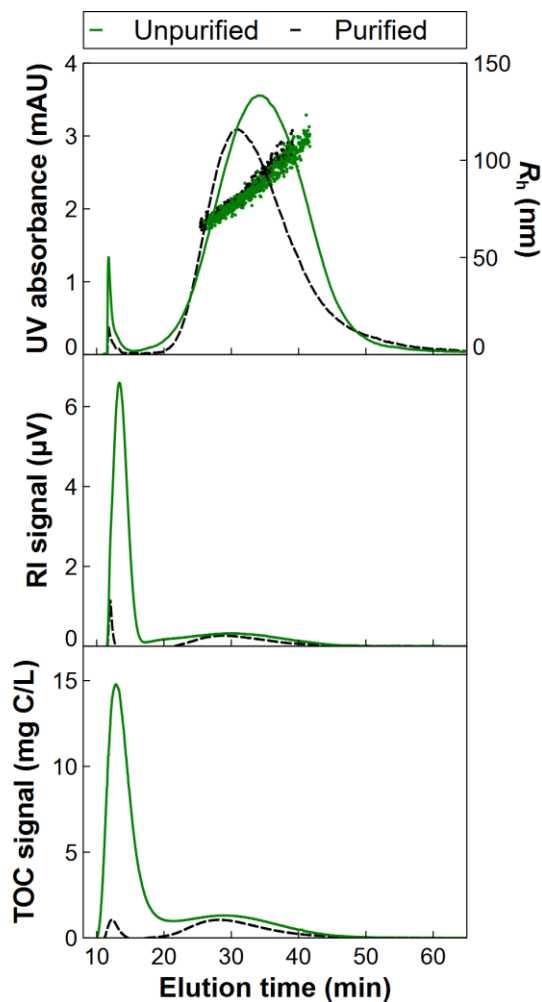
Figure 4.2. AF4-UV, AF4-RI, and AF4-TOC chromatograms and hydrodynamic radius (R_h) for purified and unpurified PLGA-C6 NPs (0.25 g/L as PLGA).

One critical advantage of the online TOC detector is that the polymer and NP mass concentrations eluting in the AF4 analysis can be quantified unambiguously given knowledge of the chemical formula and hence % C by mass for the polymers in the samples. Hence, a mass recovery from the AF4 channel can easily be computed. Based on the sample injection volume (100 μL), concentrations of PVA and PLGA in the syntheses, and the measured TOC oxidation efficiency from the batch analysis, we would expect measured masses of 0.038 mg C in PVA and 0.009 mg C in PLGA in the

injected samples. The actual TOC chromatograms show a recovery of 0.033 ± 0.003 mg C and 0.010 ± 0.002 mg C in the void peak (excess PVA) and main peak (PLGA NPs), respectively. That is, 93 ± 8 % C recovery across the entire peak area (both free PVA and PLGA NPs), and 87 ± 7 % and 120 ± 20 % for mass recovery of PVA and PLGA NPs, respectively, were obtained. The error in the separately evaluated peak recoveries may be attributable to the incomplete separation of PVA and PLGA peaks (Figure 4.2). The overall results demonstrate the suitability of TOC as an absolute and easily interpretable mass concentration detector.

For comparison, mass concentrations can be challenging to interpret directly from the RI or UV signals. For RI analysis, dn/dc of both PVA and the PLGA NPs would need to be determined. While reference values are available for PVA (0.143 mL/g for 88% hydrolyzed PVA),[257] dn/dc for PLGA is generally reported only for the dissolved polymer in organic solvent. The mass recovery on the PVA void peak in the unpurified samples was 130 ± 52 % by RI analysis. For UV analysis, a UV extinction coefficient is required to relate absorbance to concentration. For small molecules, such analysis is appropriate. However, for NPs, the measured transmittance becomes significantly impacted by light scattering, which has a strong size dependence and is hence not directly proportional to mass concentration across a range of NP sizes. Hence, the UV signal would suggest that only 3 ± 1 % of the unpurified sample consists of free polymer (as opposed to 76 ± 3 % by TOC analysis), because the UV signal is disproportionately weighted toward the large NPs.

For the purified NPs, a mass recovery of 70 ± 5 % on the PLGA NPs was measured by AF4-TOC analysis using the 10 kDa RC membrane, or 44 ± 12 % using

the 30 kDa PES membrane, respectively. NP losses in the purified samples are attributable to attachment to different compartments of the instrument (i.e., the membrane, tubing, etc.) and are reasonably higher when the excess surfactant is not injected as in the unpurified sample. Note that a *relative* mass recovery analysis is possible using both UV and RI detection but again entails further complication beyond the absolute mass analysis by TOC. To evaluate NP recovery without a reliable dn/dc or UV extinction coefficient, injection of the NPs with no applied cross flowrate is necessary with an assumption that no losses are incurred. By comparing the peak areas with and without cross flow (for an equivalent injection volume), recoveries of 88 ± 10 % and 48 ± 15 % were obtained for RC and PES membrane, respectively, using the UV detector. Overall, the results confirm the advantage of TOC over UV and RI detection as a universal, unambiguous detector for obtaining absolute mass concentrations of dissolved polymers and polymer NPs in the nanoformulations.

4.4.3 AF4-TOC for Scattering-free PLGA NP Concentration Analysis

As noted, UV transmittance is influenced both by true absorbance and light scattering away from the detector. The scattering from spherical particles and the dependence on size and scattering angle can be modeled by the Mie scattering function. Although true UV absorbance is theoretically proportional to mass concentration by the Beer Lambert law, the Mie scattering is not when comparing differently sized particles, with larger particles tending to scatter disproportionately greater light. Hence, we would expect the apex location in the UV chromatogram to be skewed toward larger particles. This expectation was confirmed experimentally, the peak shape and elution time for the

UV detector is more similar to that of the LS detector, whereas the RI and TOC detectors show peak apexes eluting at earlier times (Figure 4.3). These qualitative results support the expectation that the TOC signal is proportional to the mass of the particle; therefore, the peak location represents the sample fraction with higher concentration.
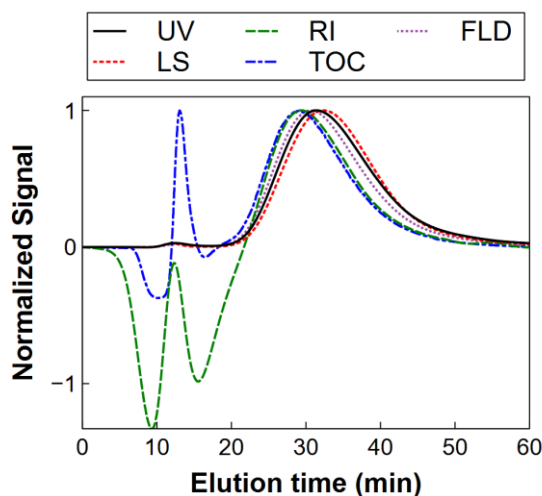
Figure 4.3. AF4-UV-LS-FLD-RI-TOC chromatograms for purified PLGA-C6 NPs (0.25 g/L in PBS). All signals were normalized to their maximum value during the NP elution (18-50 min).

The FLD signal is selective to the drug (see Figure 4.1 inset comparing FLD spectra for C6-loaded and "empty" PLGA NPs synthesized in the same manner except without C6). Hence, dividing the FLD signal by the NP signal (either by UV, RI, TOC) can be indicative of the loading. We explored the implications of having a "true" mass concentration versus scattering-impacted signal by evaluating the "apparent" dye loading profiles across the NP size distribution for both the PLGA-C6 NPs here, and enrofloxacin-loaded PLGA NPs synthesized in our prior AF4 method development study as a second case (Figure C.4). In brief, we observed opposite trends in apparent loading across the size distribution when using the raw UV signal versus the TOC signal to determine NP concentrations. The RI signal appears to confirm the reliability of the

86

TOC signal. In order to attempt to reconcile the observed difference of the UV signal, an approximation to the Mie scattering function across the NP size range of interest was determined and used to develop a correction factor to normalize for the influence of size to the scattering signal (details in Appendix C, Figure C.5). Applying this correction factor allowed the same trend to be recovered as for the TOC and RI detectors. The need to apply advanced Mie scattering corrections to the UV data emphasizes that UV detection would be poorly suited to monitor particle concentrations and hence drug loading in any samples where the particle is swelling/shrinking or degrading and thereby changing size.

Overall, uncertainty persists in the use of the raw FLD signals to evaluate absolute drug loading. In particular, it is unclear whether the trend of increasing apparent loading with increasing size (Figure C.4) represents genuine differences in loading, or whether the results are influenced by any size-dependent quenching, inner filter, or scattering artifacts. Therefore, we suggest that the absolute FLD_{drug}/NP signal should not be interpreted directly as the absolute loading at each elution time, but rather as in our previous work, we only semi-quantitatively evaluate the FLD_{drug}/NP signal for samples collected at different release times relative to the initial FLD_{drug}/NP at time zero, thereby normalizing for any size-dependent differences in loading, fluorescence quenching, or other artifacts. Such approaches for fluorescence analysis are not atypical, for example, Carrillo-Carrion et al. investigated the loss of fluorescently-labeled polymer and protein from quantum dots and normalized all temporal data for each sample to the fluorescence of the same sample at time zero, hence allowing a semi-quantitative analysis of changes in these complicated systems.[258]

4.4.4 Transformations of the PLGA NPs During the Release Experiments

AF4 is most commonly used to measure size distributions and identify any changes in particle size (e.g., due to aggregation, degradation, shrinking, or swelling). Here, no significant change in the hydrodynamic size of the nanoparticles was observed over the duration of the 96 h release experiment by either batch DLS or AF4-DLS (Figure C.6), and furthermore, no significant change in the radius of gyration was observed, with the shape factor (R_g/R_h) remaining consistent over time (Figure C.7). Furthermore, the AF4-TOC results showed a consistent recovery of C from the injected NP samples. Therefore, no significant transformations of the PLGA NPs, such as degradation or swelling, occurred during the release experiment.

These measurements were complemented with LC-QTOF analysis after extraction of pelleted NPs in acetonitrile. In addition to validating the C6 release (discussed in Section 4.4.5), the LC-QTOF analysis revealed that small oligomeric PLGA species were separated on the HPLC column (chromatograms in Appendix C, Figure C.8). By analyzing PLGA standards of the stock material in acetonitrile, we confirmed that these low MW species are present in the stock PLGA and are not degradation products. Oligomeric species belonging to the polymer series, i.e., with various numbers of lactide or glycolide monomer units, were extracted from the data and plotted as MW versus retention time (RT), with both the composition (i.e., relative number of lactide and glycolide units) and abundance visualized in Appendix C Figure C.9. The data processing approach for the data visualization is described in the SI. The data analysis was applied on samples collected at all release times from 0 to 96 h to then identify trends in abundances of the oligomeric PLGA, with data for select release times

overlaid in Figure 4.4 and data for select species plotted in Appendix C, Figure C.10. The PLGA NPs showed more rapid and extensive losses of the lower molecular weight, more hydrophilic species over time, with glycolide units being more hydrophilic than lactide units because of the methyl side chain on the lactide. In summary, the multi-detector AF4 and LC-QTOF analyses serve complementary roles, with AF4 demonstrating that the overall PLGA NP (including the bulk of the PLGA matrix) remains intact, whereas LC-QTOF analysis gives a detailed picture of the fate of the small oligomeric PLGA species.
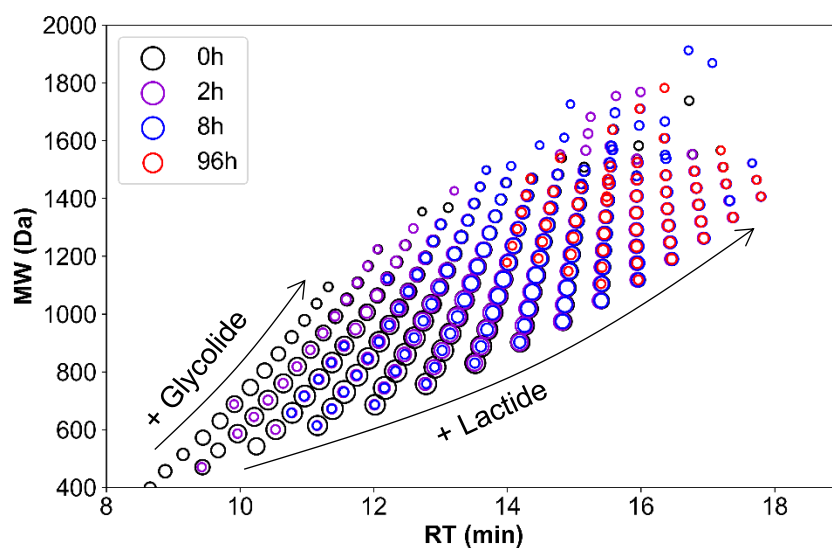
Figure 4.4. MW of the polymer versus the RT for acetonitrile extracted PLGA-C6 NPs released in PBS from 0 to 96 h at 37 °C. The size of each point represents the abundance of each polymer.

4.4.5 Measurement of Bulk Release Profiles by Multi-Detector AF4 Analysis and Validation Against LC Analysis

Here, we apply the multi-detector AF4 method for direct evaluation of C6 release from the PLGA NPs over time at 37 °C in PBS. All detectors were employed for all samples. Here, we focus primarily on release profiles acquired using FLD as the C6 detector and TOC as the NP mass concentration detector, with comparisons also made when using UV or RI detection for the NPs (Figure 4.5). To obtain the *bulk* release profile across the entire NP population, the *integrated* peak areas are used for the analysis. A slow release of up to ≈ 75% of the initial C6 loading is observed over 96 h. Importantly, because both the batch DLS and online AF4-DLS measurements showed no significant change in the PLGA NP size over time (Figure C.6, C.7); therefore, the UV signals can be appropriate to compare between time zero and later time points to obtain the relative drug loading, and hence the release profiles obtained by using either TOC or UV as PLGA concentration detector were similar (Figure 4.5). However, for any potential cases where the NP size changes over time, e.g., due to shrinking/swelling, degradation, or aggregation, we emphasize the necessity of the TOC detector over the UV detector as a true mass concentration detector for the PLGA NPs, regardless of their size or aggregation state. The RI detector was unreliable for NP concentration detection given the baseline issues and low signal (Figures 4.2b and 4.3); results when using RI for NP detection are displayed in Figure 4.5 for comparison, but RI was not used for further analysis.
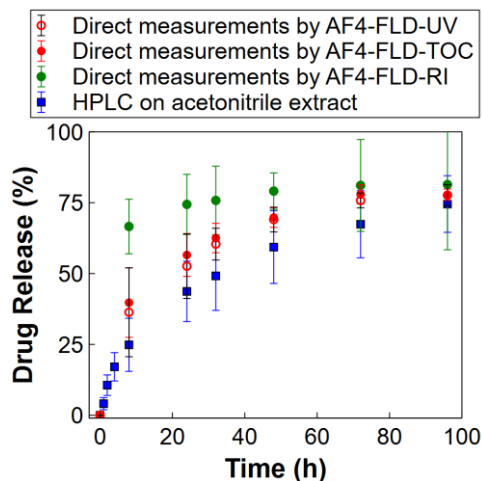
Figure 4.5. Bulk release profiles of C6 from PLGA-C6 NPs obtained by multi-detector AF4 analysis and validated against LC analysis on acetonitrile extracts of the NPs.

To validate the AF4 measurements, an acetonitrile extraction method was used to extract C6 from the NPs after pelleting by centrifugation and removing the supernatant. All LC-UV-QTOF measurements were conducted by Dr. Stacey M. Louie. As Figure 4.5 shows, both the AF4-FLD and solvent extraction technique consistently suggest that ≈ 75 % of the initial C6 loading is slowly releasing over 96 hours. Other indirect approaches to measure the dissolved C6 were not feasible because significant dye loss was observed when attempting to separate NPs from the dissolved C6 using several method, including filtration, ultrafiltration, and dialysis. Similarly in the experiments conducted here with the PLGA-C6 release performed in polypropylene tubes followed by centrifuging to separate the NPs, very low concentrations of C6 were measured in the supernatant, indicating the released dye sorbs to the plastic containers. Therefore, the multi-detector AF4 approach can be highly advantageous in this scenario because the NP-associated drug is directly evaluated, and NP recovery during the

91

release experiment does not suffer the same losses as the dissolved C6. Furthermore, no sample processing is required after sample collection at each time point.

We attempted to fit the bulk release profiles with several commonly applied models, including first-order kinetics, radial diffusion,[238] [239] the Higuchi model,[259] [260] the Korsmeyer-Peppas model,[261] [262] the Baker-Lonsdale model, and the Hixson-Crowell[263] or Hopfenburg model[264, 265] (Appendix C, Table C.3, Figure C.11). The results show that nearly all of the models can produce reasonably good fits to the data despite having different assumptions and derivations, and hence different physical interpretations. For example, the first-order model assumes diffusion across a thin-film barrier from a depleting well-mixed source (the NP) to perfect sink conditions (or alternatively, dissolution from an infinite source with accumulation in the bulk media up to the solubility limit as the Noyes-Whitney model[266]). On the other hand, the radial diffusion model assumes the drug is initially evenly dispersed within a spherical NP but then accounts for spatial heterogeneity over time, with release slowing over time as drug depletes from the exterior and diffuses outward from the interior of the NP. The fitted Korsmeyer-Peppas exponents were not significantly different from the theoretical value of 0.43 suggesting Fickian diffusion.[261, 267] Even more notable, models that are obviously irrelevant to the system, such as the Higuchi model for dissolution from a planar film, the Hixson-Crowell model for dissolution from a shrinking tablet, or the Hopfenburg model for release from erodible polymers, can also fit the release profiles. In short, the release mechanism is poorly identifiable when only considering the bulk time-dependent dye release, and it would not be possible to deduce the particle structure, the initial dye distribution, or the mechanism by which release is occurring.

4.4.6 Size-dependent Release Analysis by Multi-detector AF4 to Explore Release Mechanisms

We propose that by taking full advantage of the high resolution size separation and online detection capabilities of the multi-detector AF4 system, size-dependent drug release can be analyzed by monitoring the drug loading at each eluting size fraction over time to more definitively narrow the possible number of theoretical release mechanisms that could be consistent with the experimental data. As opposed to using integrated peak areas across the entire NP population to obtain bulk release profiles (as in Figure 4.5), here the relative change in the ratio of FLD/TOC (or FLD/UV) over the release duration is monitored at each chromatographic time point corresponding to a different size of NPs (Figure 4.6a and Figure C.12). Again, consistent results were achieved regardless of the selection of TOC or UV for the NP detector because all data are normalized to time zero of the release experiment, and the NP size did not significantly change over the 96 h experiment duration.

For simplicity, a first-order loss equation ($C(t) = C_\infty + C_0 \exp(-kt)$) was fitted to the experimental data for drug remaining in each size fraction of NPs over time to estimate the drug transfer rate constant (k), remaining dye loading for any firmly entrapped dye (C_∞), and C_0 for the initial dye loading in the NPs at time zero. The results indicate that the C6 transfer rate is largely independent of the size of the PLGA NP (Figure 4.6a, Figure C.12). These results are particularly remarkable in contrast to our previous study, in which the same analyses performed on enrofloxacin-loaded PLGA NPs showed a clear linear relationship between k and $1/R^2$, consistent with radial diffusion of entrapped drug through the matrix (Figure 4.6b).
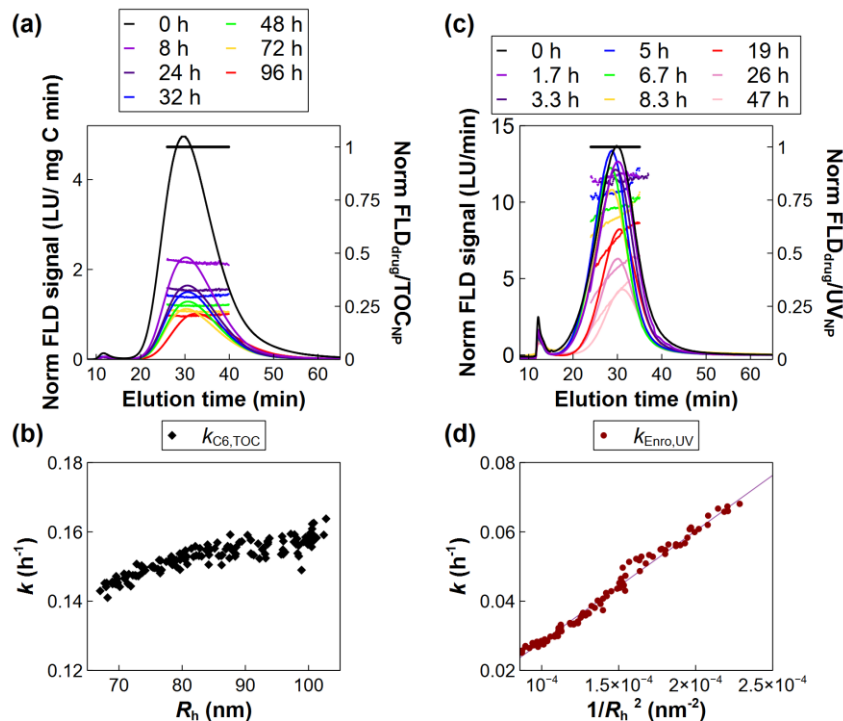
Figure 4.6. AF4–FLD chromatograms normalized to PLGA concentration, and size-dependent analysis.

Here, we propose that the underlying reason for the different size-resolved release profiles is a difference in drug localization in or on the NPs. If the C6 being released from the NPs were evenly distributed throughout the PLGA matrix, a strong size dependence should be observed, similar to the enrofloxacin release. Given that this is not the case, we hypothesize that the majority of the C6 must be precipitated at or near the surface of the particles. Therefore, dissolution occurs directly from the NP surface and no distance within the NP needs to be traversed to reach the interface and then dissolve in the media (Figure 4.7). As such, the first-order release model would be the most appropriate representation of this scenario, whereas other models for diffusion through a spherical matrix (e.g., radial diffusion, Baker-Lonsdale, and Korsmeyer-

94

Peppas models) would not be suitable regardless of goodness of fit to the bulk time-resolved data.
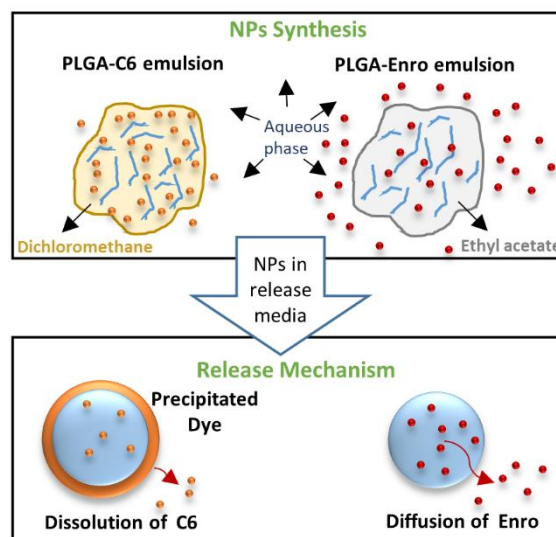
Figure 4.7. Schematic of emulsion formed during PLGA-C6 or PLGA-Enro synthesis, as well as the proposed release mechanism

The slow dissolution of a hydrophobic compound from the NP surface can be considered a "burst" release of surface-localized C6. This interpretation is consistent not only with other evidence in our studies, but also those reported in the literature. For example, the T_g measured for the PLGA NPs here ($\approx$ 45 °C) is near that for the pure PLGA[268], and also higher than the temperature of 37 °C used in the release experiments. Our prior study on enrofloxacin-loaded PLGA NPs showed a lower T_g of $\approx$ 32 °C and importantly, that the entrapped enrofloxacin only showed release at temperatures near or surpassing T_g. These results are consistent with enrofloxacin being mixed within the PLGA matrix, whereas C6 is not (and hence does not influence the T_g substantially and furthermore, can release by surface dissolution even at temperatures below T_g). It is

95

unclear whether the loss of the low molecular weight PLGA oligomers observed in the QTOF analysis can influence the C6 release or where these oligomers are distributed in the particle; however, the rate of loss of the oligomeric species (Figure C.11) generally do not appear to correspond to the rates of C6 release (Figure 4.6), suggesting a lack of correlation between oligomer and C6 loss.

Secondly, the measured release appears to plateau at around 75 % of the total loaded drug (from fitting C_∞ for the bulk release profile in Table C.3), consistent with the presence of two populations of C6, 75 % at the surface (the "burst" release) and 25 % entrapped within the NPs. This drug distribution profile could be indicative of poor miscibility or solubility of C6 with the PLGA phase – such an issue has previously been modeled and experimentally demonstrated for tetracycline separating and precipitating in "islands" on the surface of PLGA films, rather than dispersing within the film.[269] In this scenario, the amount of C6 that is truly "entrapped" during the synthesis should be related to its equilibrium solubility in the PLGA, and hence different proportions of entrapped and burst (surface) C6 would be expected depending on the ratio of C6 to PLGA, with higher ratios resulting in higher proportions on the surface that cannot dissolve into the PLGA. This expectation also appears to be consistent with a close inspection of the literature (Appendix C, Table C.1). Corrigan et al. used a lower C6 to PLGA ratio of 0.25 µg/mg (as opposed to 1.0 µg/mg here) and report only a minimum burst release of < 1 % in the first day, followed by a subsequent slow release of entrapped C6 due to degradation or erosion of the PLGA over 45 d.[270] Qaddoumi et al. similarly used a lower C6 to PLGA ratio of 0.55 µg/mg and reported only 0.32 % release over 24 h, suggesting most of the C6 is firmly entrapped in their NPs as well.[271] On the

other hand, Pietzonka et al. prepared PLGA-C6 NPs with a similar loading (nominal 0.1% or 1 μg/mg) as used here, and show results that can be consistent with a higher percent of C6 at the surface.[256] In particular, C6 release rates and extents were found to change from virtually no release within 3 h, to slow release up to > 25% at 3 h when liposomes were introduced to the media but separated from the NPs across a dialysis membrane, and then to rapid release up to 50% when the direct mixing and contact between the NPs and liposomes was allowed.[256] The influence of the liposomes without direct physical contact can be consistent with uptake of the lipophilic C6 to maintain sink conditions and avoid reaching a solubility limit (as also reported in this study when testing different container materials), and the significant influence of liposome-PLGA contact would suggest a direct surface transfer of C6 from the PLGA NPs to the liposomes.

Notably, many studies (Appendix C, Table C.1) synthesize PLGA-C6 NPs with much higher C6 to PLGA ratios than discussed in these release studies and aim to use the NPs to track NP uptake or distribution in biological systems by fluorescence imaging. As discussed by Pietzonka et al., caution must be applied in such studies because surface transfer of C6 to lipid membranes (rather than NP uptake) is likely to occur.[256] Ideally, the fluorescent label should be fully entrapped within the NP to mitigate surface transfer. It may be the case that preferential localization of drugs near the NP surface may more common than generally acknowledged, with characterization tools only recently becoming available to identify such issues.[240] This study demonstrates that size-resolved multi-detector AF4 analysis can be a valuable screening

tool to deduce localization and release mechanisms and evaluate whether a nanoformulation meets the desired design criteria.

4.4 Conclusions

This study demonstrates the first direct coupling of AF4 with online TOC detection to evaluate the purity and concentration of polymeric nanoformulations and the advantages of the TOC as a more robust, unambiguous detector for the quantification of polymeric NPs to evaluate changes in drug loading over time. Furthermore, the novel mechanistic value of acquiring size-dependent release profiles on top of the common time-dependent bulk release profiles was exemplified when comparing PLGA-C6 and PLGA-enrofloxacin NPs. The size-dependent data enables a clearer distinction of the dye distribution inside or on the particles and more detailed insight into the release mechanism. Based on the AF4 results, we would suggest that at sufficiently high C6 to PLGA ratios, the majority of the dye in the synthesized PLGA-C6 particles is precipitated near the surface and releases by dissolution rather than radial diffusion through the matrix. Overall, the analysis provided in this study is not only limited to C6 release from polymeric NPs but can be extended to probe the release of any inherently fluorescent or fluorescently tagged compounds, both to investigate release mechanisms and to rapidly screen products for the desired behavior. This case study represents a major advancement in demonstrating the full power of multi-detector AF4 analysis for simultaneous investigation of NP size distributions, NP transformations, formulation purity, drug loading and release, and most significantly, to achieve fundamental insights into the release mechanism.

CHAPTER 5. FUTURE DIRECTIONS

In this section, a brief description of the future direction and potential continuation of this work are provided. In the second chapter of the dissertation, the evaluation of the competitive adsorption of the macromolecules onto titanium oxide nanoparticles was achieved by utilizing various analytical techniques such as *in situ* ATR-FTIR and size exclusion chromatography coupled to UV-Vis, refractive index (RI), and fluorescence detection (FLD). As complementary measurements to the presented data, the characterization of the size of the particles as well as their surface chemistry can be monitored simultaneously by using separation techniques like asymmetric flow field flow fractionation (AF4) coupled to various light scattering and spectroscopy detectors. The application of this method was previously shown for nanoplastics,[272] carbon nanotubes,[272] and silver nanoparticles[273] in media containing natural organic matter. However, the use of this novel method for surface characterization of the nanomaterials in more complex systems containing different types of macromolecules has not been demonstrated yet.

Additionally, the subsequent effect of different surface chemistries, as a result of adsorption of macromolecules onto titanium dioxide (TiO_2) nanoparticles, on the functionalities of the particles, such as photoreactivity for degradation of contaminants, needs to be further explored. The effect of adsorption of a protein,[16] fulvic acid,[16] natural organic matter[274] onto TiO_2 particles were reported in previous studies. By assessing the NPs reactivity in solutions containing various types of macromolecules, mimicking the water treatment environments, a better assessment of the actual NPs degradation efficiency in natural environments can be obtained.

In Chapter 3 and 4 of the dissertation, the use of asymmetric flow field-flow fractionation with multiple detectors, including FLD, was demonstrated for characterization of the NPs containing inherently fluorescent dye/drug. The concept of controlled release is not limited to drug delivery applications. It can also be extended in different fields such as pesticide/herbicide delivery in agriculture, and using nanocapsules for the controlled delivery of antimicrobial agents for food industry (food packing) applications. Therefore, we expect the characterization methods developed here to have a broad impact to characterize NPs for the controlled release of active ingredients. Additionally, by fluorescently tagging the non-fluorophore compounds, this method can be extended to even broader ranges of the active ingredients.

Finally, to fully evaluate and predict the "actual" drug release behavior of drug-loaded nanoparticles in the biological milieu, the adsorption of macromolecules onto their surface needs to be considered. The adsorption of the biological constituents can have different effects on that drug release behavior. For example, decrement in the drug release rates due to the formation of the surface coating (corona) (obstructing the available site for the drug to diffuse from the NP)[275, 276] or acceleration in the drug release rates due to degradation of polymeric NPs can be expected. Additionally, depending on the amount of adsorbed proteins and the composition of the hard/soft corona, we might observe different drug release behaviors.[275, 276] We believe that the demonstrated asymmetric flow field-flow fractionation coupled with various online detectors (e.g., UV, MALS, RI, TOC, FLD), can enable studying the effect of different interactions between small molecules, macromolecules, and nanoparticles on the drug release behavior by direct monitoring of the drug loading. Additionally, by monitoring

the particle size under different conditions (i.e., pH, exposure to various types of macromolecules), the release mechanisms (e.g., swelling, degradation, and diffusion) can be distinguished, which can help on further improvement of nanocarriers' designs for more effective controlled drug release.

REFERENCES

1.   Kanchi, S.; Ahmed, S.; Sabela, M. I.; Hussain, C. M., *Nanomaterials: Biomedical, Environmental, and Engineering Applications*. John Wiley & Sons: 2018.

2.   Louie, S. M.; Tilton, R. D.; Lowry, G. V., "Critical review: impacts of macromolecular coatings on critical physicochemical processes controlling environmental fate of nanomaterials." *Environ. Sci. Nano* **2016,** *3*, (2), 283-310.

3.   Saptarshi, S. R.; Duschl, A.; Lopata, A. L., "Interaction of nanoparticles with proteins: relation to bio-reactivity of the nanoparticle." *J. Nanobiotechnol.* **2013,** *11*, (1), 26.

4.   Li, Z.; Shakiba, S.; Deng, N.; Chen, J.; Louie, S. M.; Hu, Y., "Natural Organic Matter (NOM) Imparts Molecular-Weight-Dependent Steric Stabilization or Electrostatic Destabilization to Ferrihydrite Nanoparticles." *Environ. Sci. Technol.* **2020,** *54*, (11), 6761-6770.

5.   Adeleye, A. S.; Conway, J. R.; Garner, K.; Huang, Y.; Su, Y.; Keller, A. A., "Engineered nanomaterials for water treatment and remediation: Costs, benefits, and applicability." *Chem. Eng. J.* **2016,** *286*, 640-662.

6.   Santhosh, C.; Velmurugan, V.; Jacob, G.; Jeong, S. K.; Grace, A. N.; Bhatnagar, A., "Role of nanomaterials in water treatment applications: A review." *Chem. Eng. J.* **2016,** *306*, 1116-1137.

7.   Gopalakrishnan, I.; Sugaraj Samuel, R.; Sridharan, K., Nanomaterials-Based Adsorbents for Water and Wastewater Treatments. In *Emerging Trends of Nanotechnology in Environment and Sustainability: A Review-Based Approach*, Sridharan, K., Ed. Springer International Publishing: Cham, 2018; pp 89-98.

8.   Amin, M. T.; Alazba, A. A.; Manzoor, U., "A Review of Removal of Pollutants from Water/Wastewater Using Different Types of Nanomaterials." *Adv. Mater. Sci. Eng.* **2014,** *2014*, 825910.

9.   Bhatnagar, A.; Sillanpää, M., "Removal of natural organic matter (NOM) and its constituents from water by adsorption – A review." *Chemosphere* **2017,** *166*, 497-510.

10.   Gopinath, K. P.; Madhav, N. V.; Krishnan, A.; Malolan, R.; Rangarajan, G., "Present applications of titanium dioxide for the photocatalytic removal of pollutants from water: A review." *J. Environ. Manage.* **2020,** *270*, 110906.

11.   Ly, Q. V.; Maqbool, T.; Zhang, Z.; Van Le, Q.; An, X.; Hu, Y.; Cho, J.; Li, J.; Hur, J., "Characterization of dissolved organic matter for understanding the adsorption on nanomaterials in aquatic environment: A review." *Chemosphere* **2021,** *269*, 128690.

12.   Mahlambi, M. M.; Ngila, C. J.; Mamba, B. B., "Recent Developments in Environmental Photocatalytic Degradation of Organic Pollutants: The Case of Titanium Dioxide Nanoparticles—A Review." *J. Nanomater.* **2015,** *2015*, 790173.

13.   Lee, S.-Y.; Park, S.-J., "TiO$_2$ photocatalyst for water treatment applications." *J. Ind. Eng. Chem.* **2013,** *19*, (6), 1761-1769.

14.   Ustunol, I. B.; Gonzalez-Pech, N. I.; Grassian, V. H., "pH-dependent adsorption of α-amino acids, lysine, glutamic acid, serine and glycine, on TiO$_2$ nanoparticle surfaces." *J. Colloid Interface Sci.* **2019,** *554*, 362-375.

15.   Mudunkotuwa, I. A.; Grassian, V. H., "Citric Acid Adsorption on TiO$_2$ Nanoparticles in Aqueous Suspensions at Acidic and Circumneutral pH: Surface

Coverage, Surface Speciation, and Its Impact on Nanoparticle−Nanoparticle Interactions." *J. Am. Chem. Soc.* **2010,** *132*, (42), 14986-14994.

16.   Wu, H.; Huang, L.; Rose, A.; Grassian, V. H., "Impact of surface adsorbed biologically and environmentally relevant coatings on TiO_2 nanoparticle reactivity." *Environ. Sci. Nano* **2020,** *7*, (12), 3783-3793.

17.   Artemyev, V. E., *Geochemistry of organic matter in river-sea systems*. <u>Kluwer Academic Publishers</u>: Dordrecht, The Netherlands, 1996.

18.   Thurman, E. M., *Organic geochemistry of natural waters*. <u>Kluwer Academic Publishers</u>: Dordrecht, The Netherlands, 1987.

19.   Zhao, T.; Fang, M.; Tang, Z.; Zhao, X.; Wu, F.; Giesy, J. P., "Adsorption, aggregation and sedimentation of titanium dioxide nanoparticles and nanotubes in the presence of different sources of humic acids." *Sci. Total Environ.* **2019,** *692*, 660-668.

20.   Erhayem, M.; Sohn, M., "Stability studies for titanium dioxide nanoparticles upon adsorption of Suwannee River humic and fulvic acids and natural organic matter." *Sci. Total Environ.* **2014,** *468-469*, 249-257.

21.   Islam, M. A.; Morton, D. W.; Johnson, B. B.; Angove, M. J., "Adsorption of humic and fulvic acids onto a range of adsorbents in aqueous systems, and their effect on the adsorption of other species: A review." *Sep. Purif. Technol.* **2020,** *247*, 116949.

22.   Luo, M.; Huang, Y.; Zhu, M.; Tang, Y.-n.; Ren, T.; Ren, J.; Wang, H.; Li, F., "Properties of different natural organic matter influence the adsorption and aggregation behavior of TiO2 nanoparticles." *J. Saudi Chem. Soc.* **2018,** *22*, (2), 146-154.

23.   Jayalath, S.; Wu, H.; Larsen, S. C.; Grassian, V. H., "Surface adsorption of Suwannee River humic acid on TiO_2 nanoparticles: A study of pH and particle size." *Langmuir* **2018,** *34*, (9), 3136-3145.

24.   Gora, S. L.; Andrews, S. A., "Adsorption of natural organic matter and disinfection byproduct precursors from surface water onto TiO_2 nanoparticles: pH effects, isotherm modelling and implications for using TiO_2 for drinking water treatment." *Chemosphere* **2017,** *174*, 363-370.

25.   Mwaanga, P.; Carraway, E. R.; Schlautman, M. A., "Preferential sorption of some natural organic matter fractions to titanium dioxide nanoparticles: influence of pH and ionic strength." *Environ. Monit. Assess.* **2014,** *186*, (12), 8833-8844.

26.   Schmidt, M. P.; Martínez, C. E., "Supramolecular Association Impacts Biomolecule Adsorption onto Goethite." *Environ. Sci. Technol.* **2018,** *52*, (7), 4079-4089.

27.   Tsai, D.-H.; Davila-Morris, M.; DelRio, F. W.; Guha, S.; Zachariah, M. R.; Hackley, V. A., "Quantitative Determination of Competitive Molecular Adsorption on Gold Nanoparticles Using Attenuated Total Reflectance–Fourier Transform Infrared Spectroscopy." *Langmuir* **2011,** *27*, (15), 9302-9313.

28.   Tsai, D.-H.; Shelton, M. P.; DelRio, F. W.; Elzey, S.; Guha, S.; Zachariah, M. R.; Hackley, V. A., "Quantifying dithiothreitol displacement of functional ligands from gold nanoparticles." *Anal. Bioanal. Chem.* **2012,** *404*, (10), 3015-3023.

29.   Yang, K.; Zhu, L.; Xing, B., "Sorption of phenanthrene by nanosized alumina coated with sequentially extracted humic acids." *Environ. Sci. Pollut. Res.* **2010,** *17*, (2), 410-419.

30.   Wu, H.; Gonzalez-Pech, N. I.; Grassian, V. H., "Displacement reactions between environmentally and biologically relevant ligands on TiO_2 nanoparticles: insights into the aging of nanoparticles in the environment." *Environ. Sci. Nano* **2019,** *6*, (2), 489-504.

31.   Kim, J.; Doudrick, K., "Emerging investigator series: protein adsorption and transformation on catalytic and food-grade TiO_2 nanoparticles in the presence of dissolved organic carbon." *Environ. Sci. Nano* **2019,** *6*, (6), 1688-1703.

32.   Moghimi, S. M.; Hunter, A. C.; Andresen, T. L., "Factors Controlling Nanoparticle Pharmacokinetics: An Integrated Analysis and Perspective." *Annu. Rev. Pharmacol. Toxicol.* **2012,** *52*, (1), 481-503.

33.   Shakiba, S.; Astete, C. E.; Paudel, S.; Sabliov, C. M.; Rodrigues, D. F.; Louie, S. M., "Emerging investigator series: polymeric nanocarriers for agricultural applications: synthesis, characterization, and environmental and biological interactions." *Environ. Sci. Nano* **2020,** *7*, (1), 37-67.

34.   Moreno-Bautista, G.; Tam, K. C., "Evaluation of dialysis membrane process for quantifying the *in vitro* drug-release from colloidal drug carriers." *Colloids Surf., A* **2011,** *389*, (1-3), 299-303.

35.   Mora, L.; Chumbimuni-Torres, K. Y.; Clawson, C.; Hernandez, L.; Zhang, L.; Wang, J., "Real-time electrochemical monitoring of drug release from therapeutic nanoparticles." *J. Controlled Release* **2009,** *140*, (1), 69-73.

36.   Peeters, K.; De Maesschalck, R.; Bohets, H.; Vanhoutte, K.; Nagels, L., "In situ dissolution testing using potentiometric sensors." *Eur. J. Pharm. Sci.* **2008,** *34*, (4), 243-249.

37. Carissimi, G.; Montalbán, M. G.; Víllora, G.; Barth, A., "Direct Quantification of Drug Loading Content in Polymeric Nanoparticles by Infrared Spectroscopy." *Pharmaceutics* **2020,** *12*, (10), 912.

38. Sarraguça, M. C.; Matias, R.; Figueiredo, R.; Ribeiro, P. R. S.; Martins, A. T.; Lopes, J. A., "Near infrared spectroscopy to monitor drug release in-situ during dissolution tests." *Int. J. Pharm.* **2016,** *513*, (1), 1-7.

39. Boetker, J. P.; Savolainen, M.; Koradia, V.; Tian, F.; Rades, T.; Müllertz, A.; Cornett, C.; Rantanen, J.; Østergaard, J., "Insights into the Early Dissolution Events of Amlodipine Using UV Imaging and Raman Spectroscopy." *Mol. Pharmaceutics* **2011,** *8*, (4), 1372-1380.

40. Coutts-Lendon, C. A.; Wright, N. A.; Mieso, E. V.; Koenig, J. L., "The use of FT-IR imaging as an analytical tool for the characterization of drug delivery systems." *J. Controlled Release* **2003,** *93*, (3), 223-248.

41. van der Weerd, J.; Kazarian, S. G., "Combined approach of FTIR imaging and conventional dissolution tests applied to drug release." *J. Controlled Release* **2004,** *98*, (2), 295-305.

42. van der Weerd, J.; Kazarian, S. G., "Release of Poorly Soluble Drugs from HPMC Tablets Studied by FTIR Imaging and Flow-Through Dissolution Tests." *J. Pharm. Sci.* **2005,** *94*, (9), 2096-2109.

43. Hulse, W. L.; Gray, J.; Forbes, R. T., "A discriminatory intrinsic dissolution study using UV area imaging analysis to gain additional insights into the dissolution behaviour of active pharmaceutical ingredients." *Int. J. Pharm.* **2012,** *434*, (1), 133-139.

44.   Berkland, C.; Kipper, M. J.; Narasimhan, B.; Kim, K.; Pack, D. W., "Microsphere size, precipitation kinetics and drug distribution control drug release from biodegradable polyanhydride microspheres." *J. Controlled Release* **2004,** *94*, (1), 129-141.

45.   Berkland, C.; King, M.; Cox, A.; Kim, K.; Pack, D. W., "Precise control of PLG microsphere size provides enhanced control of drug release rate." *J. Controlled Release* **2002,** *82*, (1), 137-147.

46.   Mahalakshmi, L.; Leena, M. M.; Moses, J. A.; Anandharamakrishnan, C., "Micro- and nano-encapsulation of β-carotene in zein protein: size-dependent release and absorption behavior." *Food & Function* **2020,** *11*, (2), 1647-1660.

47.   Pan, R.; Liu, G.; Li, Y.; Wei, Y.; Li, S.; Tao, L., "Size-dependent endocytosis and a dynamic-release model of nanoparticles." *Nanoscale* **2018,** *10*, (17), 8269-8274.

48.   Bezemer, J. M.; Radersma, R.; Grijpma, D. W.; Dijkstra, P. J.; van Blitterswijk, C. A.; Feijen, J., "Microspheres for protein delivery prepared from amphiphilic multiblock copolymers: 2. Modulation of release rate." *J. Controlled Release* **2000,** *67*, (2), 249-260.

49.   Franzen, U.; Nguyen, T. T. T. N.; Vermehren, C.; Gammelgaard, B.; Østergaard, J., "Characterization of a liposome-based formulation of oxaliplatin using capillary electrophoresis: Encapsulation and leakage." *J. Pharm. Biomed. Anal.* **2011,** *55*, (1), 16-22.

50.   Fan, Y.; Marioli, M.; Zhang, K., "Analytical characterization of liposomes and other lipid nanoparticles for drug delivery." *J. Pharm. Biomed. Anal.* **2021,** *192*, 113642.

51.   Ansar, S. M.; Jiang, W.; Mudalige, T., "Direct quantification of unencapsulated doxorubicin in liposomal doxorubicin formulations using capillary electrophoresis." *Int. J. Pharm.* **2018,** *549*, (1), 109-114.

52.   Franzen, U.; Østergaard, J., "Physico-chemical characterization of liposomes and drug substance–liposome interactions in pharmaceutics using capillary electrophoresis and electrokinetic chromatography." *J. Chromatogr. A* **2012,** *1267*, 32-44.

53.   Griese, N.; Blaschke, G.; Boos, J.; Hempel, G., "Determination of free and liposome-associated daunorubicin and daunorubicinol in plasma by capillary electrophoresis." *J. Chromatogr. A* **2002,** *979*, (1), 379-388.

54.   Quattrini, F.; Berrecoso, G.; Crecente-Campo, J.; Alonso, M. J., "Asymmetric flow field-flow fractionation as a multifunctional technique for the characterization of polymeric nanocarriers." *Drug Deliv. Transl. Res.* **2021**.

55.   Caputo, F.; Mehn, D.; Clogston, J. D.; Rösslein, M.; Prina-Mello, A.; Borgos, S. E.; Gioria, S.; Calzolai, L., "Asymmetric-flow field-flow fractionation for measuring particle size, drug loading and (in)stability of nanopharmaceuticals. The joint view of European Union Nanomedicine Characterization Laboratory and National Cancer Institute - Nanotechnology Characterization Laboratory." *J. Chromatogr. A* **2021,** *1635*, 461767.

56.   Hu, Y.; Crist, R. M.; Clogston, J. D., "The utility of asymmetric flow field-flow fractionation for preclinical characterization of nanomedicines." *Anal. Bioanal. Chem.* **2020,** *412*, 425-438.

57.   Ansar, S. M.; Mudalige, T., "Characterization of doxorubicin liposomal formulations for size-based distribution of drug and excipients using asymmetric-flow field-flow fractionation (AF4) and liquid chromatography-mass spectrometry (LC-MS)." *Int. J. Pharm.* **2020,** *574*, 118906.

58.   Hu, Y.; Crist, R. M.; Clogston, J. D., "The utility of asymmetric flow field-flow fractionation for preclinical characterization of nanomedicines." *Anal. Bioanal. Chem.* **2019**, 1-14.

59.   Hinna, A.; Steiniger, F.; Hupfeld, S.; Brandl, M.; Kuntsche, J., "Asymmetrical flow field-flow fractionation with on-line detection for drug transfer studies: A feasibility study." *Anal. Bioanal. Chem.* **2014,** *406*, (30), 7827-7839.

60.   Fraunhofer, W.; Winter, G.; Coester, C., "Asymmetrical flow field-flow fractionation and multiangle light scattering for analysis of gelatin nanoparticle drug carrier systems." *Anal. Biochem.* **2004,** *76*, (7), 1909-1920.

61.   Hinna, A. H.; Hupfeld, S.; Kuntsche, J.; Brandl, M., "The use of asymmetrical flow field-flow fractionation with on-line detection in the study of drug retention within liposomal nanocarriers and drug transfer kinetics." *J. pharm. biomed. anal.* **2016,** *124*, 157-163.

62.   Hinna, A. H.; Hupfeld, S.; Kuntsche, J.; Bauer-Brandl, A.; Brandl, M., "Mechanism and kinetics of the loss of poorly soluble drugs from liposomal carriers studied by a novel flow field-flow fractionation-based drug release−/transfer-assay." *J. Controlled Release* **2016,** *232*, 228-237.

63.   Wankar, J.; Bonvicini, F.; Benkovics, G.; Marassi, V.; Malanga, M.; Fenyvesi, E.; Gentilomi, G. A.; Reschiglian, P.; Roda, B.; Manet, I., "Widening the Therapeutic

Perspectives of Clofazimine by Its Loading in Sulfobutylether β-Cyclodextrin Nanocarriers: Nanomolar IC50 Values against MDR S. epidermidis." *Mol. Pharmaceutics* **2018,** *15*, (9), 3823-3836.

64.   Hupfeld, S.; Ausbacher, D.; Brandl, M., "Asymmetric flow field-flow fractionation of liposomes: 2. Concentration detection and adsorptive loss phenomena." *J. Sep. Sci.* **2009,** *32*, (20), 3555-3561.

65.   Iavicoli, P.; Urbán, P.; Bella, A.; Ryadnov, M. G.; Rossi, F.; Calzolai, L., "Application of asymmetric flow field-flow fractionation hyphenations for liposome–antimicrobial peptide interaction." *J. Chromatogr. A* **2015,** *1422*, 260-269.

66.   de Oliveira, M. A.; Pound-Lana, G.; Capelari-Oliveira, P.; Pontífice, T. G.; Silva, S. E. D.; Machado, M. G. C.; Postacchini, B. B.; Mosqueira, V. C. F., "Release, transfer and partition of fluorescent dyes from polymeric nanocarriers to serum proteins monitored by asymmetric flow field-flow fractionation." *J. Chromatogr. A* **2021,** *1641*, 461959.

67.   Pound-Lana, G. E. N.; Garcia, G. M.; Trindade, I. C.; Capelari-Oliveira, P.; Pontifice, T. G.; Vilela, J. M. C.; Andrade, M. S.; Nottelet, B.; Postacchini, B. B.; Mosqueira, V. C. F., "Phthalocyanine photosensitizer in polyethylene glycol-block-poly(lactide-co-benzyl glycidyl ether) nanocarriers: Probing the contribution of aromatic donor-acceptor interactions in polymeric nanospheres." *Mater. Sci. Eng. C* **2019,** *94*, 220-233.

68.   Smith, M. H.; South, A. B.; Gaulding, J. C.; Lyon, L. A., "Monitoring the Erosion of Hydrolytically-Degradable Nanogels via Multiangle Light Scattering

Coupled to Asymmetrical Flow Field-Flow Fractionation." *Anal. Biochem.* **2010,** *82*, (2), 523-530.

69.   Shimoda, A.; Sawada, S.-i.; Kano, A.; Maruyama, A.; Moquin, A.; Winnik, F. M.; Akiyoshi, K., "Dual crosslinked hydrogel nanoparticles by nanogel bottom-up method for sustained-release delivery." *Colloids Surf., B* **2012,** *99*, 38-44.

70.   Gaulding, J. C.; South, A. B.; Lyon, L. A., "Hydrolytically degradable shells on thermoresponsive microgels." *Colloid. Polym. Sci.* **2013,** *291*, (1), 99-107.

71.   Kang, D. Y.; Kim, M. J.; Kim, S. T.; Oh, K. S.; Yuk, S. H.; Lee, S., "Size characterization of drug-loaded polymeric core/shell nanoparticles using asymmetrical flow field-flow fractionation." *Anal. Bioanal. Chem.* **2008,** *390*, (8), 2183-2188.

72.   Shakiba, S.; Hakimian, A.; Barco, L. R.; Louie, S. M., "Dynamic Intermolecular Interactions Control Adsorption from Mixtures of Natural Organic Matter and Protein onto Titanium Dioxide Nanoparticles." *Environ. Sci. Technol.* **2018,** *52*, (24), 14158-14168.

73.   Ju-Nam, Y.; Lead, J. R., "Manufactured nanoparticles: An overview of their chemistry, interactions and potential environmental implications." *Sci. Total Environ.* **2008,** *400*, (1), 396-414.

74.   Dwivedi, A. D.; Dubey, S. P.; Sillanpää, M.; Kwon, Y.-N.; Lee, C.; Varma, R. S., "Fate of engineered nanoparticles: implications in the environment." *Coord. Chem. Rev.* **2015,** *287*, 64-78.

75.   Wiesner, M. R.; Lowry, G. V.; Alvarez, P.; Dionysiou, D.; Biswas, P., "Assessing the risks of manufactured nanomaterials." *Environ. Sci. Technol.* **2006,** *40*, (14), 4336-4345.

76.	Philippe, A.; Schaumann, G. E., "Interactions of dissolved organic matter with natural and engineered inorganic colloids: a review." *Environ. Sci. Technol.* **2014,** *48*, (16), 8946-62.

77.	Grillo, R.; Rosa, A. H.; Fraceto, L. F., "Engineered nanoparticles and organic matter: a review of the state-of-the-art." *Chemosphere* **2015,** *119*, 608-619.

78.	Levard, C.; Hotze, E. M.; Lowry, G. V.; Brown Jr, G. E., "Environmental transformations of silver nanoparticles: impact on stability and toxicity." *Environ. Sci. Technol.* **2012,** *46*, (13), 6900-6914.

79.	Diegoli, S.; Manciulea, A. L.; Begum, S.; Jones, I. P.; Lead, J. R.; Preece, J. A., "Interaction between manufactured gold nanoparticles and naturally occurring organic macromolecules." *Sci. Total Environ.* **2008,** *402*, (1), 51-61.

80.	Surette, M. C.; Nason, J. A., "Effects of surface coating character and interactions with natural organic matter on the colloidal stability of gold nanoparticles." *Environ. Sci. Nano* **2016,** *3*, (5), 1144-1152.

81.	Petosa, A. R.; Jaisi, D. P.; Quevedo, I. R.; Elimelech, M.; Tufenkji, N., "Aggregation and deposition of engineered nanomaterials in aquatic environments: Role of physicochemical interactions." *Environ. Sci. Technol.* **2010,** *44*, (17), 6532-6549.

82.	Lin, S.; Mortimer, M.; Chen, R.; Kakinen, A.; Riviere, J. E.; Davis, T. P.; Ding, F.; Ke, P. C., "NanoEHS beyond toxicity – focusing on biocorona." *Environ. Sci. Nano* **2017,** *4*, (7), 1433-1454.

83.	Lynch, I.; Cedervall, T.; Lundqvist, M.; Cabaleiro-Lago, C.; Linse, S.; Dawson, K. A., "The nanoparticle-protein complex as a biological entity; a complex fluids and

surface science challenge for the 21st century." *Adv. Colloid Interface Sci.* **2007,** *134-135*, 167-74.

84.   Moghimi, S. M.; Hunter, A. C.; Andresen, T. L., "Factors controlling nanoparticle pharmacokinetics: an integrated analysis and perspective." *Annu. Rev. Pharmacol. Toxicol.* **2012,** *52*, 481-503.

85.   Monopoli, M. P.; Aberg, C.; Salvati, A.; Dawson, K. A., "Biomolecular coronas provide the biological identity of nanosized materials." *Nat. Nanotechnol.* **2012,** *7*, (12), 779-86.

86.   Nel, A. E.; Madler, L.; Velegol, D.; Xia, T.; Hoek, E. M.; Somasundaran, P.; Klaessig, F.; Castranova, V.; Thompson, M., "Understanding biophysicochemical interactions at the nano-bio interface." *Nat. Mater.* **2009,** *8*, (7), 543-57.

87.   Walkey, C. D.; Chan, W. C., "Understanding and controlling the interaction of nanomaterials with proteins in a physiological environment." *Chem. Soc. Rev.* **2012,** *41*, (7), 2780-99.

88.   Li, Z.; Lowry, G. V.; Fan, J.; Liu, F.; Chen, J., "High molecular weight components of natural organic matter preferentially adsorb onto nanoscale zero valent iron and magnetite." *Sci. Total Environ.* **2018,** *628-629*, 177-185.

89.   Deonarine, A.; Lau, B. L.; Aiken, G. R.; Ryan, J. N.; Hsu-Kim, H., "Effects of humic substances on precipitation and aggregation of zinc sulfide nanoparticles." *Environ. Sci. Technol.* **2011,** *45*, (8), 3217-23.

90.   Hyung, H.; Kim, J.-H., "Natural organic matter (NOM) adsorption to multi-walled carbon nanotubes: effect of NOM characteristics and water quality parameters." *Environ. Sci. Technol.* **2008,** *42*, (12), 4416-4421.

91.   Baalousha, M.; Afshinnia, K.; Guo, L., "Natural organic matter composition determines the molecular nature of silver nanomaterial-NOM corona." *Environ. Sci. Nano* **2018,** *5*, (4), 868-881.

92.   Kang, S. H.; Xing, B. S., "Humic acid fractionation upon sequential adsorption onto goethite." *Langmuir* **2008,** *24*, (6), 2525-2531.

93.   Phong, D. D.; Hur, J., "Using two-dimensional correlation size exclusion chromatography (2D-CoSEC) and EEM-PARAFAC to explore the heterogeneous adsorption behavior of humic substances on nanoparticles with respect to molecular sizes." *Environ. Sci. Technol.* **2018,** *52*, (2), 427-435.

94.   Yang, K.; Lin, D.; Xing, B., "Interactions of humic acid with nanosized inorganic oxides." *Langmuir* **2009,** *25*, (6), 3571-3576.

95.   Carbonaro, S.; Sugihara, M. N.; Strathmann, T. J., "Continuous-flow photocatalytic treatment of pharmaceutical micropollutants: Activity, inhibition, and deactivation of TiO_2 photocatalysts in wastewater effluent." *Appl. Catal., B* **2013,** *129*, 1-12.

96.   Tan, W.; Peralta-Videa, J. R.; Gardea-Torresdey, J. L., "Interaction of titanium dioxide nanoparticles with soil components and plants: current knowledge and future research needs – a critical review." *Environ. Sci. Nano* **2018,** *5*, (2), 257-278.

97.   Menard, A.; Drobne, D.; Jemec, A., "Ecotoxicity of nanosized TiO_2. Review of in vivo data." *Environ. Pollut.* **2011,** *159*, (3), 677-84.

98.   Curry, D. E.; Andrea, K. A.; Carrier, A. J.; Nganou, C.; Scheller, H.; Yang, D.; Youden, B.; Zhang, Y.; Nicholson, A.; Cui, S., "Surface interaction of doxorubicin with anatase determines its photodegradation mechanism: insights into removal of

waterborne pharmaceuticals by TiO$_2$ nanoparticles." *Environ. Sci. Nano* **2018,** *5*, (4), 1027-1035.

99.   He, X.; Sanders, S.; Aker, W. G.; Lin, Y.; Douglas, J.; Hwang, H. M., "Assessing the effects of surface-bound humic acid on the phototoxicity of anatase and rutile TiO$_2$ nanoparticles *in vitro*." *J. Environ. Sci. (China)* **2016,** *42*, 50-60.

100.   Li, Y.; Niu, J.; Shang, E.; Crittenden, J. C., "Influence of dissolved organic matter on photogenerated reactive oxygen species and metal-oxide nanoparticle toxicity." *Water Res.* **2016,** *98*, 9-18.

101.   Gao, X.; Zhou, K.; Zhang, L.; Yang, K.; Lin, D., "Distinct effects of soluble and bound exopolymeric substances on algal bioaccumulation and toxicity of anatase and rutile TiO$_2$ nanoparticles." *Environ. Sci. Nano* **2018,** *5*, (3), 720-729.

102.   Kim, J.; Shan, W.; Davies, S. H.; Baumann, M. J.; Masten, S. J.; Tarabara, V. V., "Interactions of aqueous NOM with nanoscale TiO$_2$: Implications for ceramic membrane filtration-ozonation hybrid process." *Environ. Sci. Technol.* **2009,** *43*, (14), 5488-5494.

103.   Chen, G.; Liu, X.; Su, C., "Distinct effects of humic acid on transport and retention of TiO$_2$ rutile nanoparticles in saturated sand columns." *Environ. Sci. Technol.* **2012,** *46*, (13), 7142-7150.

104.   Hotze, E. M.; Louie, S. M.; Lin, S.; Wiesner, M. R.; Lowry, G. V., "Nanoparticle core properties affect attachment of macromolecule-coated nanoparticles to silica surfaces." *Environ. Chem.* **2014,** *11*, (3), 257-267.

105.   Bouhekka, A.; Bürgi, T., "In situ ATR-IR spectroscopy study of adsorbed protein: Visible light denaturation of bovine serum albumin on TiO$_2$." *Appl. Surf. Sci.* **2012,** *261*, 369-374.

106.   Kopac, T.; Bozgeyik, K.; Yener, J., "Effect of pH and temperature on the adsorption of bovine serum albumin onto titanium dioxide." *Colloids Surf., A* **2008,** *322*, (1-3), 19-28.

107.   Givens, B. E.; Xu, Z.; Fiegel, J.; Grassian, V. H., "Bovine serum albumin adsorption on SiO$_2$ and TiO$_2$ nanoparticle surfaces at circumneutral and acidic pH: A tale of two nano-bio surface interactions." *J. Colloid Interface Sci.* **2017,** *493*, 334-341.

108.   Kleber, M.; Sollins, P.; Sutton, R., "A conceptual model of organo-mineral interactions in soils: self-assembly of organic molecular fragments into zonal structures on mineral surfaces." *Biogeochemistry* **2007,** *85*, (1), 9-24.

109.   Pucci, A.; Paolo D'Acqui, L.; Calamai, L., "Fate of prions in soil: interactions of RecPrP with organic matter of soil aggregates as revealed by LTA-PAS." *Environ. Sci. Technol.* **2008,** *42*, (3), 728-733.

110.   Tan, W.; Norde, W.; Koopal, L. K., "Interaction between lysozyme and humic acid in layer-by-layer assemblies: Effects of pH and ionic strength." *J. Colloid Interface Sci.* **2014,** *430*, 40-46.

111.   Sander, M.; Tomaszewski, J. E.; Madliger, M.; Schwarzenbach, R. P., "Adsorption of insecticidal Cry1Ab protein to humic substances. 1. Experimental approach and mechanistic aspects." *Environ. Sci. Technol.* **2012,** *46*, (18), 9923-9931.

112.   Schmidt, M. P.; Martinez, C. E., "Supramolecular association impacts biomolecule adsorption onto goethite." *Environ. Sci. Technol.* **2018,** *52*, (7), 4079-4089.

113.   Quiquampoix, H.; Burns, R. G., "Interactions between proteins and soil mineral surfaces: environmental and health consequences." *Elements* **2007,** *3*, (6), 401-406.

114.   Tan, W. F.; Koopal, L. K.; Weng, L. P.; van Riemsdijk, W. H.; Norde, W., "Humic acid protein complexation." *Geochim. Cosmochim. Acta* **2008,** *72*, (8), 2090-2099.

115.   Li, Y.; Tan, W.; Koopal, L. K.; Wang, M.; Liu, F.; Norde, W., "Influence of soil humic and fulvic acid on the activity and stability of lysozyme and urease." *Environ. Sci. Technol.* **2013,** *47*, (10), 5050-5056.

116.   Giachin, G.; Narkiewicz, J.; Scaini, D.; Ngoc, A. T.; Margon, A.; Sequi, P.; Leita, L.; Legname, G., "Prion protein interaction with soil humic substances: environmental implications." *PloS one* **2014,** *9*, (6), e100016.

117.   Tomaszewski, J. E.; Schwarzenbach, R. P.; Sander, M., "Protein encapsulation by humic substances." *Environ. Sci. Technol.* **2011,** *45*, (14), 6003-6010.

118.   Tan, W. F.; Koopal, L. K.; Norde, W., "Interaction between humic acid and lysozyme, studied by dynamic light scattering and isothermal titration calorimetry." *Environ. Sci. Technol.* **2009,** *43*, (3), 591-596.

119.   Smith, C. B.; Booth, C. J.; Wadzinski, T. J.; Legname, G.; Chappell, R.; Johnson, C. J.; Pedersen, J. A., "Humic substances interfere with detection of pathogenic prion protein." *Soil Biol. Biochem.* **2014,** *68*, 309-316.

120.   Hirsh, S. L.; McKenzie, D. R.; Nosworthy, N. J.; Denman, J. A.; Sezerman, O. U.; Bilek, M. M., "The Vroman effect: competitive protein exchange with dynamic multilayer protein aggregates." *Colloids Surf., B* **2013,** *103*, 395-404.

121.   Tsai, D. H.; Davila-Morris, M.; DelRio, F. W.; Guha, S.; Zachariah, M. R.; Hackley, V. A., "Quantitative determination of competitive molecular adsorption on gold nanoparticles using attenuated total reflectance-Fourier transform infrared spectroscopy." *Langmuir* **2011,** *27*, (15), 9302-13.

122.   Tsai, D. H.; Shelton, M. P.; DelRio, F. W.; Elzey, S.; Guha, S.; Zachariah, M. R.; Hackley, V. A., "Quantifying dithiothreitol displacement of functional ligands from gold nanoparticles." *Anal. Bioanal. Chem.* **2012,** *404*, (10), 3015-23.

123.   U.S. Environmental Protection Agency (EPA). *Methods for measuring the acute toxicity of effluents and receiving waters to freshwater and marine organisms*;Washington, DC, 2002.

124.   Keller, A. A.; Wang, H.; Zhou, D.; Lenihan, H. S.; Cherr, G.; Cardinale, B. J.; Miller, R.; Ji, Z., "Stability and aggregation of metal oxide nanoparticles in natural aqueous matrices." *Environ. Sci. Technol.* **2010,** *44*, (6), 1962-1967.

125.   Taurozzi, J. S.; Hackley, V. A.; Wiesner, M., "Preparation of nanoparticle dispersions from powdered material using ultrasonic disruption." *NIST Special Publication 1200* **2012**, (2), 1200-2.

126.   National Institute of Standards and Technology (NIST). *Certificate of Analysis: SRM 1898 - Titanium dioxide nanomaterial*; Gaithersburg, MD, 2012.

127.   Louie, S. M.; Spielman-Sun, E. R.; Small, M. J.; Tilton, R. D.; Lowry, G. V., "Correlation of the physicochemical properties of natural organic matter samples from different sources to their effects on gold nanoparticle aggregation in monovalent electrolyte." *Environ. Sci. Technol.* **2015,** *49*, (4), 2188-2198.

128.   Louie, S. M.; Tilton, R. D.; Lowry, G. V., "Effects of molecular weight distribution and chemical properties of natural organic matter on gold nanoparticle aggregation." *Environ. Sci. Technol.* **2013,** *47*, (9), 4245-4254.

129.   Roy, A. S.; Tripathy, D. R.; Chatterjee, A.; Dasgupta, S., "A spectroscopic study of the interaction of the antioxidant naringin with bovine serum albumin." *J. Biophys. Chem.* **2010,** *1*, (03), 141.

130.   Hammond, J. B.; Kruger, N. J., The Bradford method for protein quantitation. In *New Protein Techniques*, Humana Press: Clifton, NJ, 1988; pp 25-32.

131.   Whiffen, L. K.; Midgley, D. J.; McGee, P. A., "Polyphenolic compounds interfere with quantification of protein in soil extracts using the Bradford method." *Soil Biol. Biochem.* **2007,** *39*, (2), 691-694.

132.   Bricaud, A.; Morel, A.; Prieur, L., "Absorption by dissolved organic matter of the sea (yellow substance) in the UV and visible domains 1." *Limnol. Oceanogr.* **1981,** *26*, (1), 43-53.

133.   Korshin, G.; Chow, C. W.; Fabris, R.; Drikas, M., "Absorbance spectroscopy-based examination of effects of coagulation on the reactivity of fractions of natural organic matter with varying apparent molecular weights." *Water Res.* **2009,** *43*, (6), 1541-1548.

134.   Korshin, G. V.; Li, C.-W.; Benjamin, M. M., "Monitoring the properties of natural organic matter through UV spectroscopy: A consistent theory." *Water Res.* **1997,** *31*, (7), 1787-1795.

135.   Yan, M.; Korshin, G.; Wang, D.; Cai, Z., "Characterization of dissolved organic matter using high-performance liquid chromatography (HPLC)–size exclusion

chromatography (SEC) with a multiple wavelength absorbance detector." *Chemosphere* **2012,** *87*, (8), 879-885.

136.   Xu, Z.; Grassian, V. H., "Bovine serum albumin adsorption on TiO_2 nanoparticle surfaces: Effects of pH and coadsorption of phosphate on protein–surface interactions and protein structure." *J. Phys. Chem. C* **2017,** *121*, (39), 21763-21771.

137.   Bellamy, M. K., "Using FTIR-ATR spectroscopy to teach the internal standard method." *J. Chem. Educ.* **2010,** *87*, (12), 1399-1401.

138.   Taurozzi, J. S.; Hackley, V. A.; Wiesner, M. R., "A standardised approach for the dispersion of titanium dioxide nanoparticles in biological media." *Nanotoxicology* **2013,** *7*, (4), 389-401.

139.   Lee, W.-K.; Ko, J.-S.; Kim, H.-M., "Effect of electrostatic interaction on the adsorption of globular proteins on octacalcium phosphate crystal film." *J. Colloid Interface Sci.* **2002,** *246*, (1), 70-77.

140.   Loosli, F.; Le Coustumer, P.; Stoll, S., "TiO_2 nanoparticles aggregation and disaggregation in presence of alginate and Suwannee River humic acids. pH and concentration effects on nanoparticle stability." *Water Res.* **2013,** *47*, (16), 6052-6063.

141.   Li, Y.; Yang, C.; Guo, X.; Dang, Z.; Li, X.; Zhang, Q., "Effects of humic acids on the aggregation and sorption of nano-TiO_2." *Chemosphere* **2015,** *119*, 171-176.

142.   Kawahigashi, M.; Kaiser, K.; Kalbitz, K.; Rodionov, A.; Guggenberger, G., "Dissolved organic matter in small streams along a gradient from discontinuous to continuous permafrost." *Global Change Biol.* **2004,** *10*, (9), 1576-1586.

143.   Westgate, P. J.; Park, C., "Evaluation of proteins and organic nitrogen in wastewater treatment effluents." *Environ. Sci. Technol.* **2010,** *44*, (14), 5352-5357.

144.   Aitkenhead-Peterson, J.; Steele, M.; Nahar, N.; Santhy, K., "Dissolved organic carbon and nitrogen in urban and rural watersheds of south-central Texas: land use and land management influences." *Biogeochemistry* **2009,** *96*, (1-3), 119-129.

145.   Sui, X.; Wu, Z.; Lin, C.; Zhou, S., "Terrestrially derived glomalin-related soil protein quality as a potential ecological indicator in a peri-urban watershed." *Environ. Monit. Assess.* **2017,** *189*, (7), 315.

146.   Giacomelli, C. E.; Avena, M. J.; De Pauli, C. P., "Adsorption of bovine serum albumin onto TiO_2 particles." *J. Colloid Interface Sci.* **1997,** *188*, (2), 387-395.

147.   Kim, J.; Shan, W.; Davies, S. H. R.; Baumann, M. J.; Masten, S. J.; Tarabara, V. V., "Interactions of aqueous NOM with nanoscale TiO_2: Implications for ceramic membrane filtration-ozonation hybrid process." *Environ. Sci. Technol.* **2009,** *43*, (14), 5488-5494.

148.   Ellingsen, J. E., "A study on the mechanism of protein adsorption to TiO_2." *Biomaterials* **1991,** *12*, (6), 593-596.

149.   Klinger, A.; Steinberg, D.; Kohavi, D.; Sela, M. N., "Mechanism of adsorption of human albumin to titanium in vitro." *J. Biomed. Mater. Res.* **1998,** *36*, (3), 387-392.

150.   Wassell, D. T. H.; Embery, G., "Adsorption of bovine serum albumin on to titanium powder." *Biomaterials* **1996,** *17*, (9), 859-864.

151.   Senesi, N.; Miano, T.; Provenzano, M.; Brunetti, G., "Spectroscopic and compositional comparative characterization of IHSS reference and standard fulvic and humic acids of various origin." *Sci. Total Environ.* **1989,** *81*, 143-156.

152.   Croue, J.-P.; Korshin, G. V.; Benjamin, M. M., *Characterization of natural organic matter in drinking water*. <u>American Water Works Association</u>: 2000.

153.   Rouquerol, J.; Rouquerol, F.; Sing, K. S.; Llewellyn, P.; Maurin, G., *Adsorption by powders and porous solids: Principles, methodology and applications*. 2nd ed.; Academic Press: Amsterdam, The Netherlands, 2012.

154.   Evans, J. W., "Random and cooperative sequential adsorption." *Rev. Mod. Phys.* **1993,** *65*, (4), 1281-1329.

155.   Rabe, M.; Verdes, D.; Seeger, S., "Understanding protein adsorption phenomena at solid surfaces." *Adv. Colloid Interface Sci.* **2011,** *162*, (1-2), 87-106.

156.   Johnson, P. R.; Elimelech, M., "Dynamics of colloid deposition in porous media: Blocking based on random sequential adsorption." *Langmuir* **1995,** *11*, (3), 801-812.

157.   Hiemenz, P. C.; Rajagopalan, R., *Principles of colloid and surface chemistry*. 3rd ed.; CRC Press: Boca Raton, FL, 1997.

158.   Van Tassel, P. R.; Guemouri, L. l.; Ramsden, J. J.; Tarjus, G.; Viot, P.; Talbot, J., "A particle-level model of irreversible protein adsorption with a postadsorption transition." *J. Colloid Interface Sci.* **1998,** *207*, (2), 317-323.

159.   Van Tassel, P. R.; Viot, P.; Tarjus, G.; Talbot, J., "Irreversible adsorption of macromolecules at a liquid–solid interface: Theoretical studies of the effects of conformational change." *J. Chem. Phys.* **1994,** *101*, (8), 7064-7073.

160.   Ramsden, J. J., "Puzzles and paradoxes in protein adsorption." *Chem. Soc. Rev.* **1995,** *24*, (1), 73-78.

161.   Mudunkotuwa, I. A.; Al Minshid, A.; Grassian, V. H., "ATR-FTIR spectroscopy as a tool to probe surface adsorption on nanoparticles at the liquid–solid interface in environmentally and biologically relevant media." *Analyst* **2014,** *139*, (5), 870-881.

162.   Adeleye, A. S.; Keller, A. A., "Interactions between algal extracellular polymeric substances and commercial TiO$_2$ nanoparticles in aqueous media." *Environ. Sci. Technol.* **2016,** *50*, (22), 12258-12265.

163.   Hase, M.; Scheffelmaier, R.; Hayden, S.; Rivera, D., "Quantitative *in situ* attenuated total internal reflection Fourier transform infrared study of the isotherms of poly (sodium 4-styrene sulfonate) adsorption to a TiO$_2$ surface over a range of cetylpyridinium bromide monohydrate concentration." *Langmuir* **2010,** *26*, (8), 5534-5543.

164.   Mudunkotuwa, I. A.; Grassian, V. H., "Citric acid adsorption on TiO$_2$ nanoparticles in aqueous suspensions at acidic and circumneutral pH: surface coverage, surface speciation, and its impact on nanoparticle− nanoparticle interactions." *J. Am. Chem. Soc.* **2010,** *132*, (42), 14986-14994.

165.   Pettibone, J. M.; Cwiertny, D. M.; Scherer, M.; Grassian, V. H., "Adsorption of organic acids on TiO$_2$ nanoparticles: effects of pH, nanoparticle size, and nanoparticle aggregation." *Langmuir* **2008,** *24*, (13), 6659-6667.

166.   Liang, L.; Luo, L.; Zhang, S., "Adsorption and desorption of humic and fulvic acids on SiO$_2$ particles at nano-and micro-scales." *Colloids Surf., A* **2011,** *384*, (1-3), 126-130.

167.   Das, K.; Kundu, S., "Adsorption and conformation variation of BSA protein with the size variation of the metallic nanoparticles in LB film." *Colloids Surf., A* **2015,** *468*, 56-61.

168.   Jeyachandran, Y.; Mielczarski, E.; Rai, B.; Mielczarski, J., "Quantitative and qualitative evaluation of adsorption/desorption of bovine serum albumin on hydrophilic and hydrophobic surfaces." *Langmuir* **2009,** *25*, (19), 11614-11620.

169.   Max, J.-J.; Chapados, C., "Infrared spectroscopy of aqueous carboxylic acids: comparison between different acids and their salts." *J. Phys. Chem. A* **2004,** *108*, (16), 3324-3337.

170.   Francioso, O.; Sanchez-Cortes, S.; Tugnoli, V.; Ciavatta, C.; Sitti, L.; Gessa, C., "Infrared, Raman, and nuclear magnetic resonance (^{1}H, ^{13}C, and ^{31}P) spectroscopy in the study of fractions of peat humic acids." *Appl. Spectrosc.* **1996,** *50*, (9), 1165-1174.

171.   Mudunkotuwa, I. A.; Grassian, V. H., "Biological and environmental media control oxide nanoparticle surface composition: the roles of biological components (proteins and amino acids), inorganic oxyanions and humic acid." *Environ. Sci. Nano* **2015,** *2*, (5), 429-439.

172.   Tsai, D.-H.; DelRio, F. W.; Keene, A. M.; Tyner, K. M.; MacCuspie, R. I.; Cho, T. J.; Zachariah, M. R.; Hackley, V. A., "Adsorption and conformation of serum albumin protein on gold nanoparticles investigated using dimensional measurements and *in situ* spectroscopic methods." *Langmuir* **2011,** *27*, (6), 2464-2477.

173.   Chittur, K. K., "FTIR/ATR for protein adsorption to biomaterial surfaces." *Biomaterials* **1998,** *19*, (4-5), 357-369.

174.   Wang, Z.; Cao, J.; Meng, F., "Interactions between protein-like and humic-like components in dissolved organic matter revealed by fluorescence quenching." *Water Res.* **2015,** *68*, 404-413.

175.   Phenrat, T.; Song, J. E.; Cisneros, C. M.; Schoenfelder, D. P.; Tilton, R. D.; Lowry, G. V., "Estimating attachment of nano- and submicrometer-particles coated with organic macromolecules in porous media: Development of an empirical model." *Environ. Sci. Technol.* **2010,** *44*, (12), 4531-4538.

176.   Louie, S. M.; Gorham, J. M.; McGivney, E. A.; Liu, J. Y.; Gregory, K. B.; Hackley, V. A., "Photochemical transformations of thiolated polyethylene glycol coatings on gold nanoparticles." *Environ. Sci. Nano* **2016,** *3*, (5), 1090-1102.

177.   Louie, S. M.; Gorham, J. M.; Tan, J. J.; Hackley, V. A., "Ultraviolet photo-oxidation of polyvinylpyrrolidone (PVP) coatings on gold nanoparticles." *Environ. Sci. Nano* **2017,** *4*, (9), 1866-1875.

178.   Nguyen, M. L.; Murphy, J. A.; Hamlet, L. C.; Lau, B. L. T., "Ligand-dependent Ag_2S formation: changes in deposition of silver nanoparticles with sulfidation." *Environ. Sci. Nano* **2018,** *5*, (5), 1090-1095.

179.   George, A.; Shah, P. A.; Shrivastav, P. S., "Natural biodegradable polymers based nano-formulations for drug delivery: A review." *Int. J. Pharm.* **2019,** *561*, 244-264.

180.   Pillay, V.; Seedat, A.; Choonara, Y. E.; du Toit, L. C.; Kumar, P.; Ndesendo, V. M. K., "A review of polymeric refabrication techniques to modify polymer properties for biomedical and drug delivery applications." *AAPS Pharmscitech* **2013,** *14*, (2), 692-711.

181.   Godwin, A.; Bolina, K.; Clochard, M.; Dinand, E.; Rankin, S.; Simic, S.; Brocchini, S., "New strategies for polymer development in pharmaceutical science—a short review." *J. Pharm. Pharmacol.* **2001,** *53*, (9), 1175-1184.

182. Xu, Y.; Kim, C.-S.; Saylor, D. M.; Koo, D., "Polymer degradation and drug delivery in PLGA‑based drug–polymer applications: A review of experiments and theories." *J. Biomed. Mater. Res. Part B* **2017,** *105*, (6), 1692-1716.

183. Makadia, H. K.; Siegel, S. J., "Poly lactic-*co*-glycolic acid (PLGA) as biodegradable controlled drug delivery carrier." *Polymers* **2011,** *3*, (3), 1377-1397.

184. Stebbins, N. D.; Ouimet, M. A.; Uhrich, K. E., "Antibiotic-containing polymers for localized, sustained drug delivery." *Adv. Drug Delivery Rev.* **2014,** *78*, 77-87.

185. Gao, P.; Nie, X.; Zou, M.; Shi, Y.; Cheng, G., "Recent advances in materials for extended-release antibiotic delivery system." *J. Antibiot.* **2011,** *64*, (9), 625-634.

186. Paudel, S.; Cerbu, C.; Astete, C. E.; Louie, S. M.; Sabliov, C.; Rodrigues, D. F., "Enrofloxacin-impregnated PLGA nanocarriers for efficient therapeutics and diminished generation of reactive oxygen species." *ACS Appl. Nano Mater.* **2019,** *2*, (8), 5035-5043.

187. US Food and Drug Administration, Drug products, including biological products, that contain nanomaterials-guidance for industry. In 2017.

188. Korsmeyer, R. W.; Peppas, N. A., "Effect of the morphology of hydrophilic polymeric matrices on the diffusion and release of water soluble drugs." *J. Membr. Sci.* **1981,** *9*, (3), 211-227.

189. Liechty, W. B.; Kryscio, D. R.; Slaughter, B. V.; Peppas, N. A., "Polymers for drug delivery systems." *Annu. Rev. Chem. Biomol. Eng.* **2010,** *1*, 149-173.

190. Kamaly, N.; Yameen, B.; Wu, J.; Farokhzad, O. C., "Degradable controlled-release polymers and polymeric nanoparticles: Mechanisms of controlling drug release." *Chem. Rev.* **2016,** *116*, (4), 2602-2663.

191.   Shameem, M.; Lee, H.; DeLuca, P. P., "A short-term (accelerated release) approach to evaluate peptide release from PLGA depot formulations." *AAPS PharmSciTech* **1999,** *1*, (3), 1.

192.   Lappe, S.; Mulac, D.; Langer, K., "Polymeric nanoparticles–Influence of the glass transition temperature on drug release." *Int. J. Pharm.* **2017,** *517*, (1-2), 338-347.

193.   Park, K.; Skidmore, S.; Hadar, J.; Garner, J.; Park, H.; Otte, A.; Soh, B. K.; Yoon, G.; Yu, D.; Yun, Y.; Lee, B. K.; Jiang, X.; Wang, Y., "Injectable, long-acting PLGA formulations: Analyzing PLGA and understanding microparticle formation." *J. Controlled Release* **2019,** *304*, 125-134.

194.   Gigault, J.; Pettibone, J. M.; Schmitt, C.; Hackley, V. A., "Rational strategy for characterization of nanoscale particles by asymmetric-flow field flow fractionation: A tutorial." *Anal. Chim. Acta* **2014,** *809*, 9-24.

195.   Podzimek, S., *Light scattering, size exclusion chromatography and asymmetric flow field flow fractionation: Powerful tools for the characterization of polymers, proteins and nanoparticles*. John Wiley & Sons Inc.: Hoboken, New Jersey, 2011.

196.   Wagner, M.; Holzschuh, S.; Traeger, A.; Fahr, A.; Schubert, U. S., "Asymmetric Flow Field-Flow Fractionation in the Field of Nanomedicine." *Anal. Biochem.* **2014,** *86*, (11), 5201-5210.

197.   Schimpf, M. E.; Caldwell, K.; Giddings, J. C., *Field-flow fractionation handbook*. Wiley-Interscience: New York, 2000.

198.   Wahlund, K. G.; Winegarner, H. S.; Caldwell, K. D.; Giddings, J. C., "Improved flow field-flow fractionation system applied to water-soluble polymers: Programming, outlet stream splitting, and flow optimization." *Anal. Biochem.* **1986,** *58*, (3), 573-578.

199.   Malik, M. I.; Pasch, H., "Field-flow fractionation: New and exciting perspectives in polymer analysis." *Prog. Polym. Sci.* **2016,** *63*, 42-85.

200.   Fraunhofer, W.; Winter, G., "The use of asymmetrical flow field-flow fractionation in pharmaceutics and biopharmaceutics." *Eur. J. Pharm. Biopharm.* **2004,** *58*, (2), 369-383.

201.   Zattoni, A.; Roda, B.; Borghi, F.; Marassi, V.; Reschiglian, P., "Flow field-flow fractionation for the analysis of nanoparticles used in drug delivery." *J. Pharm. Biomed. Anal.* **2014,** *87*, 53-61.

202.   Ehrhart, J.; Mingotaud, A.-F.; Violleau, F., "Asymmetrical flow field-flow fractionation with multi-angle light scattering and quasi elastic light scattering for characterization of poly (ethyleneglycol-b-ε-caprolactone) block copolymer self-assemblies used as drug carriers for photodynamic therapy." *J. Chromatogr. A* **2011,** *1218*, (27), 4249-4256.

203.   Bayart, C.; Jean, E.; Paillagot, M.; Renoud, A.; Raillard, A.; Paladino, J.; Le Borgne, M., "Comparison of SEC and AF4 analytical tools for size estimation of typhoid Vi polysaccharides." *Anal. Methods* **2019,** *11*, (37), 4851-4858.

204.   Caputo, F.; Clogston, J.; Calzolai, L.; Rösslein, M.; Prina-Mello, A., "Measuring particle size distribution of nanoparticle enabled medicinal products, the joint view of EUNCL and NCI-NCL. A step by step approach combining orthogonal measurements with increasing complexity." *J. Controlled Release* **2019,** *299*, 31-43.

205.   Parot, J.; Caputo, F.; Mehn, D.; Hackley, V. A.; Calzolai, L., "Physical characterization of liposomal drug formulations using multi-detector asymmetrical-flow field flow fractionation." *J. Controlled Release* **2020,** *320*, 495-510.

206. Collins, M. E.; Soto-Cantu, E.; Cueto, R.; Russo, P. S., "Separation and characterization of poly(tetrafluoroethylene) latex particles by asymmetric flow field flow fractionation with light-scattering detection." *Langmuir* **2014,** *30*, (12), 3373-3380.

207. Guan, X.; Cueto, R.; Russo, P.; Qi, Y.; Wu, Q., "Asymmetric flow field-flow fractionation with multiangle light scattering detection for characterization of cellulose nanocrystals." *Biomacromolecules* **2012,** *13*, (9), 2671-2679.

208. Zattoni, A.; Rambaldi, D. C.; Reschiglian, P.; Melucci, M.; Krol, S.; Garcia, A. M. C.; Sanz-Medel, A.; Roessner, D.; Johann, C., "Asymmetrical flow field-flow fractionation with multi-angle light scattering detection for the analysis of structured nanoparticles." *J. Chromatogr. A* **2009,** *1216*, (52), 9106-9112.

209. Barber, A.; Kly, S.; Moffitt, M.; Rand, L.; Ranville, J. F., "Coupling single particle ICP-MS with field-flow fractionation for characterizing metal nanoparticles contained in nanoplastic colloids." *Environ. Sci. Nano* **2020,** *7*, 514-524.

210. Bouby, M.; Geckeis, H.; Geyer, F. W., "Application of asymmetric flow field-flow fractionation (AsFlFFF) coupled to inductively coupled plasma mass spectrometry (ICPMS) to the quantitative characterization of natural colloids and synthetic nanoparticles." *Anal. Bioanal. Chem.* **2008,** *392*, (7), 1447-1457.

211. Dubascoux, S.; Le Hécho, I.; Hassellöv, M.; Von Der Kammer, F.; Potin Gautier, M.; Lespes, G., "Field-flow fractionation and inductively coupled plasma mass spectrometer coupling: History, development and applications." *J. Anal. At. Spectrom.* **2010,** *25*, (5), 613-623.

212.   M-M, P.; Siripinyanond, A., "Field-flow fractionation with inductively coupled plasma mass spectrometry: Past, present, and future." *J. Anal. At. Spectrom.* **2014,** *29*, (10), 1739-1752.

213.   Hadri, H. E.; Louie, S. M.; Hackley, V. A., "Assessing the interactions of metal nanoparticles in soil and sediment matrices - a quantitative analytical multi-technique approach." *Environ. Sci. Nano* **2018,** *5*, 203-214.

214.   Meili-Borovinskaya, O.; Meier, F.; Drexel, R.; Baalousha, M.; Flamigni, L.; Hegetschweiler, A.; Kraus, T., "Analysis of complex particle mixtures by asymmetrical flow field-flow fractionation coupled to inductively coupled plasma time-of-flight mass spectrometry." *J. Chromatogr. A* **2021**, 461981.

215.   Hawe, A.; Friess, W.; Sutter, M.; Jiskoot, W., "Online fluorescent dye detection method for the characterization of immunoglobulin G aggregation by size exclusion chromatography and asymmetrical flow field flow fractionation." *Anal. Biochem.* **2008,** *378*, (2), 115-122.

216.   Alftrén, J.; Peñarrieta, J. M.; Bergenståhl, B.; Nilsson, L., "Comparison of molecular and emulsifying properties of gum arabic and mesquite gum using asymmetrical flow field-flow fractionation." *Food Hydrocolloids* **2012,** *26*, (1), 54-62.

217.   Ulmius, M.; Adapa, S.; Önning, G.; Nilsson, L., "Gastrointestinal conditions influence the solution behaviour of cereal β-glucans *in vitro*." *Food Chem.* **2012,** *130*, (3), 536-540.

218.   Anselmo, A. C.; Mitragotri, S., "Nanoparticles in the clinic: An update." *Bioeng. Transl. Med.* **2019,** *4*, (3), e10143.

219. Runyon, J. R.; Ulmius, M.; Nilsson, L., "A perspective on the characterization of colloids and macromolecules using asymmetrical flow field-flow fractionation." *Colloids Surf., A* **2014,** *442*, 25-33.

220. Guéguen, C.; Cuss, C. W., "Characterization of aquatic dissolved organic matter by asymmetrical flow field-flow fractionation coupled to UV–Visible diode array and excitation emission matrix fluorescence." *J. Chromatogr. A* **2011,** *1218*, (27), 4188-4198.

221. Zhou, Z.; Guo, L., "A critical evaluation of an asymmetrical flow field-flow fractionation system for colloidal size characterization of natural organic matter." *J. Chromatogr. A* **2015,** *1399*, 53-64.

222. Baalousha, M.; Stolpe, B.; Lead, J. R., "Flow field-flow fractionation for the analysis and characterization of natural colloids and manufactured nanoparticles in environmental systems: A critical review." *J. Chromatogr. A* **2011,** *1218*, (27), 4078-4103.

223. Lee, S. T.; Yang, B.; Kim, J.-Y.; Park, J.-H.; Moon, M. H., "Combining asymmetrical flow field-flow fractionation with on- and off-line fluorescence detection to examine biodegradation of riverine dissolved and particulate organic matter." *J. Chromatogr. A* **2015,** *1409*, 218-225.

224. Qureshi, R. N.; Kok, W. T., "Application of flow field-flow fractionation for the characterization of macromolecules of biological interest: A review." *Anal. Bioanal. Chem.* **2011,** *399*, (4), 1401-1411.

225. Yohannes, G.; Jussila, M.; Hartonen, K.; Riekkola, M. L., "Asymmetrical flow field-flow fractionation technique for separation and characterization of biopolymers and bioparticles." *J. Chromatogr. A* **2011,** *1218*, (27), 4104-4116.

226. Danhier, F.; Ansorena, E.; Silva, J. M.; Coco, R.; Le Breton, A.; Préat, V., "PLGA-based nanoparticles: An overview of biomedical applications." *J. Controlled Release* **2012,** *161*, (2), 505-522.

227. Seedher, N.; Agarwal, P., "Various solvent systems for solubility enhancement of enrofloxacin." *Indian J. Pharm. Sci.* **2009,** *71*, (1), 82-87.

228. Cárdenas-Youngs, G.-M.; Beltrán, J.-L., "Dissociation Constants and Octanol–Water Partition Equilibria for Several Fluoroquinolones." *J. Chem. Eng. Data* **2015,** *60*, (11), 3327-3332.

229. Astete, C. E.; Sabliov, C. M., "Synthesis and characterization of PLGA nanoparticles." *J. Biomater. Sci. Polym. Ed.* **2006,** *17*, (3), 247-289.

230. D'Souza, S., "A review of *in vitro* drug release test methods for nano-sized dosage forms." *Adv. Pharmaceutics* **2014,** *2014*.

231. Ramos, M.; Aranda, A.; Garcia, E.; Reuvers, T.; Hooghuis, H., "Simple and sensitive determination of five quinolones in food by liquid chromatography with fluorescence detection." *J. Chromatogr. B* **2003,** *789*, (2), 373-381.

232. Kuntsche, J.; Decker, C.; Fahr, A., "Analysis of liposomes using asymmetrical flow field‐flow fractionation: Separation conditions and drug/lipid recovery." *J. Sep. Sci.* **2012,** *35*, (15), 1993-2001.

233.   Holzschuh, S.; Kaeß, K.; Fahr, A.; Decker, C., "Quantitative *in vitro* assessment of liposome stability and drug transfer employing asymmetrical flow field-flow fractionation (AF4)." *Pharm. Res.* **2016,** *33*, (4), 842-855.

234.   Joguparthi, V.; Anderson, B. D., "Liposomal delivery of hydrophobic weak acids: Enhancement of drug retention using a high intraliposomal pH." *J. Pharm. Sci.* **2008,** *97*, (1), 433-454.

235.   Modi, S.; Xiang, T.-X.; Anderson, B. D., "Enhanced active liposomal loading of a poorly soluble ionizable drug using supersaturated drug solutions." *J. controlled release* **2012,** *162*, (2), 330-339.

236.   Modi, S.; Anderson, B. D., "Determination of drug release kinetics from nanoparticles: Overcoming pitfalls of the dynamic dialysis method." *Mol. Pharmaceutics* **2013,** *10*, (8), 3076-3089.

237.   Burchard, W.; Schmidt, M.; Stockmayer, W., "Information on polydispersity and branching from combined quasi-elastic and integrated scattering." *Macromolecules* **1980,** *13*, (5), 1265-1272.

238.   Hombreiro-Pérez, M.; Siepmann, J.; Zinutti, C.; Lamprecht, A.; Ubrich, N.; Hoffman, M.; Bodmeier, R.; Maincent, P., "Non-degradable microparticles containing a hydrophilic and/or a lipophilic drug: preparation, characterization and drug release modeling." *J. Controlled Release* **2003,** *88*, (3), 413-428.

239.   Vergnaud, J.-M., *Controlled drug release of oral dosage forms*. CRC Press: 1993.

240.   Mathurin, J.; Pancani, E.; Deniset-Besseau, A.; Kjoller, K.; Prater, C. B.; Gref, R.; Dazzi, A., "How to unravel the chemical structure and component localization of

individual drug-loaded polymeric nanoparticles by using tapping AFM-IR." *Analyst* **2018,** *143*, (24), 5940-5949.

241.   Machado, M. G. C.; Pound-Lana, G.; de Oliveira, M. A.; Lanna, E. G.; Fialho, M. C. P.; de Brito, A. C. F.; Barboza, A. P. M.; Aguiar-Soares, R. D. d. O.; Mosqueira, V. C. F., "Labeling PLA-PEG nanocarriers with IR780: physical entrapment versus covalent attachment to polylactide." *Drug Deliv. Transl. Res.* **2020,** *10*, (6), 1626-1643.

242.   Trindade, I. C.; Pound-Lana, G.; Pereira, D. G. S.; de Oliveira, L. A. M.; Andrade, M. S.; Vilela, J. M. C.; Postacchini, B. B.; Mosqueira, V. C. F., "Mechanisms of interaction of biodegradable polyester nanocapsules with non-phagocytic cells." *Eur. J. Pharm. Sci.* **2018,** *124*, 89-104.

243.   Hu, Y.; Crist, R. M.; Clogston, J. D., "The utility of asymmetric flow field-flow fractionation for preclinical characterization of nanomedicines." *Anal. Bioanal. Chem.* **2020,** *412*, (2), 425-438.

244.   Williams, S. K. R.; Benincasa, M.-A.; Smith, W. C.; Oliver, J. D., Field-Flow Fractionation in Analysis of Polymers and Rubbers. Encyclopedia of Analytical Chemistry, pp 1-33.

245.   Werner, P.; Münzberg, M.; Hass, R.; Reich, O., "Process analytical approaches for the coil-to-globule transition of poly(N-isopropylacrylamide) in a concentrated aqueous suspension." *Anal. Bioanal. Chem.* **2017,** *409*, (3), 807-819.

246.   Babusca, D.; Benchea, A. C.; Dimitriu, D. G.; Dorohoi, D. O., "Spectral and Quantum Mechanical Characterization of 3-(2-Benzothiazolyl)-7-(Diethylamino) Coumarin (Coumarin 6) in Binary Solution." *Anal. Lett.* **2017,** *50*, (17), 2740-2754.

247. El-Shishtawy, R. M., "Functional Dyes, and Some Hi-Tech Applications." *Int. J. Photoenergy* **2009,** *2009*, 434897.

248. Liu, Y.; Feng, X.; Yu, Y.; Zhao, Q.; Tang, C.; Zhang, J., "A review of bioselenol-specific fluorescent probes: Synthesis, properties, and imaging applications." *Anal. Chim. Acta* **2020,** *1110*, 141-150.

249. Guo, Z.; Park, S.; Yoon, J.; Shin, I., "Recent progress in the development of near-infrared fluorescent probes for bioimaging applications." *Chem. Soc. Rev.* **2014,** *43*, (1), 16-29.

250. Mirza, A. Z.; Siddiqui, F. A., "Nanomedicine and drug delivery: a mini review." *Int. Nano Lett.* **2014,** *4*, (1), 94.

251. Bastiat, G.; Pritz, C. O.; Roider, C.; Fouchet, F.; Lignières, E.; Jesacher, A.; Glueckert, R.; Ritsch-Marte, M.; Schrott-Fischer, A.; Saulnier, P.; Benoit, J.-P., "A new tool to ensure the fluorescent dye labeling stability of nanocarriers: A real challenge for fluorescence imaging." *J. Controlled Release* **2013,** *170*, (3), 334-342.

252. Carneiro, A.; Matos, M. J.; Uriarte, E.; Santana, L., "Trending Topics on Coumarin and Its Derivatives in 2020." *Molecules* **2021,** *26*, (2), 501.

253. Patel, N. R.; Damann, K.; Leonardi, C.; Sabliov, C. M., "Size dependency of PLGA-nanoparticle uptake and antifungal activity against Aspergillus flavus." *Nanomedicine* **2011,** *6*, (8), 1381-1395.

254. Andersson, M.; Wittgren, B.; Wahlund, K.-G., "Accuracy in Multiangle Light Scattering Measurements for Molar Mass and Radius Estimations. Model Calculations and Experiments." *Anal. Biochem.* **2003,** *75*, (16), 4279-4291.

255.

https://www.sigmaaldrich.com/catalog/product/aldrich/719900?lang=en&region=US

(May 5, 2021),

256.   Pietzonka, P.; Rothen-Rutishauser, B.; Langguth, P.; Wunderli-Allenspach, H.;

Walter, E.; Merkle, H. P., "Transfer of Lipophilic Markers from PLGA and Polystyrene

Nanoparticles to Caco-2 Monolayers Mimics Particle Uptake." *Pharm. Res.* **2002,** *19*,

(5), 595-601.

257.   D.J. Nagi, D. A. T. *SEC of poly(vinyl alcohol) using mullti-detection

methods*;Physical Analytical Center Air Products and Chemicals Inc.: Allentown, PA.

258.   Carrillo-Carrion, C.; Bocanegra, A. I.; Arnaiz, B.; Feliu, N.; Zhu, D.; Parak, W.

J., "Triple-Labeling of Polymer-Coated Quantum Dots and Adsorbed Proteins for

Tracing their Fate in Cell Cultures." *ACS Nano* **2019,** *13*, (4), 4631-4639.

259.   Higuchi, T., "Mechanism of sustained-action medication. Theoretical analysis

of rate of release of solid drugs dispersed in solid matrices." *J. Pharm. Sci.* **1963,** *52*,

(12), 1145-1149.

260.   Higuchi, T., "Rate of Release of Medicaments from Ointment Bases Containing

Drugs in Suspension." *J. Pharm. Sci.* **1961,** *50*, (10), 874-875.

261.   Ritger, P. L.; Peppas, N. A., "A simple equation for description of solute release

I. Fickian and non-fickian release from non-swellable devices in the form of slabs,

spheres, cylinders or discs." *J. Controlled Release* **1987,** *5*, (1), 23-36.

262.   Dash, S.; Murthy, P. N.; Nath, L.; Chowdhury, P., "Kinetic modeling on drug

release from controlled drug delivery systems." *Acta Pol. Pharm.* **2010,** *67*, (3), 217-23.

263.   Hixson, A. W.; Crowell, J. H., "Dependence of Reaction Velocity upon surface and Agitation." *Ind. Eng. Chem. Chem.* **1931,** *23*, (8), 923-931.

264.   Katzhendler, I.; Hoffman, A.; Goldberger, A.; Friedman, M., "Modeling of Drug Release from Erodible Tablets." *J. Pharm. Sci.* **1997,** *86*, (1), 110-115.

265.   5 - Mathematical models of drug release. In *Strategies to Modify the Drug Release from Pharmaceutical Systems*, Bruschi, M. L., Ed. <u>Woodhead Publishing</u>: 2015; pp 63-86.

266.   Hattori, Y.; Haruna, Y.; Otsuka, M., "Dissolution process analysis using model-free Noyes–Whitney integral equation." *Colloids Surf., B* **2013,** *102*, 227-231.

267.   Wu, I. Y.; Bala, S.; Škalko-Basnet, N.; di Cagno, M. P., "Interpreting non-linear drug diffusion data: Utilizing Korsmeyer-Peppas model to study drug release from liposomes." *Eur. J. Pharm. Sci.* **2019,** *138*, 105026.

268.   Rowe, R. C.; Sheskey, P.; Quinn, M., *Handbook of pharmaceutical excipients*. <u>Libros Digitales-Pharmaceutical Press</u>: 2009.

269.   Xu, Y.; Koo, D.; Gerstein, E. A.; Kim, C.-S., "Multi-scale modeling of polymer–drug interactions and their impact on the structural evolutions in PLGA-tetracycline films." *Polymer* **2016,** *84*, 121-131.

270.   Corrigan, O. I.; Li, X., "Quantifying drug release from PLGA nanoparticulates." *Eur. J. Pharm. Sci.* **2009,** *37*, (3), 477-485.

271.   Qaddoumi, M. G.; Ueda, H.; Yang, J.; Davda, J.; Labhasetwar, V.; Lee, V. H. L., "The Characteristics and Mechanisms of Uptake of PLGA Nanoparticles in Rabbit Conjunctival Epithelial Cell Layers." *Pharm. Res.* **2004,** *21*, (4), 641-648.

272. Abdolahpur Monikh, F.; Grundschober, N.; Romeijn, S.; Arenas-Lago, D.; Vijver, M. G.; Jiskoot, W.; Peijnenburg, W. J. G. M., "Development of methods for extraction and analytical characterization of carbon-based nanomaterials (nanoplastics and carbon nanotubes) in biological and environmental matrices by asymmetrical flow field-flow fractionation." *Environ. Pollut.* **2019,** *255*, 113304.

273. Jang, M.-H.; Lee, S.; Hwang, Y. S., "Characterization of Silver Nanoparticles under Environmentally Relevant Conditions Using Asymmetrical Flow Field-Flow Fractionation (AF4)." *PloS one* **2015,** *10*, (11), e0143149.

274. Peng, H.; Chen, Y.; Mao, L.; Zhang, X., "Significant changes in the photo-reactivity of TiO2 in the presence of a capped natural dissolved organic matter layer." *Water Res.* **2017,** *110*, 233-240.

275. Behzadi, S.; Serpooshan, V.; Sakhtianchi, R.; Müller, B.; Landfester, K.; Crespy, D.; Mahmoudi, M., "Protein corona change the drug release profile of nanocarriers: The "overlooked" factor at the nanobio interface." *Colloids Surf., B* **2014,** *123*, 143-149.

276. Obst, K.; Yealland, G.; Balzus, B.; Miceli, E.; Dimde, M.; Weise, C.; Eravci, M.; Bodmeier, R.; Haag, R.; Calderón, M.; Charbaji, N.; Hedtrich, S., "Protein Corona Formation on Colloidal Polymeric Nanoparticles and Polymeric Nanogels: Impact on Cellular Uptake, Toxicity, Immunogenicity, and Drug Release Properties." *Biomacromolecules* **2017,** *18*, (6), 1762-1771.

277. Hammond, J. B.; Kruger, N. J., The Bradford method for protein quantitation. In *New Protein Techniques*, Walker, J. M., Ed. Humana Press: Clifton, NJ, 1988; pp 25-32.

278.   Zor, T.; Selinger, Z., "Linearization of the Bradford protein assay increases its sensitivity: theoretical and experimental studies." *Anal. Biochem.* **1996,** *236*, (2), 302-308.

279.   Romanello, M. B.; Fidalgo de Cortalezzi, M. M., "An experimental study on the aggregation of TiO_2 nanoparticles under environmentally relevant conditions." *Water Res.* **2013,** *47*, (12), 3887-3898.

280.   Bolster, C. H.; Hornberger, G. M., "On the use of linearized Langmuir equations." *Soil Sci. Soc. Am. J.* **2007,** *71*, (6), 1796-1806.

281.   Axelsson, I., "Characterization of proteins and other macromolecules by agarose-gel chromatography." *J. Chromatogr.* **1978,** *152*, (1), 21-32.

282.   Holthoff, H.; Egelhaaf, S. U.; Borkovec, M.; Schurtenberger, P.; Sticher, H., "Coagulation rate measurements of colloidal particles by simultaneous static and dynamic light scattering." *Langmuir* **1996,** *12*, (23), 5541-5549.

283.   Medina, R.; Perdomo, D.; Bubis, J., "The hydrodynamic properties of dark- and light-activated states of n-dodecyl beta-D-maltoside-solubilized bovine rhodopsin support the dimeric structure of both conformations." *J. Biol. Chem.* **2004,** *279*, (38), 39565-39573.

284.   Sun, T.; Chance, R. R.; Graessley, W. W.; Lohse, D. J., "A study of the separation principle in size exclusion chromatography." *Macromolecules* **2004,** *37*, (11), 4304-4312.

285.   Teraoka, I., "Calibration of retention volume in size exclusion chromatography by hydrodynamic radius." *Macromolecules* **2004,** *37*, (17), 6632-6639.

286.   National Institute of Standards and Technology (NIST) *Certificate of Analysis: SRM 1898 - Titanium dioxide nanomaterial*; Gaithersburg, MD, 2012.

287.   Schmidt, M. P.; Martinez, C. E., "Kinetic and conformational insights of protein adsorption onto montmorillonite revealed using in situ ATR-FTIR/2D-COS." *Langmuir* **2016,** *32*, (31), 7719-7729.

288.   Haerifar, M.; Azizian, S., "Mixed surface reaction and diffusion-controlled kinetic model for adsorption at the solid/solution interface." *J. Phys. Chem. C* **2013,** *117*, (16), 8310-8317.

289.   *Agilent 1260 Infinity Fluorescence Detector*; Agilent Technologies, Inc.: Germany, 2013.

290.   Davda, J.; Labhasetwar, V., "Characterization of nanoparticle uptake by endothelial cells." *Int. J. Pharm.* **2002,** *233*, (1), 51-59.

291.   Cai, H.; Liang, Z.; Huang, W.; Wen, L.; Chen, G., "Engineering PLGA nano-based systems through understanding the influence of nanoparticle properties and cell-penetrating peptides for cochlear drug delivery." *Int. J. Pharm.* **2017,** *532*, (1), 55-65.

292.   Yin Win, K.; Feng, S.-S., "Effects of particle size and surface coating on cellular uptake of polymeric nanoparticles for oral delivery of anticancer drugs." *Biomaterials* **2005,** *26*, (15), 2713-2722.

293.   Eley, J. G.; Pujari, V. D.; McLane, J., "Poly (Lactide-co-Glycolide) Nanoparticles Containing Coumarin-6 for Suppository Delivery: In Vitro Release Profile and In Vivo Tissue Distribution." *Drug Delivery* **2004,** *11*, (4), 255-261.

294.   Sahoo, S. K.; Panyam, J.; Prabha, S.; Labhasetwar, V., "Residual polyvinyl alcohol associated with poly (d,l-lactide-co-glycolide) nanoparticles affects their physical properties and cellular uptake." *J. Controlled Release* **2002,** *82*, (1), 105-114.

295.   Butler, S. M.; Tracy, M. A.; Tilton, R. D., "Adsorption of serum albumin to thin films of poly(lactide-co-glycolide)." *J. Controlled Release* **1999,** *58*, (3), 335-347.

296.   Xu, J. X.; Vithanage, B. C. N.; Athukorale, S. A.; Zhang, D., "Scattering and absorption differ drastically in their inner filter effects on fluorescence, resonance synchronous, and polarized resonance synchronous spectroscopic measurements." *Analyst* **2018,** *143*, (14), 3382-3389.

297.   Noyes, A. A.; Whitney, W. R., "The rate of solution of solid substances in their own solutions." *J. Am. Chem. Soc.* **1897,** *19*, (12), 930-934.

298.   Costa, P.; Sousa Lobo, J. M., "Modeling and comparison of dissolution profiles." *Eur. J. Pharm. Sci.* **2001,** *13*, (2), 123-133.

APPENDIX A. SUPPORTING INFORMATION FOR CHAPTER 2

A.1 Chemical Reagents

Potassium phosphate monobasic anhydrous and sodium phosphate dibasic heptahydrate (both ACS grade, Amresco, Solon, OH) were used for phosphate buffers. Sodium bicarbonate (> 99.7%, ACS grade), sodium chloride (> 99.0%, ACS grade), and calcium chloride (> 97.0%, anhydrous, ACS grade) were obtained from Sigma Aldrich (St. Louis, MO). Phosphoric acid (85%, ACS grade, Ricca Chemical Company, Arlington, TX), Coomassie Brilliant Blue (MP Biomedicals, Santa Ana, California) and ethanol (anhydrous USP grade, Decon labs, King Of Prussia, PA) were used for the Bradford assay.
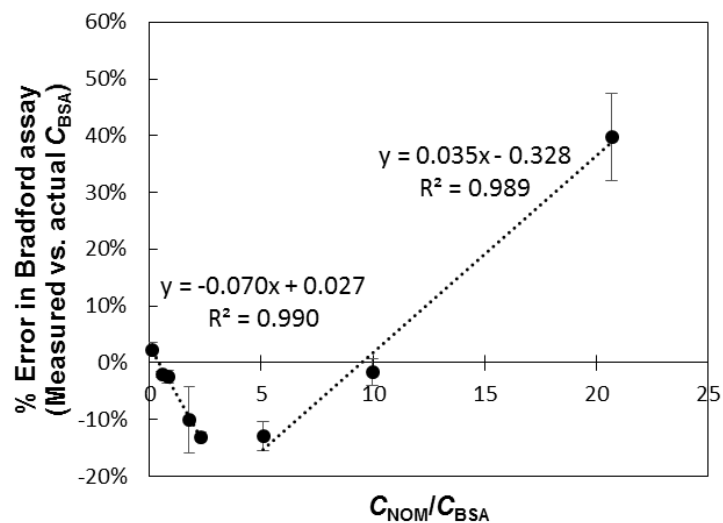
A.2 Bradford Assay

For the Bradford assay, the Bradford reagent was prepared by dissolution of 100 mg of Coomassie Blue in 50 mL of ethanol and 100 mL of 85% phosphoric acid, and the volume was made up to 1 L by adding Milli-Q water. During protein measurements, 2 mL of Bradford reagent was added to 0.2 mL of solutions containing bovine serum albumin (BSA). The concentration of BSA was quantified using the absorbance at 595 nm[277] or, for pure BSA supernatants that included high concentrations (up to 200 mg/L), using the ratio of absorbances at (595 and 450) nm, which extends the range of linearity of the calibration curve.[278] To further reduce variability in the spectrophotometric measurements, a single polystyrene cuvette was used for each set of measurements (calibration standards and samples). Between measurements, the cuvette was rinsed thoroughly with Milli-Q water, 50% ethanol, Milli-Q water, the Bradford background

solution (i.e., Bradford reagent without Coomassie Blue), and Milli-Q water. Each sample was prepared directly in the cuvette to avoid loss of dye by adsorption to external sample preparation containers. Blank checks were performed throughout each set of measurements to confirm cuvette cleanliness. The sample measurements were conducted by Dr. Stacey M. Louie.

A.3 Interferences in Quantification of BSA in the Presence of Natural Organic Matter (NOM)

To correct for interferences in the batch measurements of BSA and NOM in the mixtures, we prepared solutions containing both BSA and NOM, and after rotating for 24 h at room temperature, we quantified the concentrations of BSA with the Bradford assay in duplicate. Figure A.1 shows that the assay initially underestimates BSA concentration (likely due to competition of NOM for dye binding sites on the protein); however, beyond an NOM:BSA ratio of ≈ 4, the trend reverses (likely due to absorbance contributed from the NOM itself). While a curve fit may be more appropriate, for simplicity, we estimate two linear fits through the two regimes of data and apply the percent correction to the BSA measurements for the mixture supernatants in the adsorption experiments. The correction was applied based on the initial NOM:BSA ratio, rather than the final supernatant concentrations, assuming that the complexation occurs more rapidly than adsorption (both possible approaches for the correction were tested and found to not affect the overall conclusions that NOM outcompetes BSA to adsorb).

Figure A.1. Determination of percent error in quantification of BSA by the Bradford assay after equilibration with NOM for 24 h in 1.2 mM $NaHCO_3$, 0.85 mM $CaCl_2$, pH 7.5.

A.4 Size Exclusion Chromatography (SEC) in Mobile Phase of $NaHCO_3$ and $CaCl_2$

To investigate the complexation of BSA and NOM by SEC, ideally the mobile phase should be chosen to match the sample solvent since species will transfer into the mobile phase during the SEC run. Preliminary SEC runs on solutions containing BSA (100 mg/L) and NOM ((20 to 200) mg/L) in a buffer of 1.2 mM $NaHCO_3$ and 0.85 mM $CaCl_2$ (pH 7) were injected onto a Superdex 200 Increase 10/300 GL SEC column (GE Healthcare, Piscataway, NJ) with a matching mobile phase. However, fouling of the SEC column by NOM occurred in the Ca^{2+}-containing media, as identified by peak tailing and spurious results for mass recovery of BSA injected after NOM runs. Therefore, a mobile phase of 4 mM phosphate, 25 mM NaCl (pH 7) was used, where column fouling was not observed. The same trend was observed in both mobile phases for the UV_{350} and fluorescence peak areas (FLD, excitation/emission at 295/345 nm) of

145

BSA mixed with increasing concentrations of NOM (Figure A.2), demonstrating that the choice of eluent does not significantly change the extent of complexation measured.
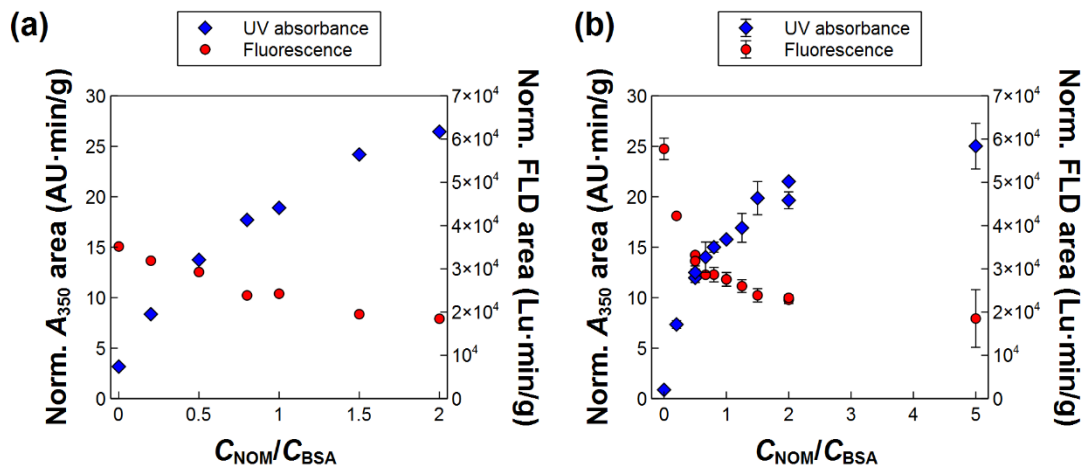

Figure A.2. Normalized BSA UV and FLD peak area for mixtures of NOM and BSA in a SEC mobile phase of 1.2 mM $NaHCO_3$+ 0.85 mM $CaCl_2$, pH 7 (a) or 4 mM phosphate+25 mM NaCl, pH 7 (b). Peak areas are normalized to mass of BSA.

A.5 SEC-Differential Refractive Index (dRI) Method for Quantification of NOM

A method was developed to separate and quantify NOM by SEC with dRI detection for solution depletion experiments to obtain adsorbed masses on TiO_2 NPs. Prior to sample analysis, both the UV extinction coefficient and RI increment (dn/dc) were needed, in order to evaluate recovery off the column as well as to calculate the mass of NOM depleted after adsorption to the NPs. The UV extinction coefficient at 280 nm was determined to be 11.9 mL/(mg cm) by batch measurements on a UV-vis spectrometer (Shimadzu UV-2600) on unfiltered NOM calibration standards. The dn/dc was then determined by measuring an unfiltered 200 mg/L sample by SEC-dRI and determining the dn/dc value (0.146 mL/g) that gave the same mass recovery off the column for dRI peak area analysis compared to the UV_{280} peak area analysis. For this

146

analysis, the dRI peak should not elute with the negative solvent peak in the SEC-dRI measurement. To achieve this, the measurement was performed in 2 mM phosphate buffer without NaCl to reduce adsorption to the column and ensure nearly complete elution of the NOM prior to the negative solvent peak.[128]

All samples were then run on a Superdex 75 column in a mobile phase of 4 mM phosphate and 25 mM NaCl at pH 7, where the higher salt concentration is needed to ensure good recovery of BSA from the column as well as separation of BSA and NOM on the column (for complexation analyses). Solution depletion in supernatants collected for adsorption experiments was calculated from the difference in the dRI peak areas for the initial NOM or NOM + BSA solution (calculated based on SEC-dRI calibration curves for pure NOM and BSA solutions) versus the supernatant (measured directly on each sample), using dn/dc, the flow rate, and the injection volume to convert the loss in dRI peak area to the mass or concentration depleted. In supernatants containing both BSA and NOM, the Bradford assay measurement provided the concentration of BSA. The contribution of the BSA to the measured dRI peak area could then be subtracted using the known BSA concentration and SEC-dRI calibration curve on pure BSA. Examples of chromatograms and difference chromatograms (showing the adsorbing species) are provided in Figure A.3.
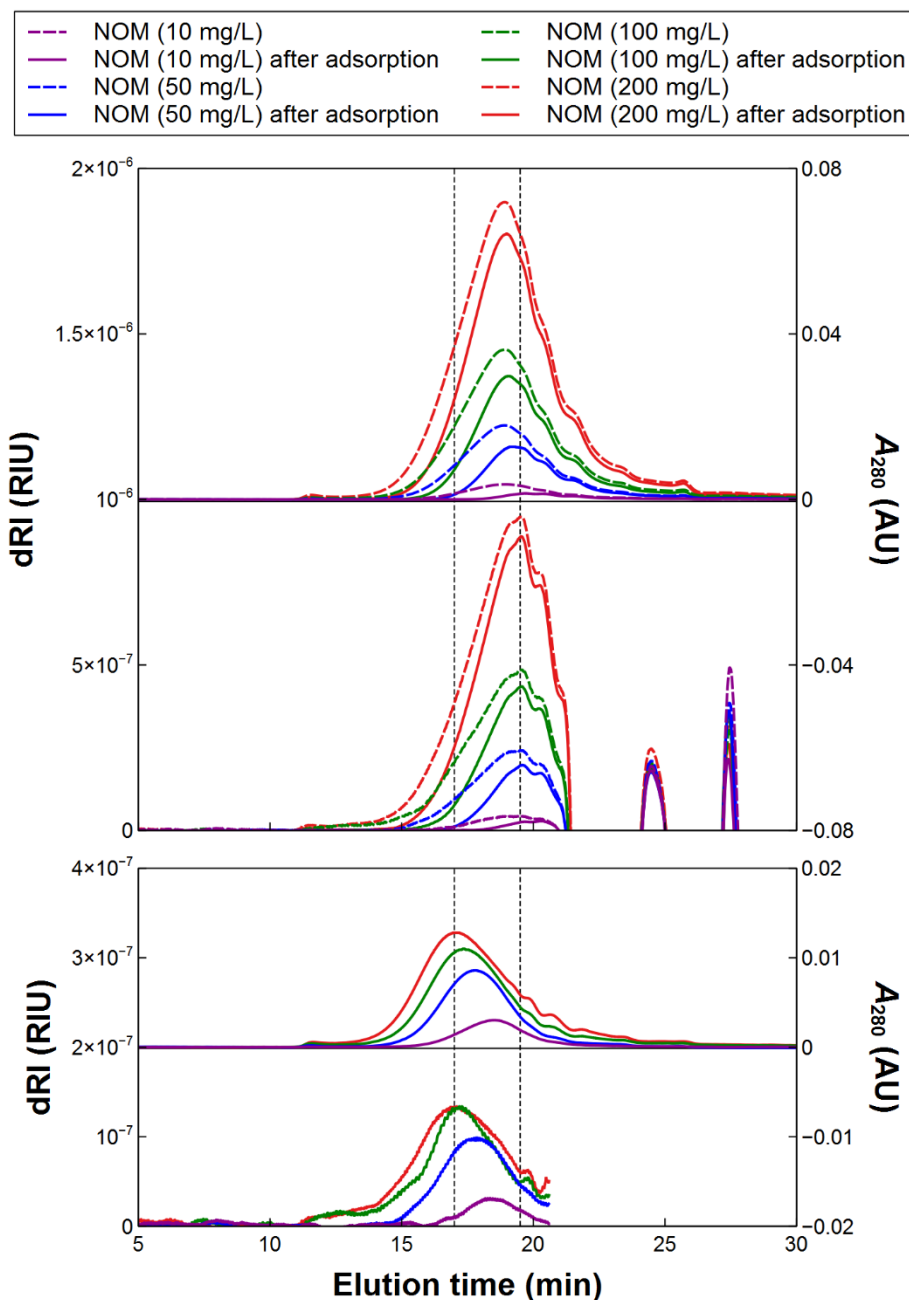
Figure A.3. SEC-dRI and SEC-A_{280} chromatograms (top) for NOM before and after adsorption onto 500 mg/L of TiO$_2$ NPs. The difference chromatograms (bottom) show adsorptive fractionation of the NOM.

After obtaining the raw change in the dRI peak areas, the following corrections were applied consistently across all samples measured:

1. Mass recovery off the column was computed from the UV_{280} recovery across the entire peak area for unfiltered calibration standards, and then applied to correct the masses that were computed from the change in dRI peak area. The mass recovery was > 90% on all sample sets.

2. Based on the calibration standards, $\approx 20\%$ of the dRI peak for the NOM eluted over the negative solvent peaks and could not be analyzed directly, with peak limits set to (9 to 20.6) min for the dRI analysis. Because of the adsorptive fractionation of NOM favoring depletion primarily of the higher molar mass (faster-eluting) species, the missing peak area represents a relatively small portion of the adsorbed NOM. However, as the A_{280} difference chromatogram showed a similar shape to the RI chromatogram, the % depletion of UV area in the region eluting after 20.6 min was used to estimate the % mass depletion in that region.

3. Complexation of NOM onto BSA resulted in imperfect additivity of the dRI from the pure calibration standards, such that the predicted peak area by addition of pure NOM and pure BSA calibration standards was $\approx 5.4\%$ lower than the measured dRI peak area in mixtures of known concentrations. The degree of error in the supernatant samples for the NOM/BSA mixtures is challenging to estimate since the initial and final BSA concentration, as well as its interaction with NOM, will all affect the error. Instead, a correction factor of 2.7% on the measured dRI peak area (average between 0% and 5.4% error) was consistently applied across all samples containing BSA to account for the possible change in dn/dc in mixtures.

The SEC-dRI method was tested against two independent measures of concentration. First, for single-component BSA adsorption, the method provided similar

results (average error of 4%) to the Bradford assay for the BSA supernatant concentrations, despite the appearance of BSA aggregates upon exposure to TiO_2 NPs (e.g., see Figure A.11 hereafter) which strongly affected the UV and light scattering data but not the dRI data. For NOM, the unfiltered stock NOM, 0.22 μm filtered stock, and two supernatants after adsorption to TiO_2 were sent for TOC analysis to a commercial laboratory to compare against the SEC-dRI method. SEC-dRI and TOC measurements matched within 5% for the 0.22 μm filter loss and adsorption from 200 mg/L of NOM, while 14% error was obtained for a second adsorption sample (from 80 mg/L of NOM). The source of the higher error in the one sample was not identified (samples for SEC-dRI and TOC were not matched from an identical sample but were from two independently prepared samples). In both adsorption measurements, the measured NOM concentration by SEC-dRI analysis was intermediate between those determined by UV_{280} analysis and TOC analysis.

A.6 Colloidal Stability of TiO_2 NPs after Adsorption Experiments

In the $CaCl_2/NaHCO_3$ buffer (pH 7 to 7.5) used here, the z-average diameter of the TiO_2 NPs measured by dynamic light scattering (DLS) after adsorption experiments in suspensions with low concentrations of NOM or BSA shows severe agglomeration of the NPs (Figure A.4), at the two lowest NOM concentrations of (10 and 20) mg/L, the agglomerate size is > 1 μm and outside the range of reliable DLS measurements. However, increasing the concentration of either NOM or BSA to ≈ 100 mg/L or higher for the high TiO_2 concentrations tested here (0.5 g/L) significantly reduces the aggregation. The colloidal stabilization can be explained by electrostatic or electrosteric

repulsion.[157] While other studies have observed enhanced aggregation of NPs due to bridging by NOM in the presence of Ca^{2+},[279] it can be inferred that in our case there is no bridging at high NOM concentrations. At low concentrations, it is not possible to distinguish if NOM/Ca^{2+} participated in bridging since the NPs themselves agglomerate rapidly in the medium used.
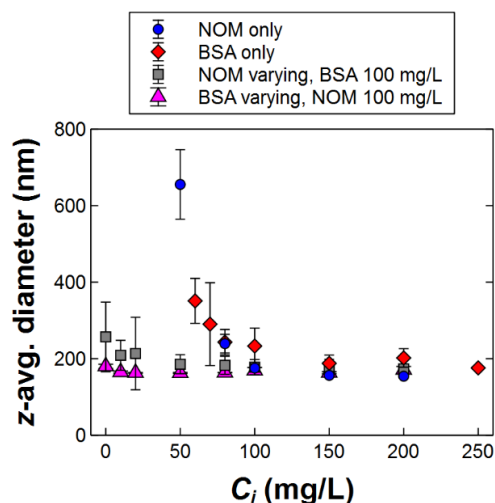
Figure A.4. DLS size measurements show colloidal stability imparted by NOM and BSA. Measurements were taken directly on the samples collected for the adsorption isotherms. Error bars represent the standard deviation over triplicate samples

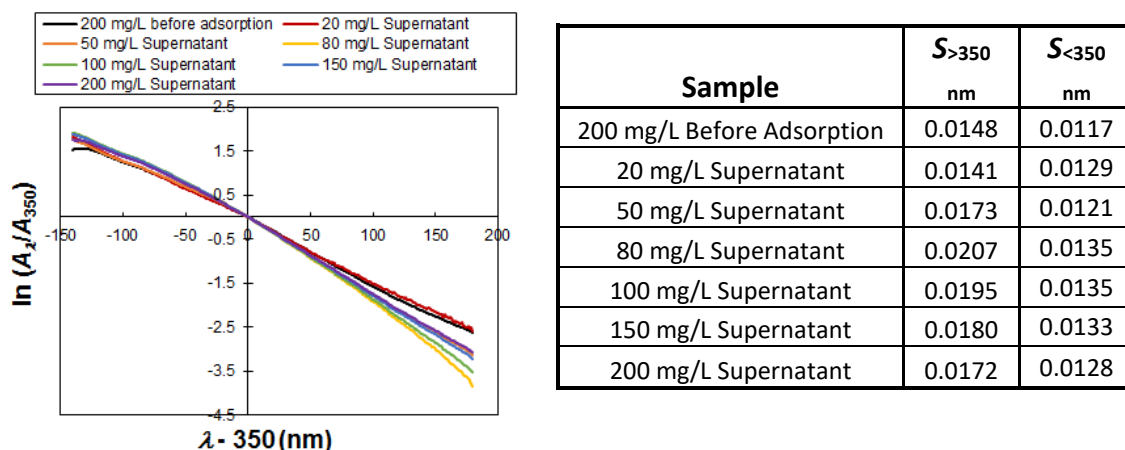### A.7 Change in NOM Spectral Properties after Adsorption

Higher aromaticity or higher molar mass NOM species are typically observed to adsorb preferentially to nanoparticles and other surfaces. The use of UV-vis absorbance would be a simple method to determine solution depletion in adsorption experiments but would require a proportionality factor between the change in UV absorbance and a more universal method for NOM detection, such as total organic carbon (TOC) or

refractive index (RI) analysis. Samples were analyzed to determine if such a correlation could be made confidently in our samples.

Batch UV-vis absorbance spectra were collected on NOM samples (without BSA) before and after adsorption to TiO_2 NPs and modeled as an exponential function that can be linearized to obtain a spectral slope parameter, S[132],

$$\ln\left(\frac{A_\lambda}{A_{\lambda_0}}\right) = -S(\lambda - \lambda_0), \tag{A.1}$$

where A_λ is the absorbance at wavelength λ, and λ_0 is a reference wavelength. As we observed different slopes in the < 350 nm and > 350 nm regions, we selected $\lambda_0 = 350$ nm and calculated the slopes separately in the two regions. The slope S is typically correlated to the molar mass of the NOM.[133, 134] For all samples except the lowest concentration (where competition among NOM species for adsorption is lowest), the slopes become steeper (S is higher) after adsorption relative to before adsorption (Figure A.5), consistent with prior studies investigating the use of spectral slope to identify the most active NOM species, e.g., in coagulation processes.[133] (We explore this further below with SEC-UV-DAD analysis.) The change in spectral slope makes solution depletion by UV-vis absorbance difficult to correlate to other methods such as TOC analysis, and hence we used SEC-dRI for NOM quantification as described above.

Sample	$S_{>350}$ nm	$S_{<350}$ nm
200 mg/L Before Adsorption	0.0148	0.0117
20 mg/L Supernatant	0.0141	0.0129
50 mg/L Supernatant	0.0173	0.0121
80 mg/L Supernatant	0.0207	0.0135
100 mg/L Supernatant	0.0195	0.0135
150 mg/L Supernatant	0.0180	0.0133
200 mg/L Supernatant	0.0172	0.0128

Figure A.5. Spectral analysis shows change in NOM spectral slope upon adsorptive fractionation.

A.8 Spectral Analysis of NOM Fractions by SEC-UV-DAD

Beyond the quantification of NOM adsorption, the UV diode array detector was set to collect full spectral data on the eluent from the SEC column, such that spectral slope (S) analysis can be performed at each time point in the SEC analysis (Figure A.6). The initial spectral data analysis was conducted by Luis R. Barco. The data for the initial NOM (before adsorption) provide a consistent explanation for the batch UV-vis observations, where the higher molar mass species that are depleted (Figure A.3) are those with lower S, leaving species in solution with higher S.
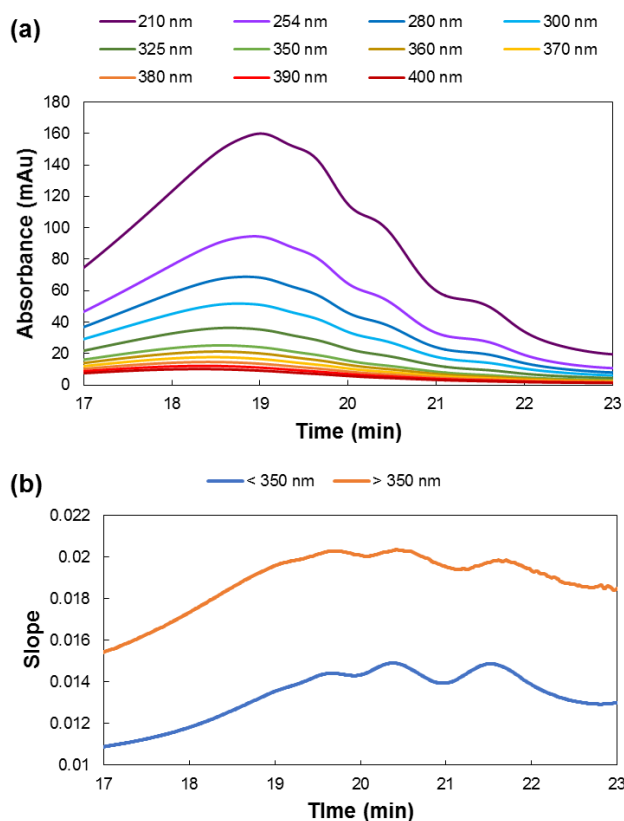
Figure A.6. SEC-UV-DAD chromatograms (a) used for spectral slope analysis (b).

A.9 Analysis of NOM Fractions by ATR-FTIR Spectroscopy

To further investigate chemical differences related to the adsorption fractionation observed, NOM species with molecular weights higher than ≈ 10 kDa were separated from lower molecular weight species in a pre-rinsed Amicon 10 kDa centrifugal ultrafiltration unit (Millipore Sigma, Burlington, MA). The molecular weight cutoff was selected by comparing the SEC chromatograms in Figure A.3 to those reported previously under the same conditions together with molar mass determination by online multi-angle light scattering (MALS).[128] The > 10 kDa fraction of NOM was then confirmed by SEC (not shown) to correspond roughly to the adsorbing species

154

identified in the SEC difference chromatograms (Figure A.3). The separated fractions were analyzed by attenuated total reflectance – Fourier transform infrared (ATR-FTIR) spectroscopy, which shows that NOM species with molecular weight less than 10 kDa have a peak around 1125 cm^{-1} that is not present in the high molecular weight fraction of NOM (Figure A.7).
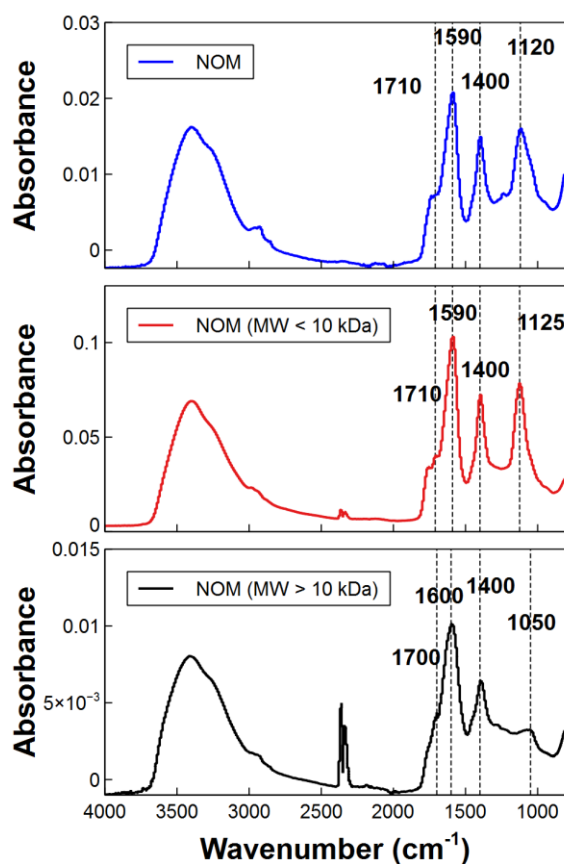
Figure A.7. ATR-FTIR spectra of unfractionated NOM, and NOM fractions with MW < 10 kDa and >10 kDa. Samples were dried from solutions (pH $\approx$ 7) onto a diamond/ZnSe ATR. The ATR crystal spectrum was used for background subtraction.

A.10 Single-component Langmuir Adsorption Model

The Langmuir model assumes that adsorption is a reversible process that has reached equilibrium, the surface is homogeneous, all sites are equivalent and accessible to all molecules, only one molecule can occupy each site, and there is no interaction between two adjacent adsorbed molecules. Equation A.2,

$$q_i = \frac{q_{\text{max},i}\, K_i C_{\text{e},i}}{1\, +\, K_i C_{\text{e},i}}, \tag{A.2}$$

presents the Langmuir adsorption model for a single-component sample, where q_i (mg/m^2) and $C_{\text{e},i}$ (mg/L) are experimental data for the adsorbed mass and equilibrium concentration of species i, respectively.

In this equation, K_i represents the Langmuir isotherm constant (L/mg), and $q_{\text{max},i}$ is the maximum monolayer adsorbed capacity (mg/m^2). Table A.1 summarizes the fitted Langmuir parameters for BSA and NOM. Standard errors and 95% confidence intervals on the fitted parameters from nonlinear regression were estimated using the Excel tool presented by Bolster and Hornberger for Langmuir isotherm analysis.[280]

Table A.1. Langmuir parameters for single-component BSA and NOM adsorption onto TiO$_2$

Parameter	Fitted values	Standard error	Approx. 95% confidence limits	
			Lower	Upper
K_{BSA} (L/mg)	1.1	0.4	0.06	2.1
$q_{\text{max,BSA}}$ (mg/m^2)	2.61	0.07	2.4	2.8
K_{NOM} (L/mg)	0.051	0.008	0.03	0.07
$q_{\text{max,NOM}}$ (mg/m^2)	0.90	0.04	0.81	0.99

A.11 Kinetic Competitive Adsorption Model

To derive the kinetic adsorption model, we considered the collision rate of each macromolecule with the TiO_2 NPs. The collision rate, Z, between the macromolecules and a single TiO_2 NP was calculated using Equation A.3[157],

$$Z = 4\pi D(R_1+R_2)N_{\infty,i},$$ (A.3)

where D is the summed diffusion coefficients for the macromolecule (D_1) and NP (D_2), and D_1 and D_2 were calculated by the Stokes–Einstein equation (Equation A.4). R_1 and R_2 are the radius of the macromolecule and the NP, respectively, and $N_{\infty,i}$ is the number concentration of macromolecules in bulk solution. The Stokes–Einstein equation is

$$D_i = \frac{k_B T}{6\pi\mu R_i},$$ (A.4)

where k_B, T, μ, and R_i are Boltzmann's constant, temperature, dynamic viscosity of water, and the radius of species i, respectively.

To consider all NPs instead of one, the number concentration of NPs in suspension was first estimated as

$$N_{TiO_2} = \frac{C_{TiO_2}}{\left(\rho_{TiO_2}\right)\left(\frac{4}{3}\pi R_{TiO_2}^3\right)},$$ (A.5)

where C_{TiO_2}, ρ_{TiO_2}, and R_{TiO_2} correspond to the mass concentration, density, and hydrodynamic radius, respectively, of the TiO_2 NPs. The remainder of the model equations and the stopping criterion for adsorption are presented in the main text.

The kinetic model was parameterized using the Langmuir single-component parameters ($q_{max,i}$) and values for the size and molar masses estimated from literature or experimental data. Table A.2 summarizes parameters used in this model. The radius and

MW of monomer BSA are assumed to be 3.48 nm[281] and 66.5 kDa, respectively; BSA dimer is roughly estimated to have a hydrodynamic radius 1.3 times larger than the monomer (based on hard-sphere dimers)[282] and MW twice that of the monomer; and the TiO_2 radius is estimated as the volume-average hydrodynamic radius measured by DLS. The MW of only the adsorbing NOM was estimated by considering the fraction of the NOM that has higher affinity for adsorption, with a molar mass of ≈ 27.5 kDa reported by Louie et al.[128] at the approximate peak elution location of the adsorbed fraction identified in Figure A3. The radius of NOM was estimated by comparing the peak elution time of the adsorbing NOM to that of BSA (3.48 nm)[281] and Ribonuclease A (1.64 nm)[283] as size standards for a universal SEC calibration curve, which assumes a linear relationship between elution time and the log (hydrodynamic diameter).[284, 285] It is noted that the elution time of NOM is affected by the choice of eluent, which mediates the repulsive or adsorptive interactions between NOM and the SEC column used here. The SEC eluent used in this study was selected so that the molar mass determined across the elution time for the NOM sample roughly overlays the profile for the BSA and Ribonuclease A (with known molar masses and sizes). The density of TiO_2 was computed as a weighted average of anatase and rutile densities based on the reported composition in the NIST SRM 1898 Certificate of Analysis.[286]

Table A.2. Parameters used in the kinetic competitive adsorption model

Parameter	Value
T	298 K
$R_{BSA, monomer}$	3.48 nm
$R_{BSA, dimer}$	4.52 nm
R_{NOM}	2.0 nm
R_{TiO2}	60.5 nm
$MW_{BSA, monomer}$	66.5 kDa
$MW_{BSA, dimer}$	130 kDa
MW_{NOM}	27.5 kDa
ρ_{TiO2}	4000 kg/m^3

A.12 *In Situ* ATR-FTIR Results for Single-component Adsorption to TiO$_2$ NPs

Figure A.8 shows the ATR-FTIR spectra for *in situ* adsorption of BSA and NOM onto deposited TiO$_2$ NPs. For NOM, the non-adsorbing peak (1125 cm^{-1}) that was identified *ex situ* in Figure A.7 was also confirmed to not adsorb in the *in situ* experiments. The negative peak in the BSA spectra is attributable to water loss as the protein displaces liquid water on the surface of the NPs.[287] Further fitting of the ATR-FTIR spectra in mixture and sequential adsorption experiments (*vide infra*) assumes that the water loss per adsorbed BSA remains constant in each experiment, i.e., no spectral processing for liquid water was performed.
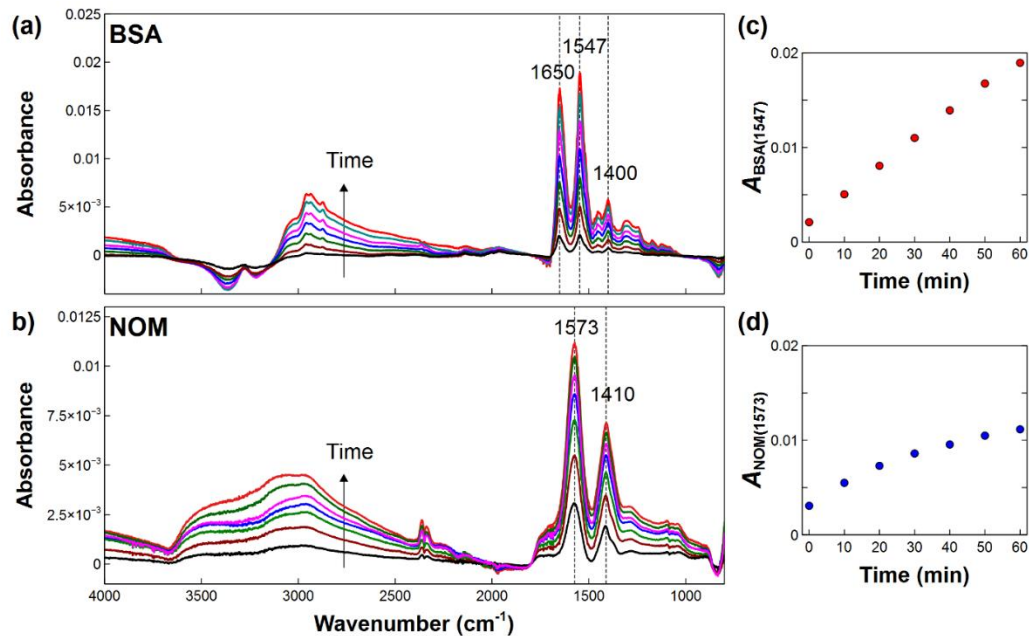
Figure A.8. *In situ* ATR-FTIR spectra for 100 mg/L of BSA (a) and 100 mg/L of NOM (b) adsorbing onto TiO$_2$ NPs, and the kinetics of adsorption as monitored by the peak height for BSA at 1547 cm^{-1} (c) and NOM at 1573 cm^{-1} (d).

A.13 ATR-FTIR Spectral Fitting for Adsorption from Mixtures onto TiO$_2$ NPs

During *in situ* experiments, baseline shifts can occur due to changes in the detector temperature or other conditions. To model the *in situ* ATR-FTIR spectra, all spectra were first shifted vertically to have a zero point at 1800 cm^{-1}, which was found to have minimal contribution of absorbance from either BSA or NOM. No further baseline corrections were applied. Since BSA and NOM show peak overlaps, instead of using one specific peak for quantification, the entire wavenumber region from (1300 to 1800) cm^{-1} was fitted as a linear summation of the pure adsorbed BSA and pure adsorbed NOM spectra (Figure A.8), as in Equation A.6,

$$A_{\text{mixture}}(\upsilon) = A'_{\text{BSA}} A_{\text{ref,BSA}}(\upsilon) + A'_{\text{NOM}} A_{\text{ref,NOM}}(\upsilon), \tag{A.6}$$

where $A_{\text{mixture}}(\upsilon)$ is the absorbance at each wavenumber υ in the mixed adsorbed layer. A'_{BSA} and A'_{NOM} are the BSA and NOM coefficients, respectively, representing the

signal strength of each species relative to $A_{ref,BSA}(\upsilon)$ and $A_{ref,NOM}(\upsilon)$ (the absorbance of pure BSA and pure NOM, respectively, adsorbed onto TiO_2 NPs after 1 h which serve as "reference spectra" for the fitting). The sum of squared errors across the (1300 to 1800) cm^{-1} range is minimized to obtain the best-fit BSA and NOM coefficients. We assume that the liquid water displacement per adsorbed BSA or NOM molecule in the reference spectra (Figure A.8) is consistent in the mixture spectra, such that no corrections for changes in adsorbed liquid water were made prior to the fitting analysis.

A.14 *In situ* ATR-FTIR Results for Sequential Adsorption of Pure BSA onto NOM-coated TiO_2 NPs

The sequential adsorption of pure BSA over TiO_2 NPs that were pre-coated with NOM was monitored by *in situ* ATR-FTIR spectroscopy. Minimal displacement of NOM by BSA was observed. Rather, the pure BSA overcoated the NOM layer, with the adsorption showing a nearly linear profile over the first 60 min (similar to BSA adsorption to uncoated TiO_2 NPs in Figure A.8) and then beginning to plateau over the next several hours.
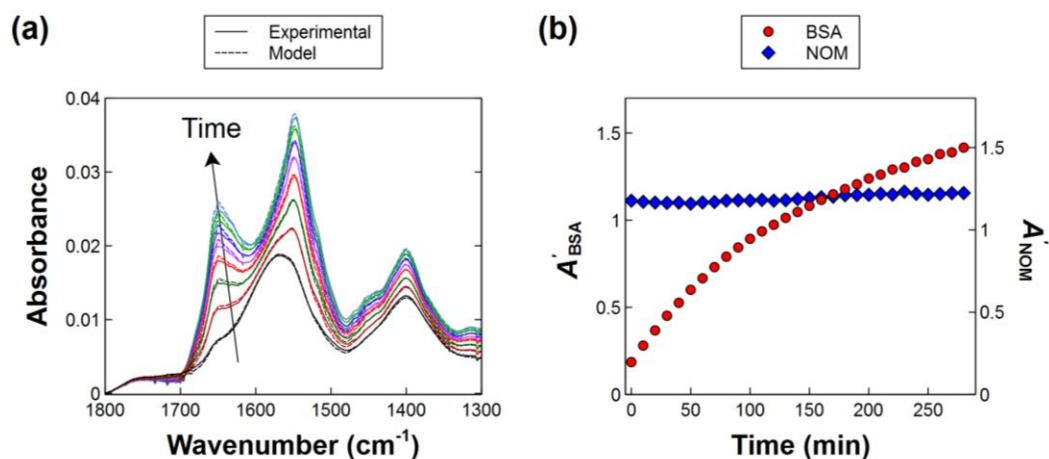
Figure A.9. *In situ* ATR-FTIR spectra for BSA (100 mg/L) adsorption over NOM-coated TiO$_2$. Spectra were reprocessed with the spectrum of clean buffer over TiO$_2$.

## A.15 Quantification of NOM Complexation to BSA and Evaluation of Complexation Kinetics

NOM complexation onto BSA was estimated across a range of concentration ratios by SEC-dRI analysis of the depletion of the free NOM peak as NOM attached onto the BSA peaks, and the complexation kinetics were evaluated by monitoring the change in UV absorbance across the BSA peak over time for a mixture of BSA (100 mg/L) and NOM (100 mg/L), as shown in Figure A.10.
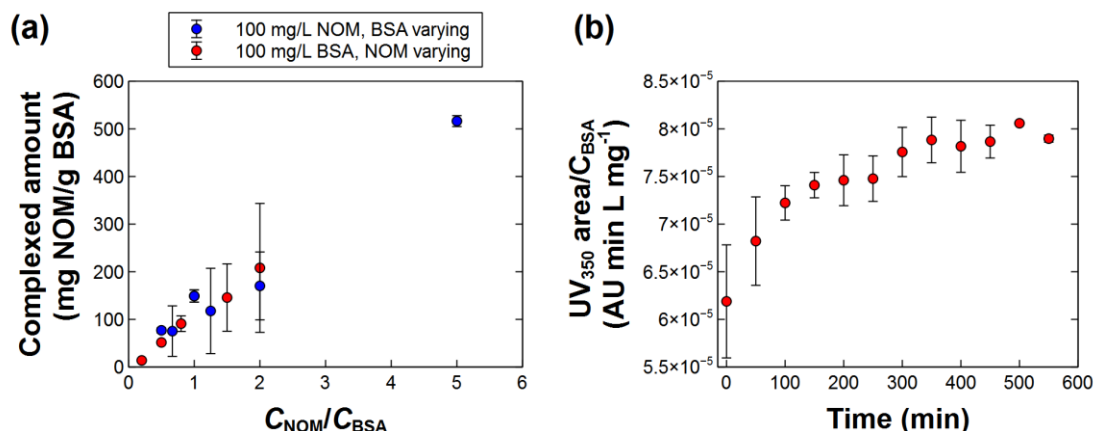
Figure A.10. NOM complexation onto BSA was estimated across a range of concentration ratios by SEC-dRI analysis of the depletion of the free NOM peak. Error bars represent the standard deviation for $n = 2$ independently prepared samples.

A.16 Isolation of BSA-NOM Complexes and Adsorption to TiO_2 NPs

BSA-NOM complexes were isolated from mixtures of 200 mg/L BSA and 100 mg/L NOM in the same buffer as the batch adsorption experiments, using a 50 kDa Amicon centrifugal ultrafiltration unit to retain BSA-NOM complexes and remove free NOM. The Amicon filters were pre-rinsed by centrifuging clean buffer three times through the membrane at 4500 rpm (relative centrifugal force (RCF), $RCF_{min} = 1879$ *g* and $RCF_{max} = 4415$ *g*) for 10 min (Sorvall Legend XTR Centrifuge, Thermo Fisher Scientific, Waltham, MA), before adding the BSA-NOM mixture and centrifuging at the same conditions to separate. To thoroughly rinse free NOM from the retained complex in the filter, the retentate was washed with buffer until the filtrate had no visible color apparent. Minimal BSA loss in the filter (5%) was measured by the Bradford assay, and the persistence of NOM complexed to the BSA and removal of most (but not all) of the free NOM was confirmed by SEC-UV$_{280}$ analysis (Figure A.11a).
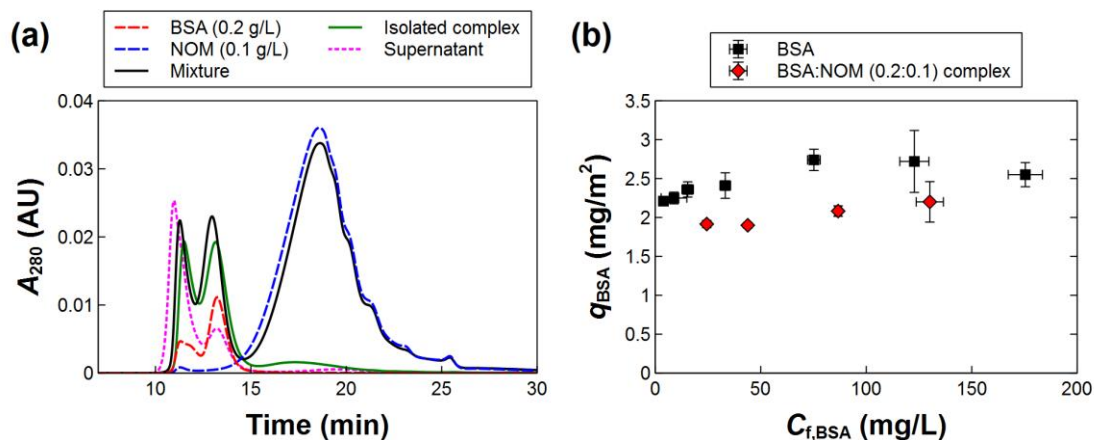
Figure A.11. SEC-UV$_{280}$ chromatograms (a) for BSA, NOM, the mixture, the isolated complex, and the supernatant of isolated complex (150 mg/L) adsorbing onto 0.5 g/L of TiO$_2$ NPs and (b) adsorption isotherm of BSA and complex.

The adsorption of the isolated BSA-NOM complexes onto uncoated TiO$_2$ NPs was measured by the solution depletion method (using the Bradford assay for BSA quantification) and compared to the adsorption of the pure BSA. While some reduction in adsorption of the isolated complex onto the uncoated TiO$_2$ was observed relative to pure BSA, some of the difference in adsorption in Figure A.11b may be attributable to remaining free NOM in the isolated complex (peak elution time > 15 min) that outcompetes BSA for adsorption (Figure A.11a). After exposure to the TiO$_2$ NPs, a large peak is also observed eluting at $\approx$ 11 min that does not appear in the dRI chromatogram (not shown) and is likely attributable to light scattering from large BSA aggregates. This peak was observed in all BSA-containing supernatants after exposure to the NPs for 24 h but not after mixing with any other species in the samples (NOM or the buffer) and also not observed in samples of pure NOM after adsorption to TiO$_2$.

A.17 Exponential Fit of the BSA and NOM Adsorption Kinetics in ATR-FTIR Experiments

Because the kinetics of adsorption onto the TiO_2 NP surface in the *in situ* ATR-FTIR experiments were slow and steady-state was not achieved within > 2 h in the experiments, we fitted a pseudo first-order kinetic adsorption model[288] to extrapolate the value of the steady-state adsorption coefficient. Equation A.7 presents this model as

$$A' = A'_{\infty} + (A'_0 - A'_{\infty})\exp(-kt). \qquad (A.7)$$

In this equation, A' is the fitted coefficient (see Equation A.6) for the adsorbed amount at time t, and A'_0 and A'_{∞} are the values of the coefficient at time zero and infinity, respectively. A'_{∞} and k were fitted by minimizing the sum of squared errors between the model and experimental data. Fitted A'_{∞} values were compared for BSA adsorption in the mixture versus pure BSA adsorption to estimate the relative extents of adsorption of complexed and pure BSA to the TiO_2 NPs.

A.18 *In Situ* ATR-FTIR Results for Sequential Adsorption of BSA-NOM Mixtures and Pure BSA onto NOM-coated TiO_2 NPs

In addition to the sequential ATR-FTIR experiments presented in the main text, two additional experiments were performed (Figure A.12) to investigate the role of concentrations or degree of complexation. Extrapolating the kinetic adsorption data to estimate steady-state adsorbed amounts for BSA from the mixture and pure BSA (Equation A.7), the relative adsorption of complexed BSA to pure BSA was 0.51 ± 0.06 ($n = 2$ experiments) for the (200:100) mg/L mixture of BSA:NOM compared to 200 mg/L of pure BSA, 0.56 ± 0.05 ($n = 2$ experiments) for the (100:200) mg/L mixture of

BSA:NOM compared to 100 mg/L of pure BSA, and 0.16 ± 0.10 ($n = 2$ experiments) for the (50:100) mg/L mixture of BSA:NOM compared to 50 mg/L of pure BSA. Therefore, while complexes from the mixture with (50:100) mg/L of BSA:NOM mixture in Figure A.12b appear to adsorb to less extent to the TiO_2, the effect can be attributable to the lower concentration of BSA rather than the degree of complexation, as the adsorption for (100:200) mg/L of BSA:NOM (also 2:1 NOM:BSA) in Figure A.12a is similar to that in Figure 2.4. However, we emphasize that across all cases, pure BSA is consistently able to adsorb to additional sites that are not able to be occupied by the BSA:NOM complexes.
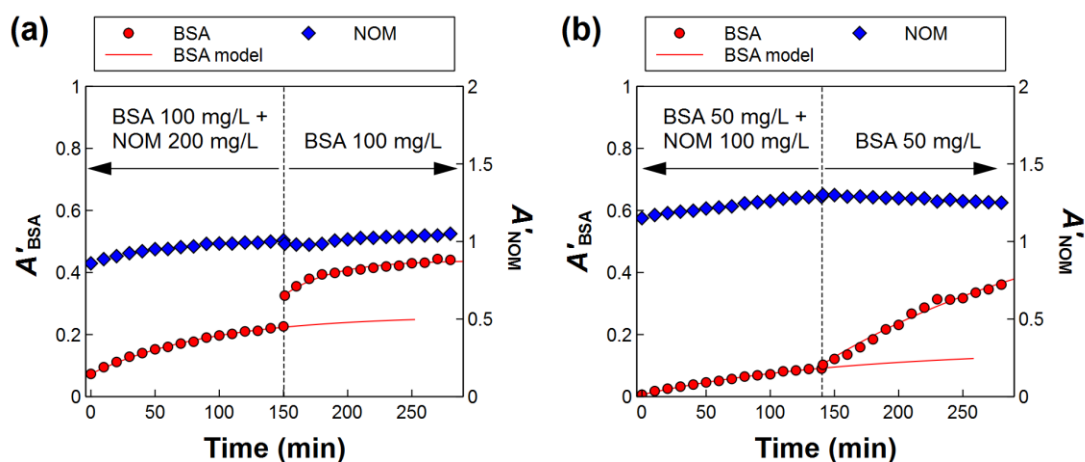
Figure A.12. *In situ* ATR-FTIR experiment for the sequential adsorption of a mixture of BSA and NOM, followed by pure BSA, over a NOM layer (pre-adsorbed from 100 mg/L) on TiO_2 NPs.

A.19 Multilayer Adsorption Model

All batch adsorption experiments in this study were conducted by exposing TiO_2 NPs to the NOM and BSA simultaneously in mixtures, where monolayer adsorption models were satisfactory due to the suppression of overcoating by complexation onto BSA. However, our FTIR data showed the possibility of extensive multilayer formation

upon sequential exposure to a pure protein solution. To model this multilayer adsorption, we can propose distinct adsorption equilibria in Equation 2.4 indicating a different interaction with empty sites and filled sites,

$$q_i(t) = \frac{q_{\max,i\leftrightarrow TiO_2}K_{i\leftrightarrow TiO_2}C_i(t)}{1 + K_{i\leftrightarrow TiO_2}C_i(t)}\left(1 - \sum_{j\neq i}\frac{q_j}{q_{\max,j}}\right)$$
$$+ \sum_{j\neq i}\left(\frac{q_{\max,i\leftrightarrow j}K_{i\leftrightarrow j}C_i(t)}{1 + K_{i\leftrightarrow j}C_i(t)}\frac{q_j}{q_{\max,j}}\right).$$

(A.8)

In this equation, $q_{\max,i\leftrightarrow TiO2}$ and $K_{i\leftrightarrow TiO2}$ are the Langmuir parameters from the single-component adsorption isotherm for i adsorbing to TiO_2. A second Langmuir isotherm is defined for adsorption to the sites filled by the other species j. (If this interaction is not Langmuirian, the term can be replaced with a different isotherm function, for example, a linear isotherm.)

If the FTIR sequential adsorption results are taken semi-quantitatively with the assumptions that, after NOM pre-adsorption, the complexed BSA adsorbs only to remaining bare TiO_2 sites and pure BSA adsorbs only to the NOM coating thereafter, then the data can theoretically be used to parameterize this model given the surface coverage and adsorbed mass of pre-adsorbed NOM (using the single-component Langmuir isotherm), and the ratio of the maximum adsorbed BSA complex to the maximum adsorbed pure BSA. For example, for the results shown in Figures 1 and 4, 100 mg/L of initial NOM coating is predicted to produce 83% surface coverage at 0.75 mg/m². The 200 mg/L of complexed BSA in the BSA-NOM mixture may then saturate the remaining 17% of vacant surface sites to produce an adsorbed mass of $\approx 17\% \times 2.6$ mg/m² or 0.44 mg/m². Finally comparing the relative increase in BSA adsorption for

the pure versus mixture BSA, the pure BSA adsorbing (presumably onto the NOM) would be 0.42 mg/m^2, or about 0.56 mg of BSA overcoating per mg of NOM coating on the surface. If several pure BSA concentrations for the last multilayer coating stage are tested in this manner (or in batch adsorption experiments of pure BSA onto washed, NOM-coated TiO$_2$), the BSA↔NOM interaction parameters in Equation A.8 can then be obtained experimentally.

An alternative approach can be to write the attachment efficiency in the adsorption rate equation (Equation 2.2) as a function of the surface coverage by other adsorbates, i.e., allowing the other adsorbates to produce either an increased or decreased energy barrier to adsorption. A complexation rate equation can also be written to explicitly treat complexed BSA as a species with different adsorption behavior than pure BSA. Then, instead of having three types of species in the rate equation (TiO$_2$ NPs, NOM, and BSA), a fourth species would be present (BSA-NOM complex) and the depletion or generation of the three macromolecular species would be determined by both the adsorption and complexation rate equations simultaneously. In this system, the extent of multilayer formation will depend on the relative timescales for complexation and adsorption and hence the concentrations of NPs, BSA, and NOM. These models would require more detailed kinetic studies of the complexation and adsorption processes to parameterize and are left for implementation in future studies.

APPENDIX B. SUPPORTING INFORMATION FOR CHAPTER 3

B.1 Transmission Electron Microscope (TEM) Images of the Synthesized Nanoparticles (NPs)
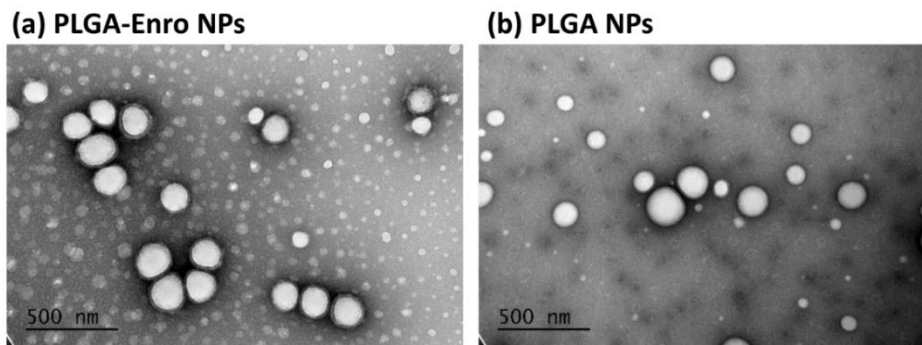
Figure B.1. TEM images of enrofloxacin-loaded poly(lactic-*co*-glycolic acid) (PLGA-Enro) NPs (a) and empty PLGA NPs (b). Experiments were conducted by Dr. Carlos E. Astete.

## B.2 Attenuated Total Reflectance – Fourier Transform Infrared (ATR-FTIR) Spectra
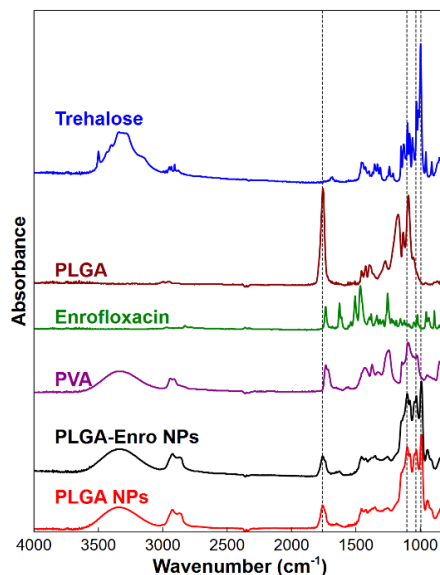
Figure B.2. ATR-FTIR spectra of the synthesized PLGA, PLGA-Enro NPs and materials used during the synthesis, including PLGA, PVA, enrofloxacin, and trehalose.

B.3 Glass Transition Temperature (T_g) of PLGA-Enro NPs

The calculated values for PLGA-Enro NPs from DSC measurements are T_g (inflection point method) (32.9 ± 0.8) °C, onset point (28.5 ± 0.3) °C, and offset point (37.67 ± 0.09) °C. The calculated values for PLGA NPs are T_g (inflection point method) 31.26 °C, onset point 28.21 °C, and offset point 34.96 °C. All measurements and data analysis was performed by Dr. Rafael Cueto.
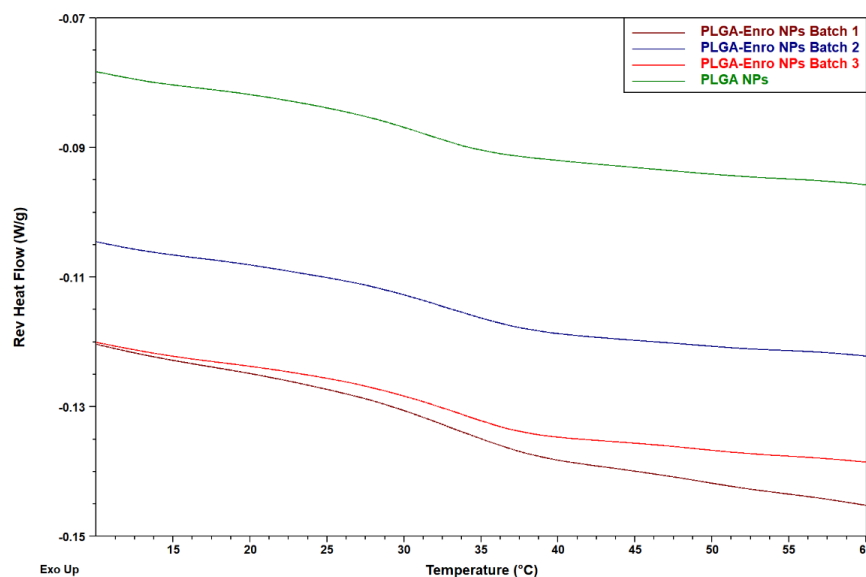
Figure B.3. Determination of T_g for PLGA-Enro NPs, from the second heating differential scanning calorimetry (DSC) plot. Experiments and data analysis were conducted by Dr. Rafael Cueto.

B.4 Corrections on Measured Enrofloxacin Concentrations in Dialysate Samples

In this study, collection of samples from inside the dialysis device for asymmetric flow field–flow fractionation (AF4) analysis removes NPs from the system, and therefore the amount of drug available to release is depleted between each measurement. In addition, removal of sample from the dialysate for analysis by high

performance liquid chromatography (HPLC) analysis and replacement with fresh buffer results in a small depletion and dilution of drug from one time point to the next. Therefore, Equation B.1 was applied to correct the enrofloxacin concentration measured by HPLC for these depletions

$$C_{d,outer,N} = \sum_{i=1}^{N} \left[\frac{(C_{meas,i} - C_{meas,i-1})V_{outer} + C_{meas,i-1}V_{r,outer}}{V_{outer}} \left(\frac{V_{inner}}{V_{inner} - (i-1)V_{r,inner}} \right) \right], \qquad (B.1)$$

where i is the counter for each sample collection from 1 to N samples (with $i = 1$ representing the sample collected at time 0), $C_{meas,i}$ is the measured concentration (by HPLC) for sample i, V_{outer} is the total volume of phosphate buffer saline (PBS) in the reservoir (120 mL), V_{inner} is the volume of NP suspension inside the dialysis device (1 mL), $V_{r,outer}$ is the volume of dialysate removed from the reservoir for each sample collection (0.4 mL), $V_{r,inner}$ is the volume of NP suspension removed from inside the dialysis device for each sample collection (0.02 mL), and $C_{d,outer,N}$ is the corrected concentration for the Nth sample collected.

Equation B.1 represents the mass balance for the accumulation or summation of released enrofloxacin in the dialysate from the first sample collection to the Nth sample collection. The first correction factor, $C_{meas,i-1}V_{r,outer}$, accounts for the mass of enrofloxacin removed with each prior NP collection from the reservoir. The second factor, $V_{inner}/(V_{inner} - (i-1)V_{r,inner})$, accounts for the removal of NP suspension from inside the dialysis device and proportional loss of releasable drug present in the system. $C_{meas,0}$ is taken to be zero prior to initiation of the release experiment (resulting in no correction of the first measurement, $N = 1$, at time zero).

B.5 Optimized AF4 Flow Parameters

For all samples, the detector flow rate was 0.5 mL/min, and the injector flow rate was 0.2 mL/min with a 50 μL injection volume. The AF4 steps and crossflow rate during each step are reported in Table B.1 for the optimized flow conditions.

Table B.1. Crossflow rates and duration of each separation step in the optimized AF4 method

Mode	Duration (min)	Crossflow rate (mL/min)	Purpose
Elution	6	0.15	Stabilize flow and baselines to those used during NP analysis
Focus	1	1.5	Stabilize focus flow
Focus + injection	4	1.5	Introduce and focus NP sample; remove unentrapped drug
Elution	58	0.15	Size separation of NPs for online characterization
Elution + injection	15	0	Flush the AF4 injection port and channel
Elution	6	0	Flush the AF4 channel
Elution	10	0.15	Restabilize flow and baselines to those used during NP analysis

## B.6 Fluorescence detector (FLD) Optimization

To find the optimum excitation and emission wavelengths for the FLD detector setup in AF4 measurements, the suspension of enrofloxacin-loaded poly lactic-*co*-glycolic acid (PLGA) nanoparticles (PLGA-Enro NPs) was injected to the HPLC system at 0.5 g/L as NPs in PBS without any further pretreatment and using a union (no separation). The optimum FLD wavelengths were obtained following the instrument manual.[289] Briefly, several injections were used to identify the peak emission

wavelength at a fixed excitation wavelength, followed by identifying the maximum excitation wavelength at the peak emission wavelength, and finally identifying the maximum emission wavelength again for the optimal excitation wavelength. The optimum wavelengths were 280 nm and 420 nm for the excitation and emission wavelengths, respectively.

B.7 Quantification of Entrapped Drug in PLGA-Enro NPs by Standard Additions

To obtain the drug loading and entrapment efficiency, the standard addition method was applied. Standard additions of 1 mL of dissolved enrofloxacin (at various concentrations) were made to 3 mL of PLGA-Enro NPs (concentration of 0.5 g/L NPs (1 g/L of powder including the trehalose)), after which the NPs and dissolved drug were separated using either ultrafiltration or centrifugation. Controls without NPs were also evaluated. Although adsorptive loss to the ultrafiltration device was observed in the enrofloxacin-only controls (Figure B.4a), excipients in the NP formulation appear to coat the membrane, resulting in good drug recovery in the standard additions (Figure B.4b). The x-intercept of the standard addition plots (Figure B.4b) gives the free drug concentration as (10.8 ± 0.4) mg/L and (11.3 ± 0.5) mg/L enrofloxacin ($n = 3$ replicates) by ultrafiltration and centrifugation, respectively. The drug loading was then estimated by subtracting the free drug from the total drug concentration and dividing by the concentration of the NPs.
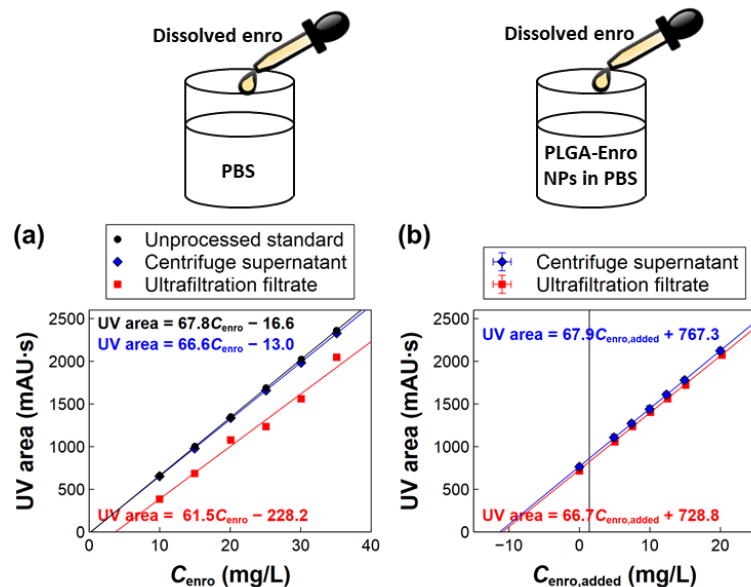
Figure B.4. UV$_{280}$ calibration for dissolved enrofloxacin in the supernatant (after centrifugation) or filtrate (after ultrafiltration) of samples containing no NPs (a) or PLGA-Enro NPs (b). Error bars in (b) represent the standard deviation of three replicates and are smaller than the marker size.

B.8 *In Situ* Purification of NPs with AF4

To verify that AF4 is capable of *in situ* removal of dissolved (unincorporated) drug from the NPs, physical mixtures of empty PLGA and enrofloxacin (denoted "PLGA + enro") were prepared (7.5 g/L of NPs + 249 mg/L enrofloxacin) and then inserted inside a dialysis bag in a reservoir maintained at 30 °C. At time zero, 20 μL of the sample was collected and diluted in PBS to a final concentration of 0.5 g/L as NPs and injected to AF4 (AF4 settings noted in Table B.1). The same procedure was also repeated after keeping the samples at 30 °C for 47 h. Negligible contribution of the unentrapped drug is observed in the FLD$_{drug}$ chromatograms (Figure B.5).
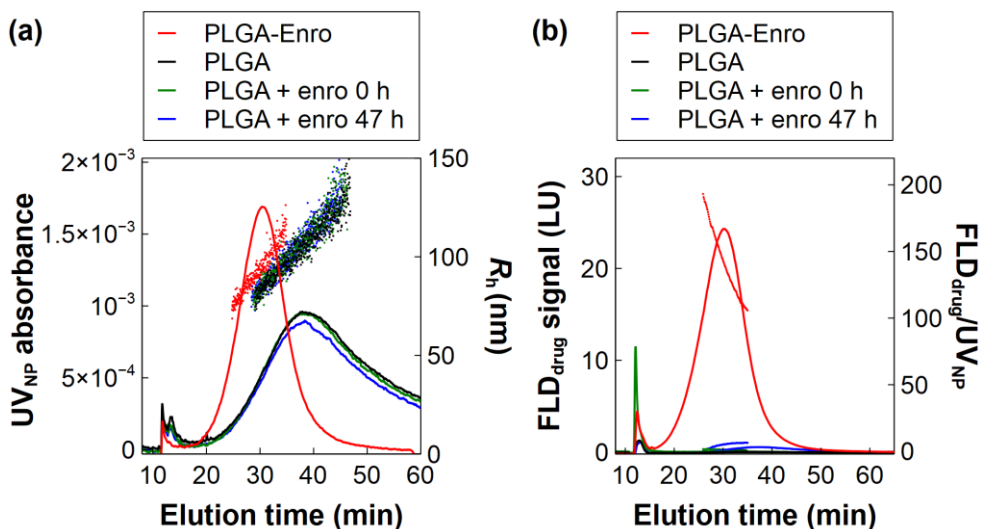
Figure B.5. AF4-UV$_{NP}$ (a, solid traces) and AF4-FLD$_{drug}$ (b, solid traces) chromatograms, R_h (a, scatter points), and FLD$_{drug}$/UV$_{NP}$ ratios (b, scatter points) of synthesized NPs and a physical mixture of PLGA + enro.

B.9 Characterization of Entrapped Drug in PLGA-Enro NPs by AF4 with UV-Vis or Fluorescence Detection

Spectral data are important to inspect to confirm the presence of a strong signal for the desired analyte (i.e., enrofloxacin), particularly when entrapped in the PLGA matrix. Here, a UV-Vis diode array detector and fluorescence detector with full spectra capabilities produce spectra data at each chromatographic time point during the AF4 runs. Figure B.6 compares UV-Vis and FLD spectra for PLGA-Enro NPs and empty PLGA NPs injected to the AF4 channel, either without separation (i.e., no focus step or crossflow) or with separation (Table B.1). The AF4 method without crossflow was 1 min elution, 5 min elution + injection, and 1 min elution, with 0.5 mL/min and 0.2 mL/min as detector and injection flow rate, respectively. Additive spectra of the empty PLGA NPs and a dissolved enrofloxacin standard are also presented for comparison. All PLGA-Enro NP spectra were scaled relative to the empty PLGA NPs to normalize

175

for differences in injected concentration and volume, as well as differences in peak broadening (based on the total UV peak area and the UV_{NP} absorbance at 400 nm at the chromatographic time point where the spectrum was selected). The arrows in the FLD spectrum denote the peak locations for the purified PLGA-Enro NPs (412 nm), unpurified PLGA-Enro NPs (420 nm), and dissolved enrofloxacin (420 nm).

Both UV-Vis and FLD spectra demonstrate that a high proportion of the total enrofloxacin is removed with focusing or crossflow in the AF4 channel, as expected based on the high percentage of burst release. UV-Vis detection was not suitable for quantification of the remaining enrofloxacin inside the PLGA-Enro NPs because the UV absorbance attributable to the drug was low relative to the particle scattering exhibited by the PLGA NPs (Figure B.6a). Instead, the UV detector was set to $UV_{NP} =$ 400 nm (no enrofloxacin interference) for all other measurements to provide a measure of the overall PLGA NP concentration.
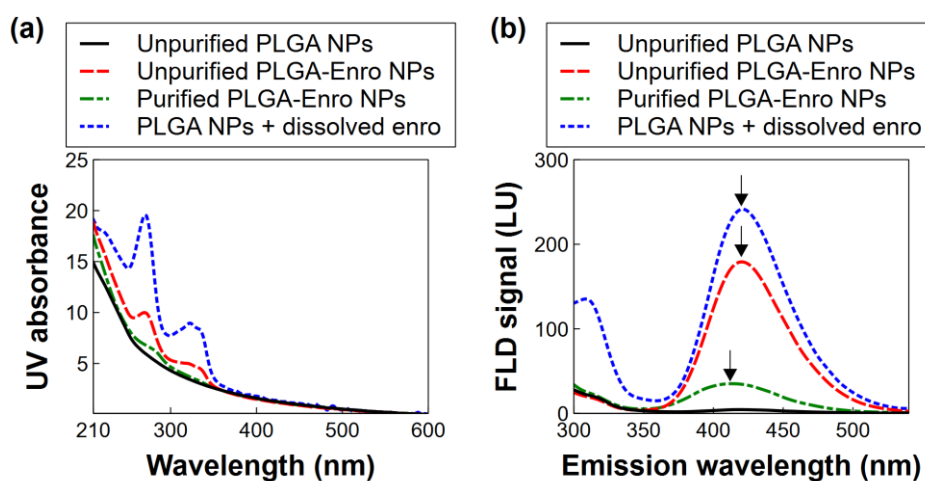

Figure B.6. UV (a) and FLD (b) spectra for unpurified empty PLGA NPs and PLGA-Enro NPs, purified PLGA-Enro NPs, and empty PLGA NPs + dissolved enrofloxacin (enro).

The FLD shows much more sensitive detection of the enrofloxacin, free of interferences from the PLGA matrix at the excitation/emission wavelengths for the drug (FLD$_{drug}$). Direct quantification of the absolute enrofloxacin concentrations in the PLGA NPs against dissolved enrofloxacin standards (i.e., to obtain mg/L concentrations rather than relative fractions of remaining enrofloxacin) would be ideal but may not be possible if the polymeric matrix affects the fluorescence of the entrapped drug. To evaluate the feasibility of direct quantification, different concentrations of enrofloxacin standards were injected through the AF4 system in elution mode only without crossflow (1 min elution, 5 min elution + injection, and 1 min elution with 0.5 mL/min and 0.2 mL/min detector flow rate and injection flow rate, respectively). To avoid saturation of the detector, the injection volume was decreased to 5 μL. To apply the calibration to estimate the loading of the PLGA-Enro NPs (50 μL injection, AF4 settings in Table B.1), the slope and intercept of the calibration curve were both multiplied by 10. The NP recovery in AF4 (discussed in the main text) was also taken into account. This measurement against external standards suggested an enrofloxacin loading of (4.0 ± 0.1) μg/mg ($n = 16$ replicates) inside the NPs, which is higher than that obtained by separating the NPs to quantify and subtracted the unentrapped drug (main text Section 3.3.1). The higher value suggests fluorescence enhancement in the PLGA matrix. Additionally, the spectral analysis shows a shift in the peak fluorescence emission wavelength for the entrapped enrofloxacin compared to dissolved enrofloxacin (Figure B.6b), which is consistent with strong interaction between PLGA and enrofloxacin and would further complicate attempts to quantify against external standards. Since direct quantification of enrofloxacin inside the NPs was not feasible, analyses were conducted

177

semi-quantitatively by taking the FLD_{drug}/UV_{NP} peak area during the release experiment relative to that of the initial NPs to eliminate the need for detector calibration.

B.10 Optimization of AF4 flow settings

To determine the optimal AF4 focus flow rate and focus duration (provided in Table B.1), the PLGA-Enro NPs were tested with three different focus flow rates (0.5 mL/min, 1.5 mL/min, and 2.0 mL/min) and two focus durations (4 min and 8 min). Figure B.7 presents the chromatograms and Table B.2 shows the retention time (RT), UV_{NP} peak area (400 nm wavelength), FLD_{drug} peak area, and the ratio of FLD_{drug}/UV_{NP} peak areas for the void peak, main (NPs) peak, and the retained peak. As noted in the main text, the UV_{NP} area at 400 nm and FLD_{drug}/UV_{NP} peak area can be representative of the concentration of NPs and the loading of enrofloxacin inside the NPs, respectively.
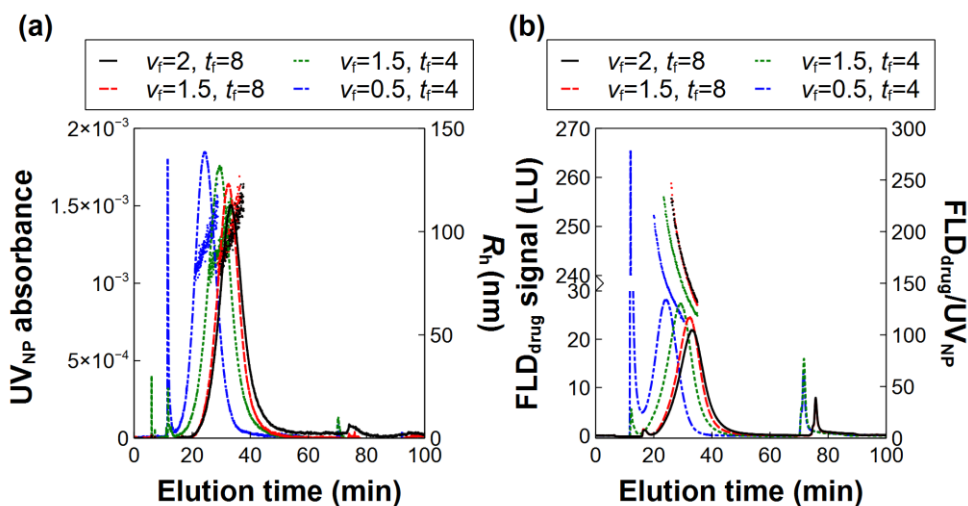
Figure B.7. AF4-UV_{NP} and AF4-FLD_{drug} chromatograms, R_h, and FLD_{drug}/UV_{NP} ratios of PLGA-Enro NPs (0.5 g/L as NPs in PBS) obtained with different focus flow rates (v_f) and focus duration (t_f)).

Table B.2. Effect of AF4 focus flow rates (v_f) and focus durations (t_f) on separation efficiency and recovery.

Method Settings		Void peak			Main peak				Retained peak		
t_f (min)	v_f (mL/min)	RT (min)	UV area (mAU·s)	FLD area (LU·s)	RT (min)	UV area (mAU·s)	FLD area (LU·s)	FLD/UV area (LU/mAU)	RT (min)	UV area (mAU·s)	FLD area (LU·s)
8	2	10 to18	5.9	1.4×10^2	18 to 65	9.7×10^2	14.4×10^3	14.9	65 to 100	16.8	1047.2
8	1.5	10 to 18	1.0	1.4×10^2	18 to 65	9.7×10^2	15.0×10^3	15.4	65 to 100	5.6	1041.3
4	1.5	10 to 13	9.1	3.7×10^2	13 to 60	11.0×10^2	17.7×10^3	16.1	60 to 100	26.9	1883
4	0.5	10 to 13	47	92.7×10^2	13 to 60	10.4×10^2	16.4×10^3	15.8	60 to 100	8.9	1682

B.11 UV-Vis and FLD Spectra of PLGA-Enro NPs during AF4 Measurements of Drug Release

UV-Vis and FLD spectra (Figure B.8) were inspected in the NPs to confirm the presence or release of enrofloxacin during the release experiments. The FLD spectra (Figure B.8b) show clear release from the NPs at 30 °C and 37 °C. The UV-Vis spectra also show loss of the weak enrofloxacin signal at the higher temperatures (Figure B.8a) but affirm that the enrofloxacin signal is too low relative to the NP scattering signal to quantify by UV-Vis.
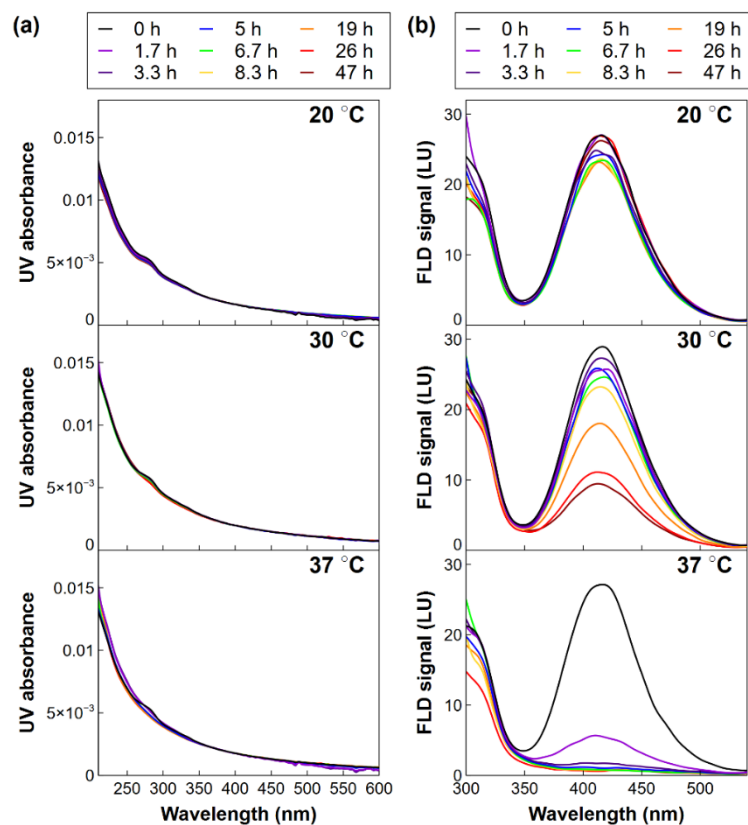
Figure B.8. UV-Vis spectra (a) and FLD spectra (b) of PLGA-Enro NPs (0.5 g/L NPs in PBS) at the peak maximum in the NP chromatograms (Figure 3.3)

B.12 Release Profiles for PLGA-Enro NPs

Release profiles are presented in Figure 3.4 as a % of the total drug (entrapped + burst). Here, the raw analysis of $(C/C_0)_{entrapped}$ by AF4 and $C_{d,outer}$ in the dialysate are presented (Figure B.9).
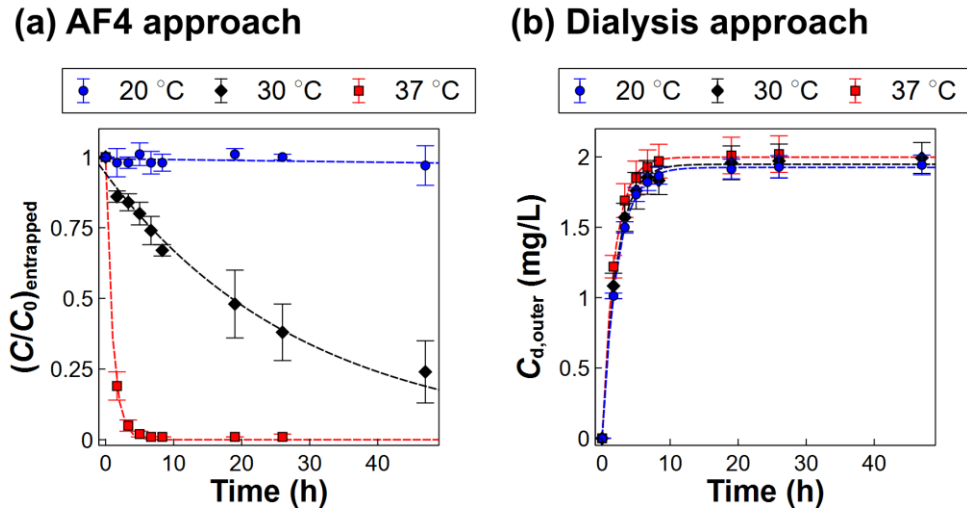
Figure B.9. Release profiles of PLGA-Enro NPs by AF4-FLD (a) and dialysis (b). The AF4 release profile was obtained by normalizing the ratio of FLD_{drug}/UV_{NP} peak areas at each release time to that at time zero.

B.13 Diffusion Model to Evaluate Drug Release Profiles for the Unpurified PLGA-Enro NPs

A diffusion model was applied that considers drug in three populations (Figure B.10), entrapped drug inside the NPs ($C_{entrapped}$) dissolved drug outside the dialysis device ($C_{d,outer}$), and dissolved drug inside the dialysis bag ($C_{d,inner}$). Diffusion rates from the polymeric NPs (k_p) and across the dialysis membrane (k_d) are both considered.
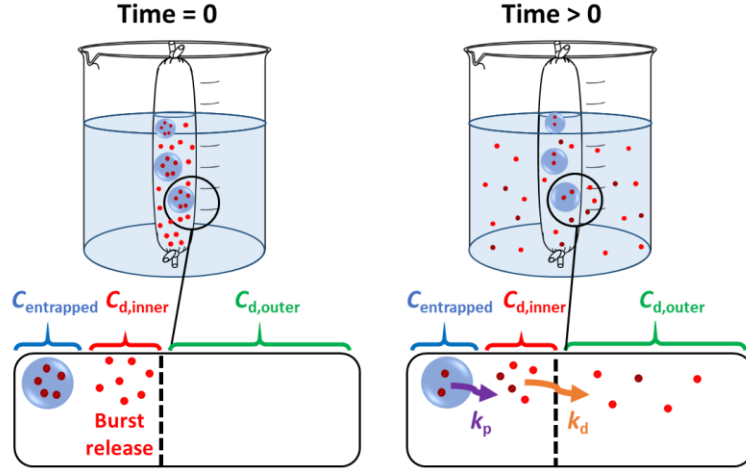
Figure B.10. Schematic of dialysis setup and defined regional concentrations and diffusion rates.

The proposed model to predict $C_{\text{entrapped}}$, $C_{\text{d,inner}}$, and $C_{\text{d,outer}}$ (Equations B.2 to B.4) is derived from Fick's law for homogeneous drug in each compartment and non-sink conditions:

$$\frac{d(xC_{\text{entrapped}})}{dt} = -k_{\text{p}}(xC_{\text{entrapped}} - C_{\text{d,inner}}), \tag{B.2}$$

$$\frac{dC_{\text{d,inner}}}{dt} = \frac{k_{\text{p}}}{x}(xC_{\text{entrapped}} - C_{\text{d,inner}}) - k_{\text{d}}(C_{\text{d,inner}} - C_{\text{d,outer}}), \tag{B.3}$$

and

$$\frac{dC_{\text{d,outer}}}{dt} = \frac{k_{\text{d}}}{y}(C_{\text{d,inner}} - C_{\text{d,outer}}). \tag{B.4}$$

Note $C_{\text{entrapped}}$ is defined here as the mass of enrofloxacin entrapped in the NPs divided by the total solution volume in the dialysis device ($V_{\text{inner}} = 1$ mL), while the driving force for diffusion in Fick's law requires the local concentration in the NPs (i.e., mass of enrofloxacin divided by volume of PLGA NPs, $V_{\text{NPs}} = m_{\text{NPs}}/\rho_{\text{NPs}}$, where m_{NPs}

and ρ_{NPs} are the mass and density, respectively of PLGA). Therefore, $C_{entrapped}$ is adjusted by a factor x representing V_{inner}/V_{NPs} as

$$x = \frac{V_{inner}}{V_{NPs}} = \frac{V_{inner}}{\frac{m_{NPs}}{\rho_{NPs}}} = \frac{1 \text{ mL}}{\frac{(7.5 \times 10^{-3}) \text{ g}}{\left(1.34 \frac{g}{mL}\right)}} = 178.7. \qquad \text{(B.5)}$$

The mass flux of entrapped drug to the inner dialysis solution is also divided by x in the model to obtain $C_{d,inner}$, with the mass and density of PLGA NPs used to determine V_{NPs}. Similarly, y is the ratio of the solution volume in the reservoir (V_{outer} =120 mL) to V_{inner} and is used to obtain $C_{d,outer}$ from the mass flux of drug leaving the inner dialysis solution.

Experimental values for $C_{d,outer}$ were obtained directly by HPLC analysis on the dialysate (Figure B.9b), and $C_{entrapped}$ from the AF4 analysis (Figure B.9a) (assuming an initial entrapped concentration of 1.9 µg/mg from the main text Section 3.3.5). The experimental $C_{d,inner}$ value was computed by mass balance as in

$$m_{total} = C_{entrapped} V_{inner} + C_{d,inner} V_{inner} + C_{d,outer} V_{outer}, \qquad \text{(B.6)}$$

where m_{total} is the total measurable released mass, determined as the summed concentrations released in the two-stage dialysis experiment at 20 °C (to measure the burst release) and 37 °C (to measure the entrapped release).

To minimize the number of fitting parameters and reduce the risk of overfitting the model, k_d for each temperature was measured by fitting first-order rate constants to the data from control experiments for enrofloxacin diffusion through the dialysis membrane. Comparing the dialysis rate of pure enrofloxacin solutions to that after spiking into an empty PLGA NP suspension showed a delay due to matrix effects of the

NP excipients (Figure B.11), so the dialysis rates of the spiked samples were used as k_d

for the PLGA-Enro NP release models.
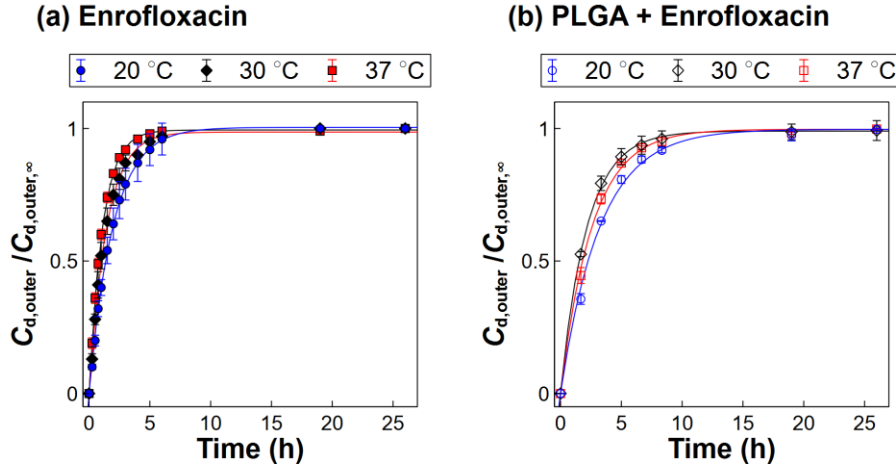
Figure B.11. Release profile of enrofloxacin (249 mg/L) in the dialysate, for pure drug in PBS (a) or drug spiked into 7.5 g/L of empty PLGA NPs in PBS (b). The lines are the first-order model fits to obtain k_d.

Finally, using the PLGA-Enro NP release data in Figure B.9, the best-fit value

of k_p was then obtained by minimizing the sum of squared errors between the predicted

$C_{entrapped}$, $C_{d,inner}$, and $C_{d,outer}$ (Equations B.2 to B.4) and the experimental values across

all time points measured. The best-fit models are presented in Figure B.12 and rate

constants in Table B.3.
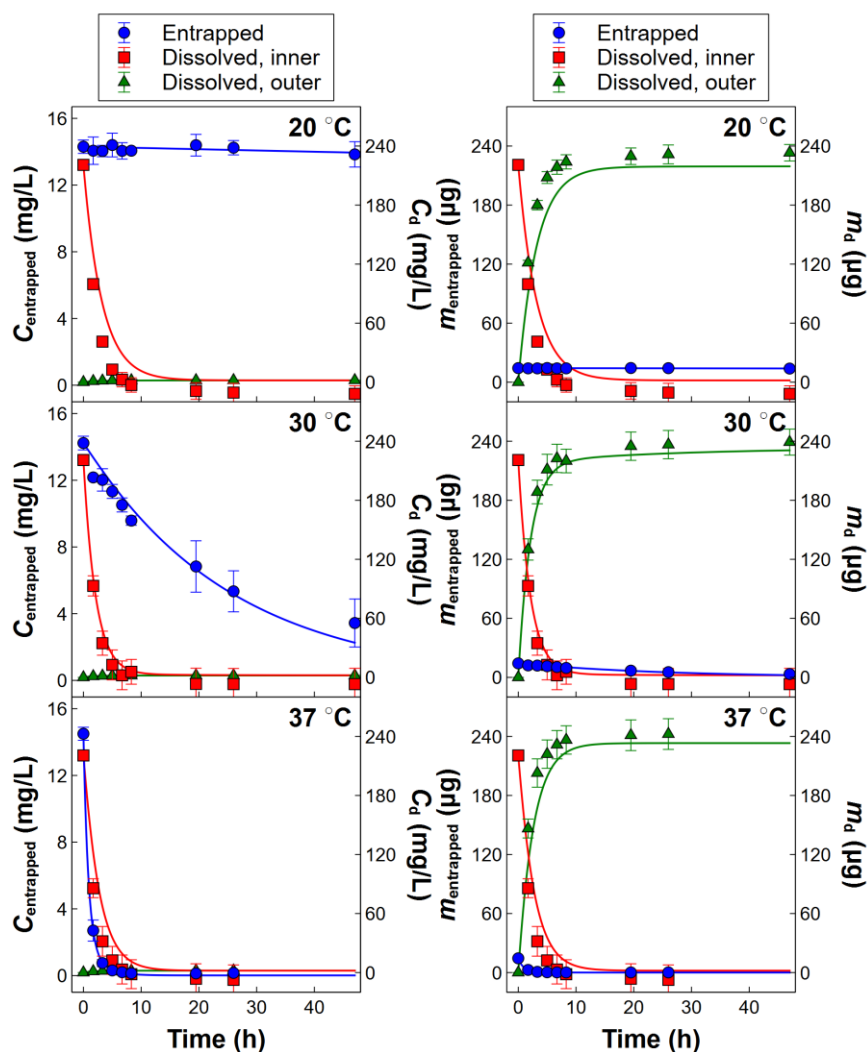
Figure B.12. Experimental results (points) and model fits (lines) for the distribution of enrofloxacin between three populations (denoted in Figure B.10), reported on a concentration (a) or mass (b) basis.

Table B.3. Rate constants obtained from model fitting of the AF4 and dialysis data.

T (K)	$k_{apparent,AF4}$ (h^{-1})	$k_{apparent,dialysis}$ (h^{-1})	k_p (h^{-1})	k_d (h^{-1})
293	0.0010 ± 0.0005	0.45 ± 0.01	0.001 ± 0.001	0.31 ± 0.01
303	0.06 ± 0.01	0.48 ± 0.06	0.04 ± 0.01	0.47 ± 0.01
310	1.0 ± 0.1	0.55 ± 0.02	1.2 ± 0.2	0.39 ± 0.02

185

B.14 Release Profile for Purified PLGA-Enro NPs

Release experiments were conducted on purified PLGA-Enro NPs at 30 °C to explore the impact of the burst release and affirm AF4 is selective to only the entrapped drug (Figure B.13).
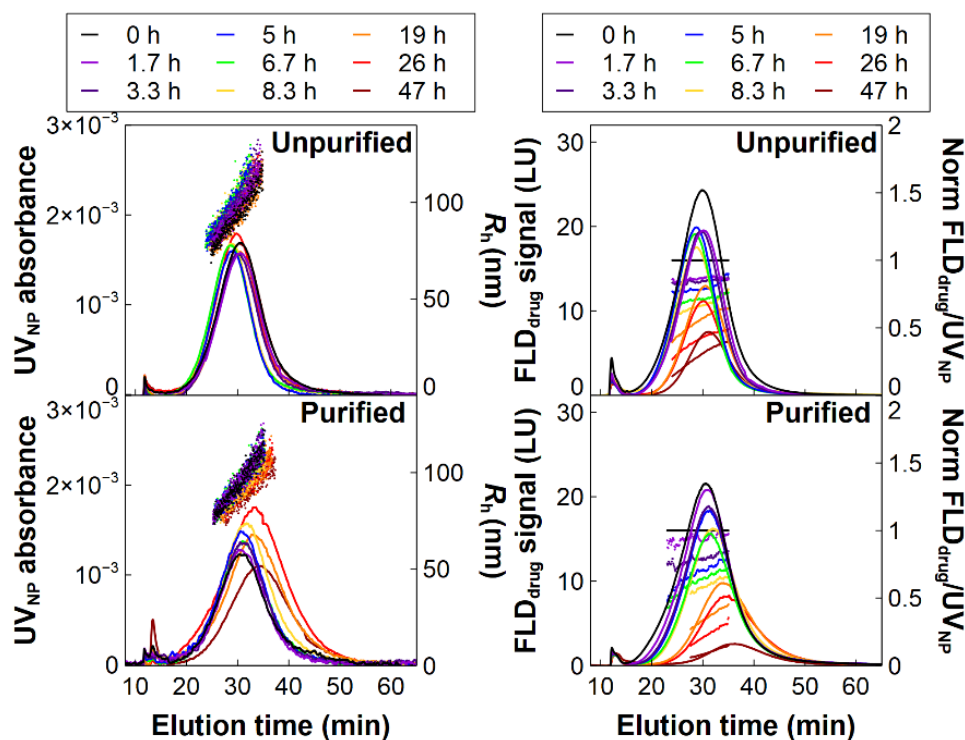
Figure B.13. AF4-UV_{NP} and AF4-FLD_{drug} chromatograms, R_h, and FLD_{drug}/UV_{drug} ratios relative to time 0 of the unpurified and purified PLGA-Enro NPs for release experiments at 30 °C.

B.15 Size Distributions and Shape Factors Obtained from AF4 with Light Scattering Analysis

NP size distributions were obtained during the AF4 measurement using online dynamic light scattering (DLS) and compared to the hydrodynamic radius, R_h, measured on batch DLS samples (Figure B.14a). The ASTRA software (v. 7.3.2.19) from Wyatt Technology (Santa Barbara, CA, USA) was utilized to analyze the online data, with

autocorrelation data at long delay times $> 7 \times 10^{-4}$ s excluded in the regularization fitting (DYNALS 2.0 algorithm) to eliminate shoulders in the autocorrelation function (which can be artifacts from sample flow through the detector). The Zetasizer software (v. 7.13) from Malvern (Malvern Panalytical Inc., Malvern, UK) was used to obtain the z-average R_h from a cumulants fit of the batch data. Online DLS measurements were slightly lower than batch DLS measurements. In batch measurements, scattering from large particles can mask the scattering from small particles, whereas AF4 provides size separation of the NPs to produce better-resolved, more accurate size distributions. Additionally, the exclusion of the larger NPs during the online DLS analysis (considering the mean of the R_h values across full width at half maximum (FWHM) of the DLS count rate peak)[2] can contribute to the lower size.

Coupling multi-angle light scattering (MALS) and DLS provides additional information on the shape of the NPs. The shape factor (ρ) is the ratio of the radius of gyration (R_g) (obtained by MALS) to R_h (obtained by online DLS) (Figure B.14b). All MALS detectors were calibrated using bovine serum albumin (BSA) monomer. The R_g was calculated using the data from at least 13 angles from the MALS (where lower angles were excluded when they showed deviation from the fitted model, e.g., due to high sensitivity to the existence of any debris). A 2nd order Berry model was used,[3-5] since it has been recommended as a robust method [195] and, based on the findings of Andersson et al. for polymeric particles with R_g around 50 nm, the Berry method with fit order ≥ 2 results in low relative error in measured R_g (less than 0.3%).[4] The reported R_g is the average value across the FWHM of the 90° MALS detector.
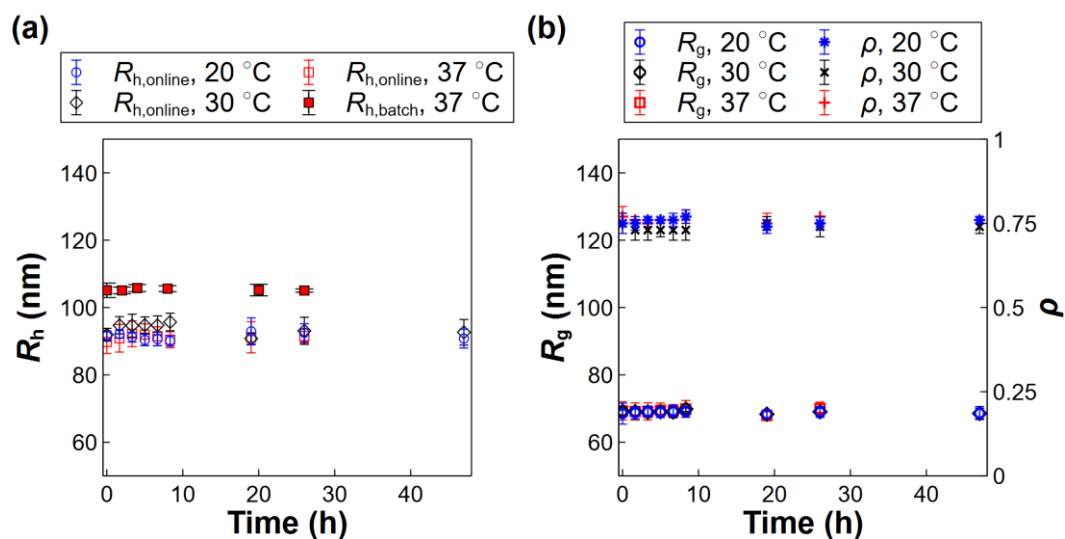
Figure B.14. Hydrodynamic radius, R_h, of PLGA-Enro NPs (0.5 g/L NPs in PBS) obtained by batch and online DLS (a), as well as radius of gyration, R_g, and shape factor, ρ.

**B.16 Zeta Potential Measurements for PLGA-Enro NPs**

Zeta potential was measured on the NPs during the release experiments (Figure B.15) to evaluate whether changes in AF4 elution time correlate to any changes in zeta potential. Zeta potential measurements were conducted in folded zeta capillary cells (DTS 1070, Malvern) on a Malvern Zetasizer Nano ZS instrument on the same samples for batch DLS analysis (Figure B.14). Zeta potential was computed from the electrophoretic mobility using the Smoluchowski model.
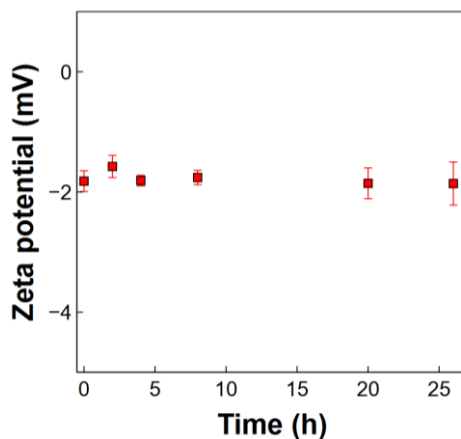
Figure B.15. Zeta potential of PLGA-Enro NPs (0.5 g/L NPs in PBS).

B.17 Size-Dependent Drug Release from PLGA-Enro NPs

Figure B.16 shows the matching of the release rate constant with each size of NP eluting at each time point on the AF4 chromatograms (see Figures 3.3 and 3.7a in the main text), to clarify how size-dependent release profiles were acquired for Figure 3.7b.
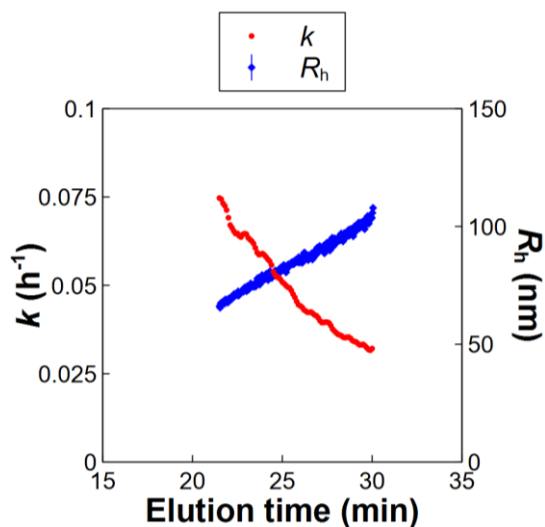
Figure B.16. Drug release rates (k) and hydrodynamic radius (R_h) across the AF4 chromatograms for the PLGA-Enro NPs at 30 °C.

189

APPENDIX C. SUPPORTING INFORMATION FOR CHAPTER 4

C.1 Literature review on coumarin 6 (C6) release from poly (lactic-*co*-glycolic acid) PLGA NPs

Table C.1. Literature review on coumarin 6 (C6) release from PLGA NPs

Synthesis Conditions[a] and Total C6:PLGA Ratio in the Synthesis[b]	Loading (L) and entrapment efficiency (EE)	Release Behavior	Reference
• First emulsion: 2 mg protein in 50 μL of water + 2 mL of PLGA (100 mg/mL) and 50 μL of C6 (1mg/mL) in ethyl acetate • Second emulsion: 4 mL of PVA (1%, w/v) + first emulsion, then dilution with 90 mL PVA solution (0.3%, w/v) • Total C6:PLGA ratio = 0.25 μg/mg	• L = 0.025 ± 0.009 % (w/w) • EE = 100 %	• <1% burst release during the first day • Sigmoidal release up to 100% over 45 days due to polymer degradation or erosion	Corrigan et al.[270]
• Organic phase: 90 mg PLGA in 3 mL of chloroform containing 50 μg of C6 (0.5 mg/mL) • Aqueous phase: 12 mL of PVA (2%) • Total C6:PLGA ratio = 0.55 μg/mg	• L = 0.05 % (w/w)	• Rapid initial release within 30 min and further 0.32% release within 24 h	Qaddoumi et al.[271]; Synthesis reported in Davda et al.[290]

Table C.1. Continue. Literature review on coumarin 6 (C6) release from PLGA NPs

Synthesis Conditions[a] and Total C6:PLGA Ratio in the Synthesis[b]	Loading (L) and entrapment efficiency (EE)	Release Behavior	Reference
• Organic phase: 500 mg PLGA in 10 mL methylene chloride + 0.1% C6 • Aqueous phase: 50 mL 0.2% PVA • Total C6:PLGA ratio = 1 µg/mg (assuming 0.1% C6 relative to PLGA)	• L = 0.1 % (w/w) nominal loading • EE = 70-80 %	• Transport buffer: No significant release within 3 h • Dialysis set-up with liposome dispersion in the receiver: Around 35 % within 3 h • Direct contact with liposomes: 50 % release within 3 h	Pietzonka et al.[256]
• 30 mg of PLGA + 60 µg of C6 in - 1 mL of ethyl acetate + 5 mL PVA (3% (w/v)) (for 80 nm NPs) - or in 1 mL dichloromethane-ethyl acetate (7:3) + 5 mL PVA (3% (w/v)) (for 150 nm NPs) - or in 1mL dichloromethane + 8 mL of PVA (5 %(w/v)) (for 300 nm NPs)	• EE = 89.7 % (for 80 nm NPs) • EE = 96.61 % (for 150 nm NPs) • EE = 92.80 % (for 300 nm NPs)	N.D.	Cai et l.[291]

Table C.1. Continue. Literature review on coumarin 6 (C6) release from PLGA NPs

Synthesis Conditions[a] and Total C6:PLGA Ratio in the Synthesis[b]	Loading (L) and entrapment efficiency (EE)	Release Behavior	Reference
Then diluted with a 0.5% (w/v) PVA • Total C6:PLGA ratio = 2 µg/mg			
• PLGA and C6 (0.05% (w/v)) in DCM • PVA (or vitamin E TPGS)	N.D.	• 3.75% and 2.55% release from the TPGS and PVA NPs, respectively, over 24 h	Yin Win et al.[292]
• Polyvinyl alcohol or Mowiol 4-88 and magnesium acetate tetrahydrate, ratio 1 to 3 with PLGA (20% w/w) and C6 (1%) in acetone • Total C6:PLGA ratio = 50 µg/mg	N.D.	N.D.	Eley et al.[293]
• Organic phase: BSA (300 µl, 10 % w/v) + 90 mg PLGA + 50 µg C6 in 3 mL chloroform • Aqueous phase: 12 mL PVA (0.5 to 5 % w/v) • Total C6:PLGA ratio = 0.55 µg/mg	N.D.	N.D.	Sahoo et al.[294]

Table C.1. Continue. Literature review on coumarin 6 (C6) release from PLGA NPs

| Synthesis Conditions[a] and Total C6:PLGA Ratio in the Synthesis[b]	Loading (L) and entrapment efficiency (EE)	Release Behavior	Reference
• 1 mg of C6 in 1.25 ml of 1% PLGA-DCM solution, + 12.5 ml of PVA (0.3% (w/v)) (for 200 nm NPs) • 1.5 mg of C6 in 1.25 ml of 15% PLGA-DCM + 12.5 ml of PVA (0.3% (w/v)) (for 1200 nm particles) • Total C6:PLGA ratio = 80 µg/mg	N.D.	N.D.	Patel at al.[253]

[a]As reported, [b]Computed, N. D. not determined

**C.2 Batch Total Organic Carbon (TOC) Measurements**

To quantify the carbon concentration of the PVA standards, we initially attempted to use an alternative TOC analyzer (TOC-L, Shimadzu, Kyoto, Japan). The measurements in this instrument are based on sample combustion over a Pt catalyst at 680 °C. However, the catalyst was found to be unsuitable for PVA analysis; reported C concentrations were lower on standards with higher concentrations (e.g., 200 mg/L PVA, measured as 0.5 mg C/L) than those with lower concentrations (e.g., 100 mg/L PVA, measured as 30.9 mg C/L). Therefore, all batch TOC measurements were performed using the batch mode of the same TOC detector (Sievers M9-SEC portable TOC analyzer, Suez, Trevose, PA, USA) as used in the online mode attached to AF4.

C.3 Characterization of the Synthesized PLGA-C6 NPs

The transmission electron microscobe (TEM) image, and differential scanning calorimetry (DSC) were conducted and analyzed by Dr. Carlos E. Astete and Dr. Rafael Cueto.
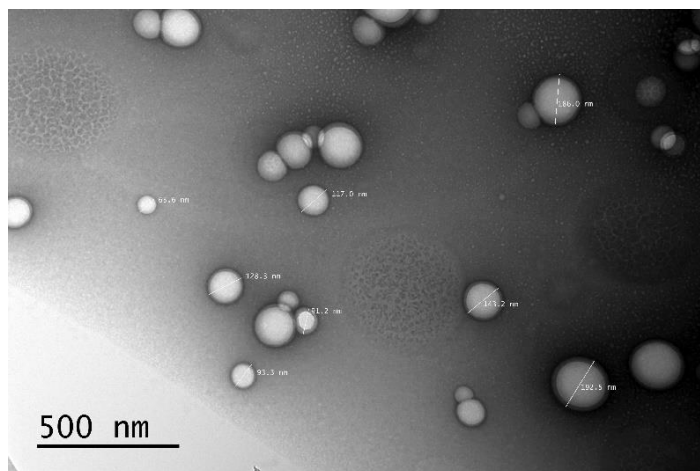
Figure C.1. Transmission electron microscope (TEM) image of PLGA-C6 NPs.
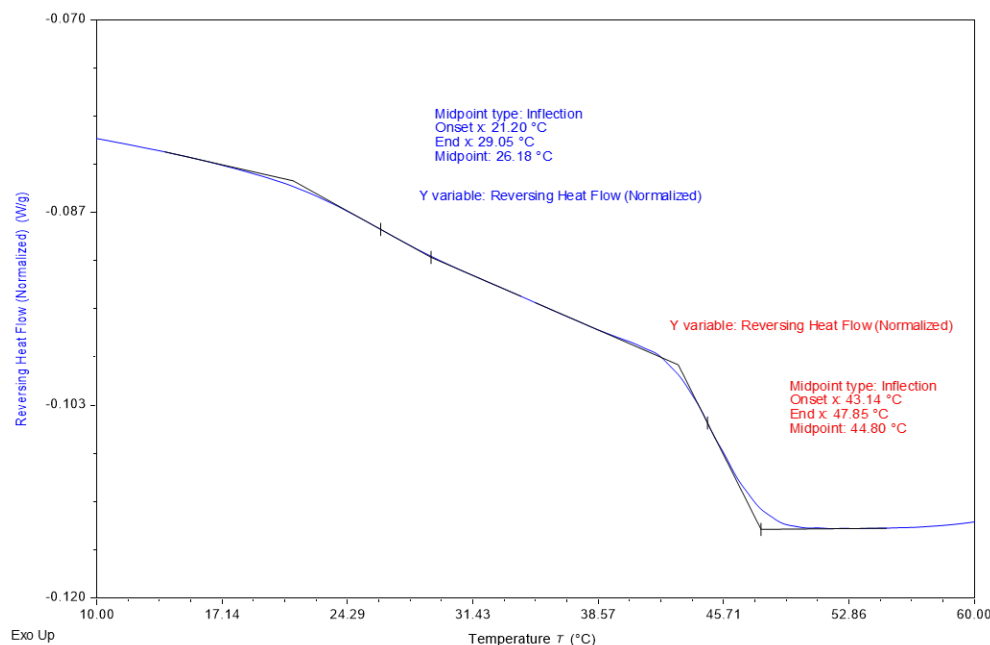
Figure C.2. Determination of T_g from the second heating differential scanning calorimetry (DSC) plot of PLGA-C6 NPs. Tg (inflection point method), onset point, and end point are 44.8 °C, 43.14 °C , and 47.85 °C, respectively.

C.4 Effect of Container Material on Release Profile

Our initial results obtained for the C6 release profile from the NPs revealed a significant effect of container material on the release behavior (under similar conditions, i.e., 0.25 g/L of NPs in PBS at 37 °C). We observed almost no drug release from the NPs if held in polytetrafluoroethylene (PTFE) or glass containers for the release experiment, in contrast to observing a slow release profile when polypropylene centrifuge tubes were used. Release can be limited by the low aqueous solubility of C6, and hence sink conditions are not achieved in containers with low sorption. This was supported by control experiments (C6 only at 0.25 mg/L in PBS) showing minimal dye adsorption onto glass, as opposed to decreasing dye concentrations due to sorption onto the polypropylene tubes. The disposable plastic centrifuge tubes were therefore used to acquire drug release profiles under sink conditions. Note that dialysis was also tested,

and similar release profiles were achieved in the polypropylene centrifuge tube. Furthermore, when collecting samples from the plastic tubes, the dissolved C6 concentration measured in the supernatant after pelleting the NPs was typically < 10 µg/L, further indicating that losses of dissolved C6 occurred and sink conditions were achieved during the experiments.
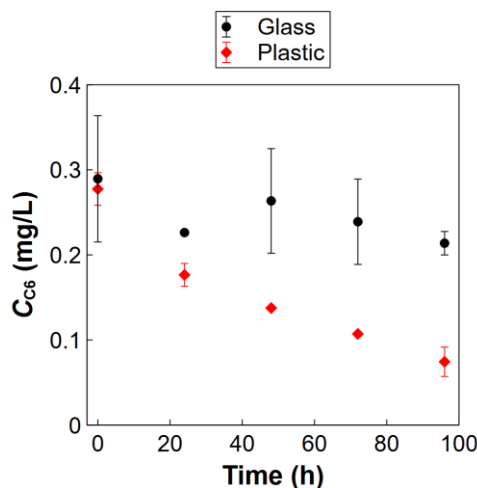
Figure C.3. Adsorption of C6 (0.25 mg/L in PBS) onto glass or plastic container within 96 h.

### C.5 Optimized AF4 Flow Parameters

The AF4 flow parameters used here were the same as those optimized in our previously published work. The detector flow rate and the injector flow rate were 0.5 and 0.2 mL/min, respectively. The injection volume was 100 µL. Table C.2 presents the crossflow rate and duration of each separation step.

Table C.2. Crossflow rates and duration of each separation step in the AF4 method

Mode	Duration (min)	Crossflow rate (mL/min)
Elution	6	0.15
Focus	1	1.5
Focus + injection	4	1.5
Elution	58	0.15
Elution + injection	15	0
Elution	6	0
Elution	10	0.15

C.6 Analysis of Size-resolved "Apparent" Dye Loading Profiles by AF4

To assess the amount of dye loading inside the polymeric NPs across different size fractions of the particles, we might attempt to take the ratio of the FLD signal (indicative of the C6 concentration) to a signal corresponding to the concentration of the PLGA at each size fraction. Using TOC or RI as the NP concentration detectors showed an increasing FLD/NP signal with increasing size, whereas dividing FLD by the raw UV signal for the NPs shows the opposite trend (Figure C.4). The values for each series are normalized to the minimum value in each data series for ease of comparison.
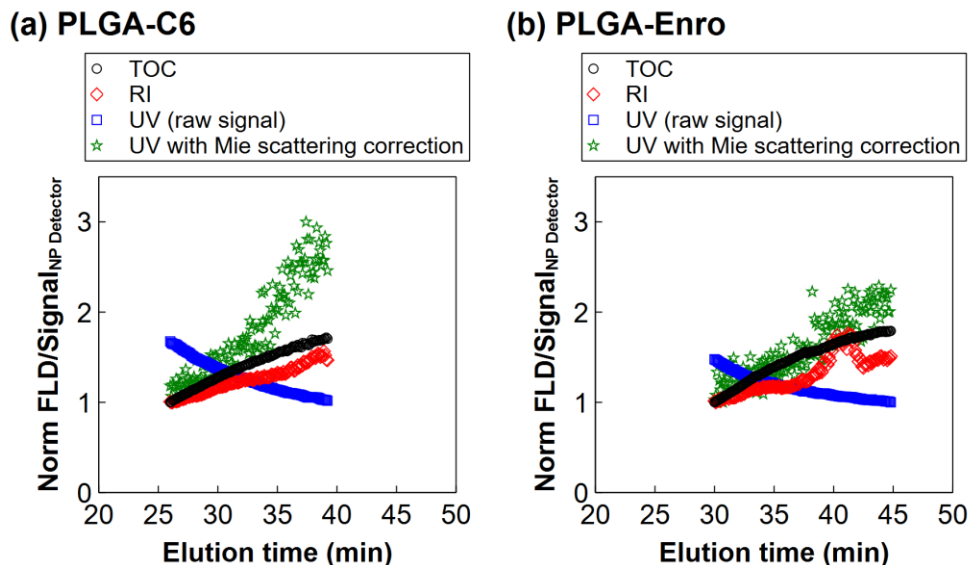
Figure C.4. The normalized ratio of FLD/Signal$_{NP\ Detector}$, by considering TOC, RI, raw UV, and UV with Mie scattering correction as the signal representing NP concentration.

The higher values of FLD/UV for the smaller (more rapidly eluting) particles was postulated to be an artifact of the fact that the UV "absorbance" signal includes scattering contributions, particularly for large NPs, which are not simply proportional to the mass concentration of the NPs. To evaluate this hypothesis, a UV signal correction approach was taken to normalize the UV signals to eliminate the influence of size and leave only mass concentration contributions to the measured signal. First, the AF4-UV "absorbance" signal for the eluting PLGA NPs is assumed to represent primarily scattering with minimal contribution of true absorbance, i.e., the "absorbance" may be more correctly termed "turbidity," τ, where τ is approximately equal to the ratio of scattered intensity (I_s) and incident light intensity (I_0), i.e., $\tau \approx I_s/I_0$ for dilute samples where $I_s \ll I_0$. To account for and normalize the influence of size on the scattering intensity, the Malvern Zetasizer software (Version 7.13, Malvern

Panalytical Inc., Malvern, UK) was used to compute the Mie scattering function as relative scattering per unit volume of the PLGA NP (nm^3) for particles ranging from 1 nm to 130 nm radius (covering the size ranges measured by AF4-DLS across the full width half maximum of the AF4-DLS peak). The medium refractive index was set to 1.33 for aqueous medium, wavelength to 350 nm (the same wavelength applied in the AF4-UV analysis), scattering angle of 0° representing scattering toward the UV detector (which measures the forward transmitted light through the UV flow cell), and the real and imaginary particle refractive index of 1.46 and 0, respectively, for PLGA.[295]

An increase in forward scattering with particle size is clearly observed, as expected (Figure C.5). The exported Mie scattering function was normalized to the maximum value for the largest size particle to obtain size normalization factors (Figure C.5), and fitted with a power law function for convenient computation of normalization factors given the measured R_h values from the AF4-DLS data. The raw UV "absorbance" data were then divided by the normalization factor to obtain corrected UV signals that are expected to be proportional the mass concentration of the particles without the influence of size on the Mie scattering function. After applying this correction, the FLD/UV ratios show a similar trend to FLD/TOC; furthermore, the FLD/RI analysis also confirms this trend (Figure C.4).
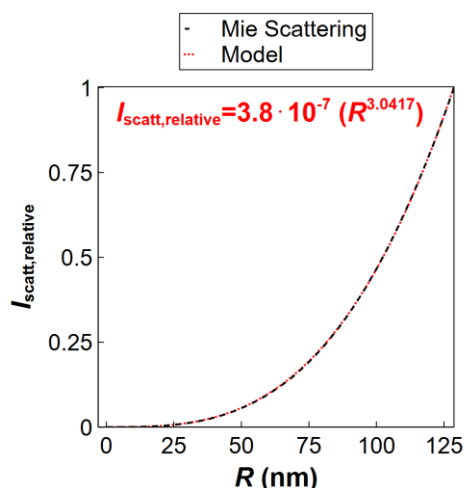
Figure C.5. Relative scattering per unit volume normalized to the maximum in the size range of interest for the PLGA NPs computed in the Malvern Zetasizer Mie scattering calculator.

The reason for the observed trend of increasing FLD signal/PLGA concentration with increasing particle size is not clear. Possible reasons include a truly higher C6 loading in the larger particles, or other measurement artifacts on the FLD signal itself (rather than the NP concentration signals) that may be size-dependent, including fluorescence quenching or enhancement, or inner filter and scattering effects. Note that while inner filter corrections can be applied given true absorbance measurements and path lengths for the FLD flow cell, scattering influences on the measured FLD signal are highly complicated and currently deemed impossible to predict.[296] Hence, no further corrections were attempted.

C.7 Evaluation of NP Size and Shape during the Release Experiments

Possible NP transformations were evaluated through size and shape analysis over the duration of the C6 release experiments (Figures C.6 and C.7). The analysis for shape

factor was performed in ASTRA (v. 7.3.2.19) from Wyatt Technology (Santa Barbara, CA, USA), with the 2nd order Berry model for R_g calculations.
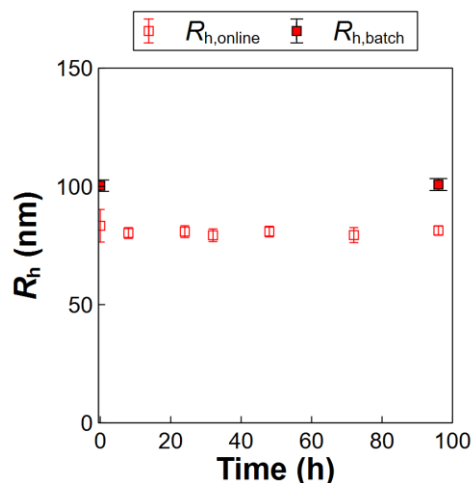
**Figure C.6.** Hydrodynamic radius (R_h) obtained by batch and online DLS measurements.
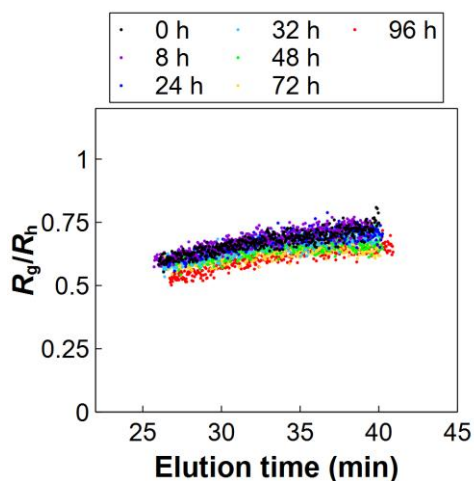
Figure C.7. The ratio of radius of gyration (R_g) to R_h, i.e., the shape factor, obtained for AF4 measurements with online multi angle light scattering (MALS) and DLS detectors.

C.8 LC-UV-QTOF for C6 Release Validation and PLGA Oligomer Analysis

NP samples collected during the release experiments were pelleted by centrifugation and extracted into acetonitrile for LC-UV-QTOF analysis. The UV and TIC chromatograms are presented in Figure C.8. The C6 eluted at 16 min in the UV

chromatogram and slightly later in the TIC due to the tubing delay between detectors. Other major peaks observed in the TIC are attributable to PLGA in the extracts (as affirmed by comparison against measured stock PLGA solutions).
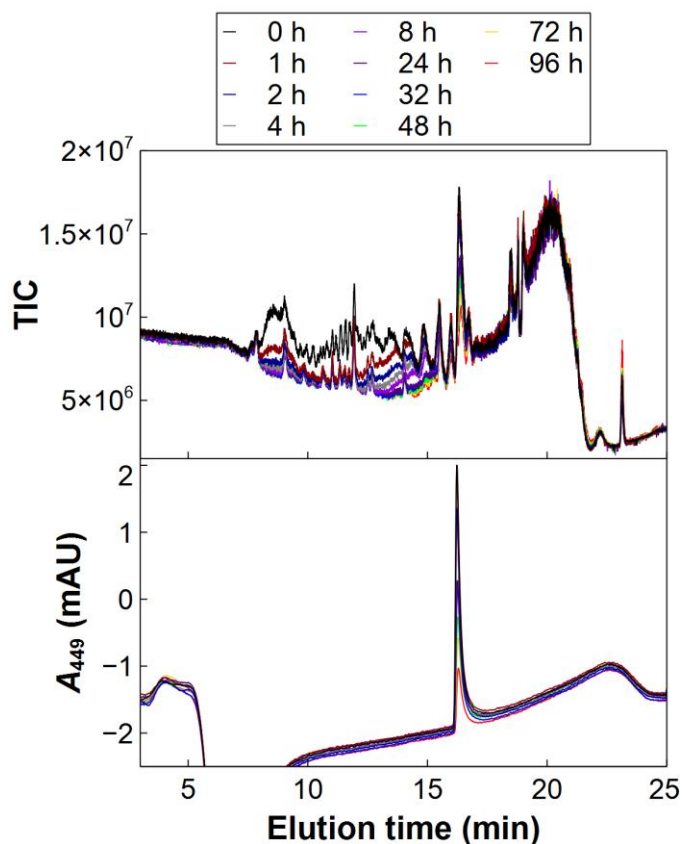

Figure C.8. The total ion count (TIC) and UV chromatograms for acetonitrile extracted PLGA-C6 NPs collected during the release experiments in PBS at 37 °C.

Because losses of PLGA-related peaks were observed, further evaluation of these species was undertaken. First, untargeted compound discovery was performed using Agilent MassHunter Mass Profiler 10.0.1 (Agilent, Santa Clara, CA, USA) – when plotting the extracted species by their MW vs. retention time (RT), polymer series show clear patterns representing additions of the monomer units. To obtain additional information regarding the relative composition of glycolide (GA) or lactide (LA) in the polymers and

develop improved plots with higher information value, the data on the molecular weight, retention time, and abundance for all extracted species were exported from Mass Profiler for further processing. First, an appropriate low MW species was identified to serve as a "base" species with molecular weight m_{base} (398.0462 Da) (i.e., $m/z \approx 399$ assuming H^+ for ionization), upon which a search was conducted for a list of masses m representing all possible combinations of additions of n_{GA} glycolide units (each with mass m_{GA} of 58.0055 Da) and n_{LA} lactide units (each with mass m_{LA} of 72.0211 Da) to the base mass, i.e.,

$$m = m_{GA}n_{GA} + m_{LA}n_{LA} + m_{base}. \tag{C.1}$$

All found species in each sample were compiled into a list (thus paring the untargeted compound search from Mass Profiler to only species related to PLGA). These species were then plotted in Figure C.9, where each point represents a found species, the size of each point represents the abundance of that species, and the intensity of the red and blue color on the left and right side of the plotted circles represents n_{LA} and n_{GA}, respectively, added to the base species.
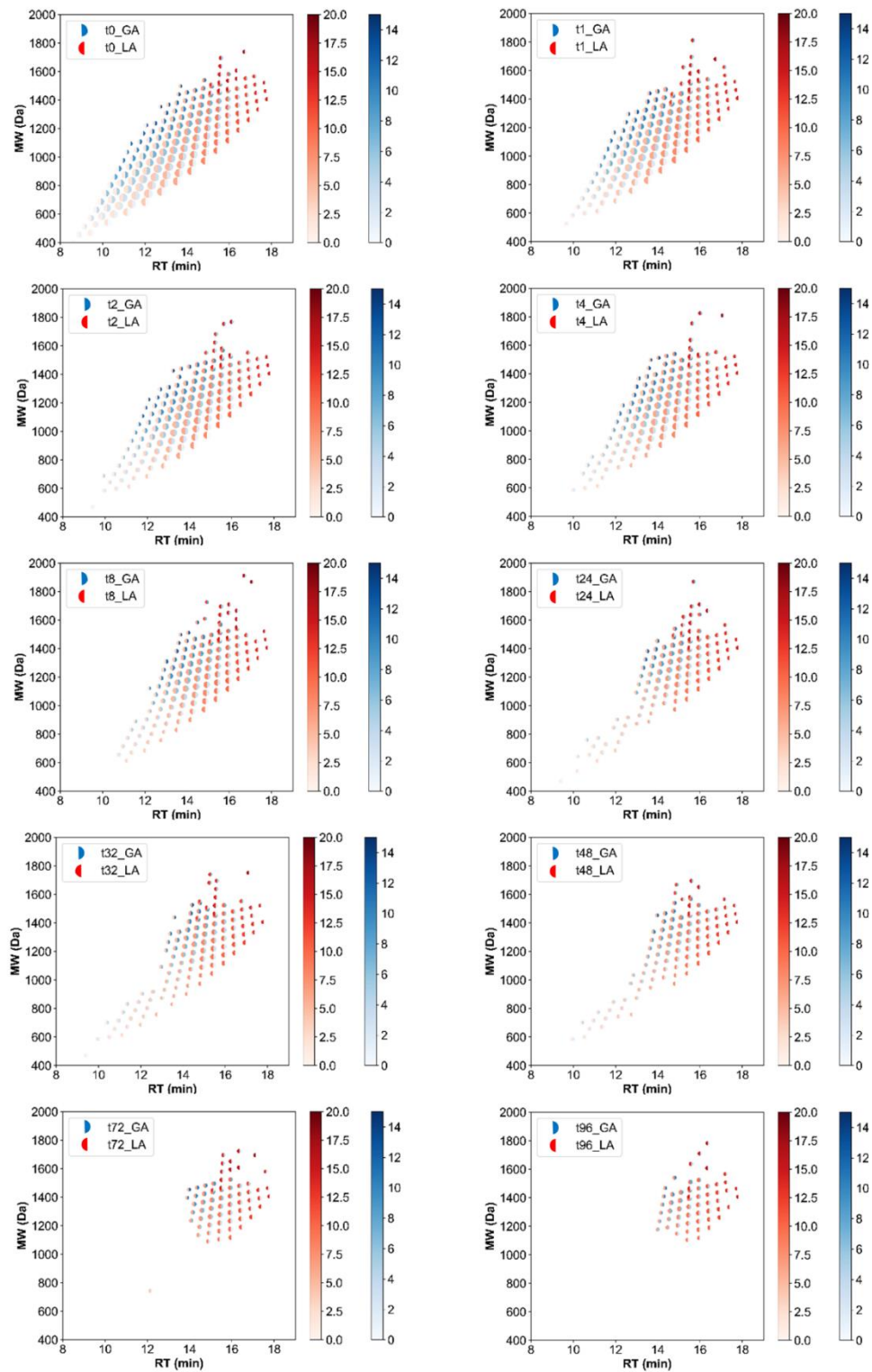
Figure C.9. Oligomeric PLGA species identified in the LC-QTOF analysis of the NPs collected during the release experiments. Colors and symbols are explained in the text above.

Species with lower MW and higher GA character showed more rapid and extensive loss. To more clearly assess the rate of loss, species were selected from a few representative regions of Figure C.9 to plot their abundance in the samples over the course of the release experiment, as shown in Figure C.10.
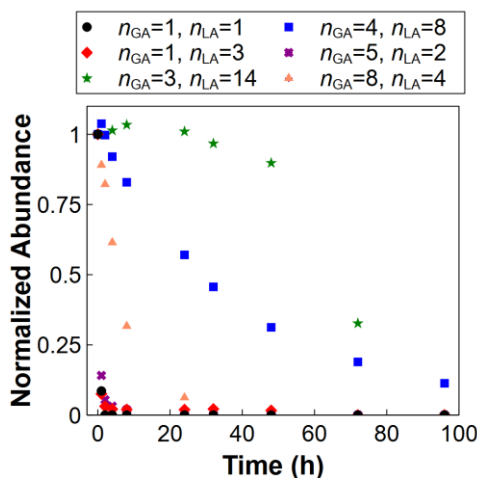
Figure C.10. Abundances of select PLGA oligomers with varying MW and degree of LA or GA character over the course of the release experiment. Abundances at each time point were normalized to that at time zero for each species.

C.9 Modeling of the Bulk Time-Resolved Release Profiles

Six different release models were fitted to the bulk C6 release profiles measured using the multi-detector AF4 approach and the LC validation measurements. We emphasize here that several of the models presented are not appropriate for release from spherical NPs, but rather are used to demonstrate the uncertainty in model selection that can be encountered when fitting release profiles *a priori* and attempting to interpret the results. For all models, best-fit parameters were obtained by minimizing the sum square

errors (SSE) between the model prediction and the experimental data across all measured time points. All best-fit models are compared to the experimental data in Figure C.11.

The first model fitted was a first-order kinetic model (Equation C.2),

$$C_t' = C_\infty'[1 - \exp(-kt)], \tag{C.2}$$

where C_t' is defined as the ratio of concentration of released drug at time t to the total initial concentration of drug loaded on the particles, C_∞' represents the ratio of the ultimate releasable drug at time infinity to the total initial concentration, and k is the first-order rate constant. In this study, both k and C_∞' were fitted (Table C.3). In Equation C.2, the bulk drug in the media is assumed to be zero at all times (perfect sink conditions), where the drug in the particles depletes over time. It is noted that the Noyes–Whitney equation[266, 297] describing the dissolution of a solid results in a mathematically equivalent model form, as shown in Equations C.3 and C.4,

$$\frac{dC_t}{dt} = \frac{DS}{Vh}(C_s - C_t) = k_{N-W}(C_s - C_t), \tag{C.3}$$

where C_t and C_s are the concentration of released drug at time t and drug solubility, respectively. D, S, V, and h are drug diffusion coefficient, the surface area of the solid, solution volume, and thickness of the diffusion layer, respectively, which can be lumped into a single parameter, k_{N-W}. Integrating Equation C.3 with $C_0 = 0$ yields

$$C_t = C_s[1 - \exp(-k_{N-W}t)]. \tag{C.4}$$

The second model applied is a radial diffusion model[238 239] for release from spherical particles (Equation C.5),

$$C_t' = C_\infty' \left[1 - \frac{6}{\pi^2} \sum_{n=1}^{\infty} \frac{1}{n^2} \exp\left(-\frac{Dn^2\pi^2 t}{R^2} \right) \right], \tag{C.5}$$

where D is the diffusion coefficient of drug transfer through the polymeric matrix, and R is the particle radius. The model was fitted for D/R^2 and C_∞ (Table C.3). For an average R of 80 nm (Figure C.11), the best-fit value of D is then $(7 \pm 6) \times 10^{-11}$ cm^2/s or $(1.8 \pm 0.9) \times 10^{-11}$ cm^2/s for the release profiles obtained by the AF4 or LC measurements, respectively.

The third model applied is the Higuchi model[259][260] for release from a planar film (Equation C.6),

$$C_t' = C_\infty' \sqrt{2DW_0 C_s t} = C_\infty' k_H \sqrt{t}, \tag{C.6}$$

where k_H is the Higuchi rate constant, W_0 is the initial drug concentration inside the matrix, and all other variables are as defined above. The main assumptions are that the initial drug concentration inside the matrix is much higher than the dye solubility ($W_0 \gg C_s$), no swelling or other changes to the matrix occur, and perfect sink conditions are maintained during the release. Here we fitted $C_\infty' k_H$ as one lumped parameter (Table C.3).

The fourth model applied is the Baker–Lonsdale model, which is based on the Higuchi model but for drug release from spherical systems (Equation C.7),

$$\frac{3}{2} \left(1 - \left(1 - \frac{C_t'}{C_\infty'} \right)^{\frac{2}{3}} \right) - \frac{C_t'}{C_\infty'} = k_{B-L} t, \tag{C.7}$$

where k_{B-L} is the Baker–Lonsdale rate constant. To fit both C_∞' and k_{B-L} (Table C.3), an initial guess was set for C_∞' to compute the left hand side (LHS) of the equation for our experimental data, and the best-fit C_∞' was optimized as that which yields the highest R^2 value for the line of best fit for the LHS versus time. The best-fit k_{B-L} was then taken as the slope of the line.

The fifth model applied is the semi-empirical Korsmeyer-Peppas model,[261] in which the concentration of released drug from the polymeric system is described by a power law function over time (Equation C.8), as in

$$C_t' = C_\infty' \, k_{\text{K-P}}(t^n),$$ (C.8)

where $k_{\text{K-P}}$ is the release rate constant and n is the diffusional exponent. This model is only applicable to the first 60% of the drug release profile. Here, we fitted $C_\infty' \, k_{\text{H}}$ as one lumped parameter (Table C.3). The n value can be interpreted for the release mode, with $n = 0.43$ representing Fickian diffusion or $0.43 < n < 1$ representing non-Fickian release mechanisms for spherical particles.[261, 298]

The sixth model applied is the Hixson–Crowell model[263] (Equation C.9),

$$\sqrt[3]{\frac{W_t}{W_0}} = \sqrt[3]{1 - \frac{C_t}{C_\infty}} = 1 - k_{\text{H-C}}t,$$ (C.9)

where W_0 and W_t are the drug concentration inside the particles at time 0 and t, respectively, and $k_{\text{H-C}}$ is the Hixson–Crowell release constant. This model is based on the dissolution of a solid drug (e.g., a tablet form), and assumes the surface decreases over time while maintain the same geometrical form. In order to fit this model to our experimental data, we rearrange the model to Equation C.10,

$$C_t' = C_\infty'[1 - (1 - k_{\text{H-C}}t)^3],$$ (C.10)

and fit the C_∞' and $k_{\text{H-C}}$ parameters (Table C.3).

Finally, we present the Hopfenberg model [264] in Equation C.11 for drug release from an eroding polymer,

$$C_t' = C_\infty' \left[1 - \left(1 - \frac{k_0 t}{A_0 a_0}\right)^n\right],$$ (C.11)

where k_0, A_0, and a_0 are the erosion constant, the initial drug concentration in the matrix, and the initial radius of the sphere, respectively. For a spherical particle, $n = 3$ and hence the model takes mathematically the same form as Equation C.10.

Table C.3. Best-fit model parameters; the fitted values are reported the average and standard deviation on fits for four experimental replicates.

| Experimental data	Model	Parameters (units)	Fitted value
AF4-FLD-TOC	First-order kinetics	k (h^{-1})	0.09 ± 0.05
		C'_∞	0.77 ± 0.05
	Radial diffusion	$\dfrac{D}{R^2}$ (h^{-1})	0.01 ± 0.01
		C'_∞	0.86 ± 0.14
	Higuchi	$C_\infty k_H$ (h^2)	0.094 ± 0.004
	Baker and Lonsdale	k (h^{-1})	0.0016 ± 0.0005
		C'_∞	0.9 ± 0.1
	Korsmeyer-Peppas	$C_\infty k_{H\text{-}P}$ ($h^{1/n}$)	0.2 ± 0.1
		n	0.3 ± 0.2
	Hixson–Crowell (or Hopfenberg)	k (h^{-1}) (or $\dfrac{k_0}{A_0 a_0}$ (h^{-1}))	0.014 ± 0.002
		C'_∞	0.77 ± 0.02
HPLC on acetonitrile extracts	First-order kinetics	k (h^{-1})	0.04 ± 0.01
		C'_∞	0.73 ± 0.08
	Radial diffusion	$\dfrac{D}{R^2}$ (h^{-1})	0.003 ± 0.001
		C'_∞	1.00 ± 0.01
	Higuchi	$C'_\infty k_H$ (h^2)	0.08 ± 0.01
	Baker and Lonsdale	k (h^{-1})	0.0007
		C'_∞	0.83
	Korsmeyer-Peppas	$C'_\infty k_{H\text{-}P}$ ($h^{1/n}$)	0.09 ± 0.04
		n	0.47 ± 0.06
	Hixson–Crowell (or Hopfenberg)	k (h^{-1}) (or $\dfrac{k_0}{A_0 a_0}$ (h^{-1}))	0.013 ± 0.004
		C'_∞	0.68 ± 0.06
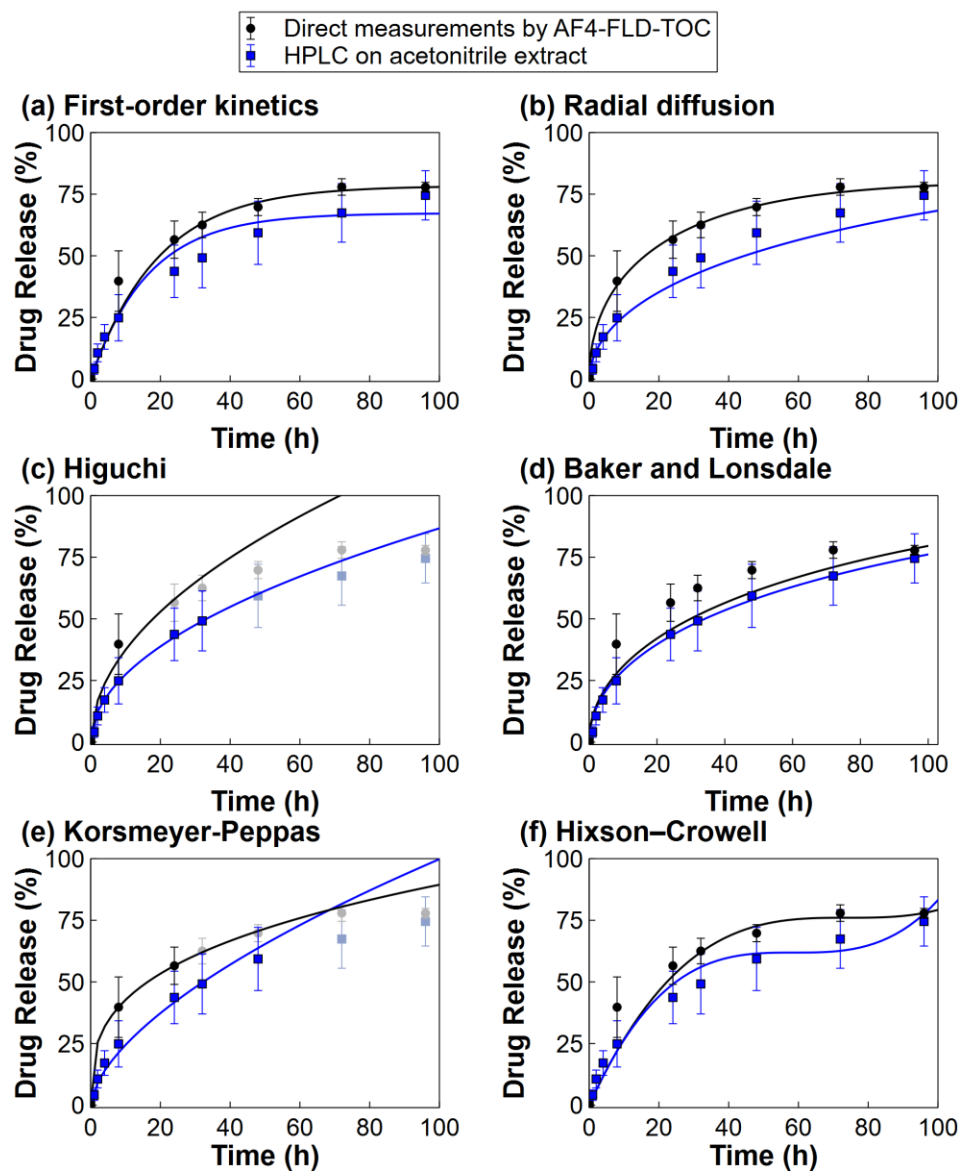
Figure C.11. Model fits for C6 release profile from PLGA NPs obtained by AF4-FLD-TOC or HPLC on the acetonitrile extract samples. The points shown in faded colors were excluded from the models.

C.10 AF4-FLD-UV or AF4-FLD-RI for Size-dependent Release Analysis

The size-dependent release analysis was performed using either UV or RI detectors for NP concentration (Figure C.12) and generally affirm the results of the analysis using

TOC detection as presented in the main text. The presented AF4-FLD chromatograms are normalized to the bulk PLGA concentration (using the integrated UV or RI peak area).
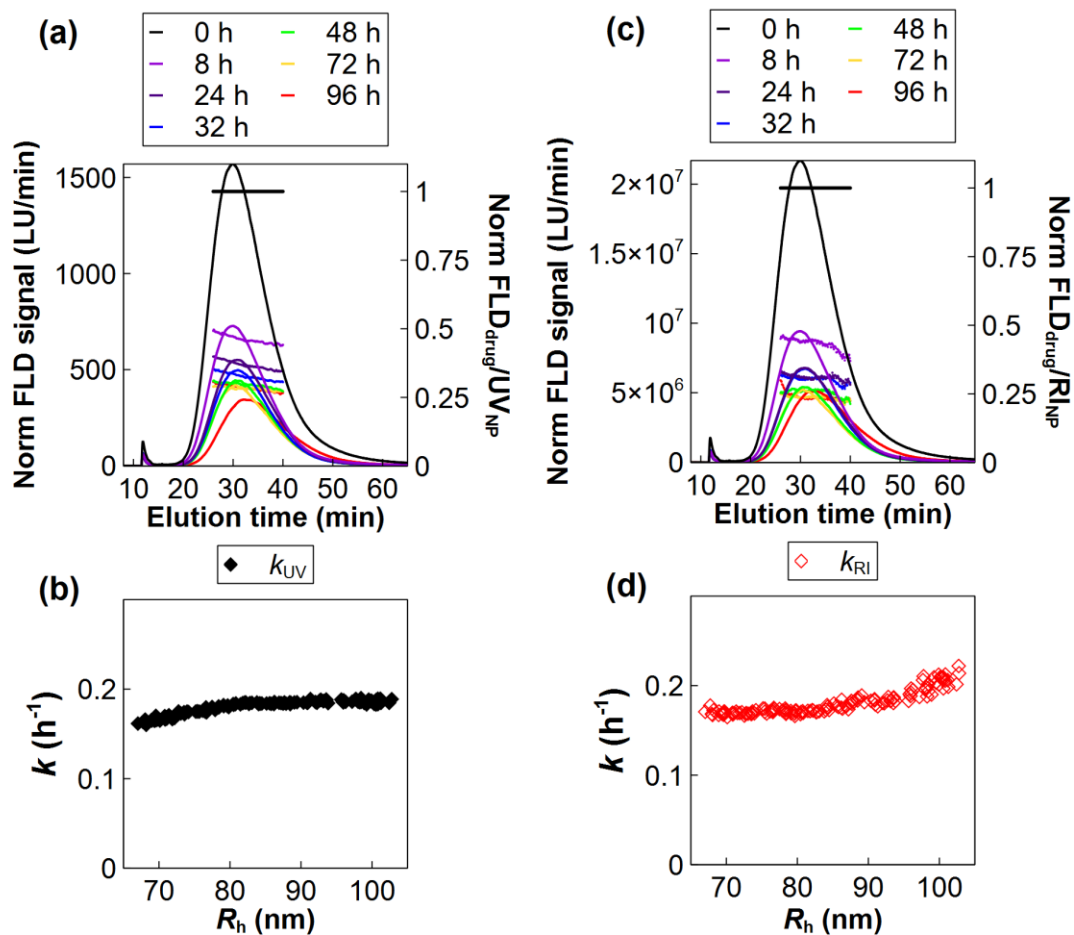
Figure C.12. Normalized AF4-FLD chromatograms, FLD/UV or FLD/RI ratios at each chromatographic time point normalized to the initial loading and fitted drug release rate constants from the size-resolved analysis